



EUROPEAN SOUTHERN OBSERVATORY
Organisation Européenne pour des Recherches Astronomiques dans l'Hémisphère Austral
Europäische Organisation für astronomische Forschung in der südlichen Hemisphäre

VERY LARGE TELESCOPE

TELESCOPE SYSTEMS DIVISION

SHS AND PWS COMPARISON TEST REPORT

Doc. No. VLT-TRE-ESO-14690-4724

Issue: 1.0

Date: 18/05/09

Prepared: E. Aller 18.05.09
Name Date Signature

Approved: M. Kasper 18.05.09
Name Date Signature

Released: N. Hubin 18.05.09
Name Date Signature



HIGH ORDER TESTBENCH
SHS and PWFS comparison test report

Doc:
Issue: 1.0
Date: 18/05/09
Page: 2 out of 80

CHANGE RECORD

ISSUE	DATE	SECTION/PAGE AFFECTED	REASON/INITIATION DOCUMENTS/REMARKS
1.0	18.05.09	All	



TABLE OF CONTENTS

CHANGE RECORD	2
TABLE OF CONTENTS.....	3
1 ACRONYMS.....	5
2 APPLICABLE AND REFERENCE DOCUMENTS	6
2.1 APPLICABLE DOCUMENTS	6
2.2 REFERENCE DOCUMENTS.....	7
3 SCOPE	8
4 SYSTEM OVERVIEW.....	8
5 SYSTEM CHARACTERIZATION.....	9
5.1 LIGHT SOURCES	9
5.2 TURBULENCE GENERATION	9
5.3 BOSTON MICRO DM.....	12
5.3.1 <i>BMM problematic</i>	14
5.4 INFRARED TEST CAMERA	16
6 HOT SHACK-HARTMANN WAVE FRONT SENSOR	17
6.1 INTRODUCTION	17
6.2 OPTICAL ALIGNMENT	17
6.3 SLOPE RECONSTRUCTION.....	17
6.4 SHS CHARACTERIZATION	18
6.4.1 <i>SHS linearity</i>	18
6.4.2 <i>Sensor sensitivity in Fourier space.</i>	19
6.4.3 <i>Spatial filter shack-Hartmann</i>	21
6.5 MODAL CONTROL IMPLEMENTATION	23
6.6 CALIBRATION	24
6.7 MODAL BASE.....	25
6.8 SLAVING.....	28
6.9 LOOP CONTROL	28
7 PYRAMID WAVE FRONT SENSOR	31
7.1 INTRODUCTION.....	31
7.2 OPTICAL ALIGNMENT	31
7.2.1 <i>Magnification and rotation correction</i>	32
7.2.2 <i>Shift correction</i>	33
7.3 PUPIL ACQUISITION AND SIGNAL COMPUTATION	35
7.4 MODAL CONTROL.....	37
7.4.1 <i>Computation of pure KL modes</i>	37
7.4.2 <i>Matching the BMM optical alignment</i>	37
7.4.3 <i>Selection of independent, master and slave actuators</i>	39
7.4.4 <i>Fitting of pure KL modes by the BMM influence functions</i>	41
7.5 PYRAMID'S TILT MODULATION	43
7.6 INTERACTION MATRIX ACQUISITION	45



HIGH ORDER TESTBENCH
SHS and PWFS comparison test report

Doc:
Issue: 1.0
Date: 18/05/09
Page: 4 out of 80

7.7	CONTROL LOOP ANALYSIS	46
7.7.1	Loop control implementation.....	46
7.7.2	Performance metrics and system parameters	47
7.7.3	Effect of the number of controlled modes	47
7.7.4	Estimation of Rejection Transfer Functions	49
7.7.5	Effect of the integrator's gain.....	52
8	SHWFS AND PWFS EXPERIMENT COMPARISON.....	54
8.1	EXPERIMENTAL PLAN.	54
8.2	INITIAL CONDITIONS.	54
8.2.1	Turbulence and illumination conditions.....	54
8.2.2	L3 gain and equivalent RON	55
8.2.3	Reconstructor.....	57
8.2.4	Loop frequency and bandwidth.	57
8.2.5	ITC: PSF image acquisition.	58
8.3	PSF ANALYSIS	59
8.3.1	The ghosts problem.....	59
8.3.2	PSF profile and pixel scale estimation	59
8.3.3	SR estimation	60
8.4	CLOSE LOOP OPTIMIZATION	60
8.4.1	SHS loop optimization	60
8.4.2	PWS loop optimization.....	65
8.5	PSF CORRECTION VERSUS MAGNITUDE: STREHL RATIO AND FWHM	68
8.6	PSF CORRECTION VERSUS STAR MAGNITUDE: PSF PROFILE AND CONTRAST	71
9	CONCLUSION AND DISCUSSION.....	76
10	ANNEX	78



HIGH ORDER TESTBENCH
SHS and PWFS comparison test report

Doc:
Issue: 1.0
Date: 18/05/09
Page: 5 out of 80

1 Acronyms

AO	Adaptive Optics
AS	Alternative Source
BMM	Boston Micro deformable Mirror
BW	Bandwidth
CODE	Corrective Optics Drive Electronics
DM	Deformable Mirror
FPDP	Front Panel Data Port
FWHM	Full Width Half Maximum
GUI	Graphical User Interface
HKL	House-Keeping Link
HOT	High Order Test
HSDL	High-Speed Data Link
HVA	High Voltage Assembly
IF	Influence Function
IM	Interaction Matrix
ITC	Infrared Test Camera
KL	Karhunen-Loeve
LA	Lenslet Array
MACAO	Multiple Application Curvature Adaptive Optics
MEMS	Micro Electro-Mechanical Systems
NTF	Noise Transfer Function
PSD	Power Spectral Density
PSF	Point Spread Function
PWS	Pyramid Wavefront Sensor
RTC	Real Time Computer
RTF	Rejection Transfer Function
SF	Spatial Filter
SFSHS	Spatial Filter Shack-Hartmann
SHS	Shack-Hartman wavefront Sensor
SNR	Signal to Noise Ratio
SPARTA	Standard Platform for Adaptive Optics Real Time Applications
SR	Strehl Ratio
SS	Standard Source
SVD	Single Value Decomposition
TTM	Tip Tilt Mount



HIGH ORDER TESTBENCH
SHS and PWFS comparison test report

Doc:
Issue: 1.0
Date: 18/05/09
Page: 6 out of 80

VLT Very Large Telescope
WFE Wave Front Error
XAO Extreme Adaptive Optics

2 Applicable and reference documents

2.1 Applicable documents

- AD1 High order test bench for extreme adaptive optics system optimization, E. Aller-Carpentier et al. Proc SPIE 7015, Marseille, 2008.
- AD2 E. Pinna et al, "The pyramid wavefront sensor for the high order testbench", Proc. SPIE 7015, Marseille 2008.
- AD3 Vernet et al. 2006, "Extreme adaptive optics system optimization with the high order test bench". Proc. SPIE, 6272, 62722K (2006).
- AD4 VLT-SPE-ESO-14690-3705 Issue 1, HIGH ORDER TEST BENCH Phase Screens, Technical Specifications and Statement of Work
- AD5 VLT-SOW-ESO-16100-4595 Issue 1, HOT Mirror Control Statement of Work and Technical Specifications
- AD6 VLT-SPE-ESO-14690-3414, High Order Testbench, Top Level Requirements.
- AD7 VLT-SPE-ESO-14690-4079, High Order Testbench Assembly, Integration, Testing Plan & Results.
- AD8 VLT-SPE-ESO-14690-4081, High Order Testbench Experiment plan Overview.
- AD9 VLT-TRE-ESO-14690-3857, High Order Testbench Design Report.
- AD10 VLT-TRE-ESO-14690-4080, High Order Testbench Simulations.
- AD11 VLT-TRE-ESO-14690-4082, High Order Testbench BMM Deformable Mirror Characterization.
- AD12 VLT-TRE-ESO-14690-4083, Andor iXON L3 Camera Characterisation.
- AD13 VLT-TRE-ESO-16100-3983, SPARTA for HOT Conceptual Design.
- AD14 shs_design_Nov05 , Design of the Shack-Hartmann Wavefront Sensor for HOT.
- AD15 HOT_Arcetri_V5 , Pyramid wavefront Sensor for HOT.



HIGH ORDER TESTBENCH
SHS and PWFS comparison test report

Doc:
Issue: 1.0
Date: 18/05/09
Page: 7 out of 80

2.2 Reference documents

- RD1 P.Martinez et al., "Phase and Lyot-type coronagraphs for the High Order Testbench prototyping and laboratory results" Proc. SPIE 7015, Marseille, 2008.
- RD2 Markus Kasper and Enrico Fedrigo, "Fast Calibration of high-order adaptive optics systems", J. Opt. Soc. Am. A, Vol. 21, No. 6, 2004.
- RD3 Horeinstain et al, "Eelctrostatic effects in Micromachined Actuators for Adaptive Optics, Journal of Eletrostatics, Vol 42, 69-81, 1997.
- RD4 Chirstophe Verinaud, "On the nature of the measurements provided by a pyramid wave-front sensor", Optics Communications, Vol 233, 27-38, 2004.
- RD5 Conan et al., "Wave front spectra in high-resolution imaging through turbulence", Opt. Soc. Am. A., Vol. 12, No. 7, July 1995/J.
- RD6 E. Gendron et al., "Astronomical Adaptive Optics. I. Modal control optimization.",Astron. Astrophys. 291, 337-347, 1994.
- RD7 E. Gendron et al, Astronomical adaptive optics. II. "Experimental results of an optimized modal control." , Astron. Astrophys. Suppl. Ser. 111, 153-167, 1995.
- RD8 Lisa A. Poyneer and Bruce Macintosh, "Spatially filtered wafe-front sensor for high-order adaptive optics", Opt. Soc. Am. A., Vol 21, No 5, 2004.
- RD9 E. Gendron and P. Lena, "Single Layer atmospheric turbulence demonstrated by adaptive optics observations", Astrophysics and Space Science 239, 221-228, 1996.
- RD10 Conan et al, "Distributed modal command for a two deformable mirror adaptive optics system", applied optics, Vol 46, No 20, 2007.
- RD11 Eric Gendron, "Optimization de la commande modale en optique adaptative: Applications a l'astronomie", These, March 1995.
- RD12 Roberto Ragazzoni, "Pupil plane wavefront sensing with an oscillating prism", Journal of Modern Optics, Volume 43, Issue 2, pages 289 - 293, 1996
- RD13 R. Ragazzoni and J. Farinato, "Sensitivity of a pyramidic Wave Front sensor in closed loop Adaptive Optics", A&A v.350, p. L23-L26, 1999
- RD14 S. Esposito and A. Riccardi, "Pyramid Wavefront Sensor behavior in partial correction Adaptive Optic systems", A&A v. 369, p. L9-L12, 2001
- RD15 S. Esposito et al., "Laboratory test of a pyramid wavefront sensor", Proc. SPIE Vol. 4007, p. 416-422, 2000



3 Scope

The scope of this document is to present the first results of the PWFS and the SHWFS experiments in order to assess the performances of the HOT AO systems. These experiments are carried out in the frame of the OPTICON joint research activity (JRA) 1 workpackage 3.8, by a collaboration of Arcetri, the University of Durham and ESO.

4 System overview

The High Order Testbench (HOT) (Figure 1) (AD1,AD3) implements a laboratory XAO system. Realistic conditions are achieved simulating the VLT pupil (8m) with a F/50 beam and applying different pupil masks. The HOT bench incorporates a turbulence generator with phase screens to simulate real seeing conditions.

Two deformable mirrors for WFE correction are integrated on the system. A first deformable mirror (60 bimorph elements) is used to correct large static aberrations of the bench. This mirror is placed on a TTM (Tip tilt mount) for tip tilt correction. The second one is a micro deformable mirror (electrostatic MEMS device) to correct the high order modes of the generated turbulence.

A cube beamsplitter splits the optical beam in two channels. A Shack-Hartmann or a pyramid working on the visible can be chosen on the first channel for wave front sensing. On the second channel an IR camera (ITC) is used to study the PSF image.

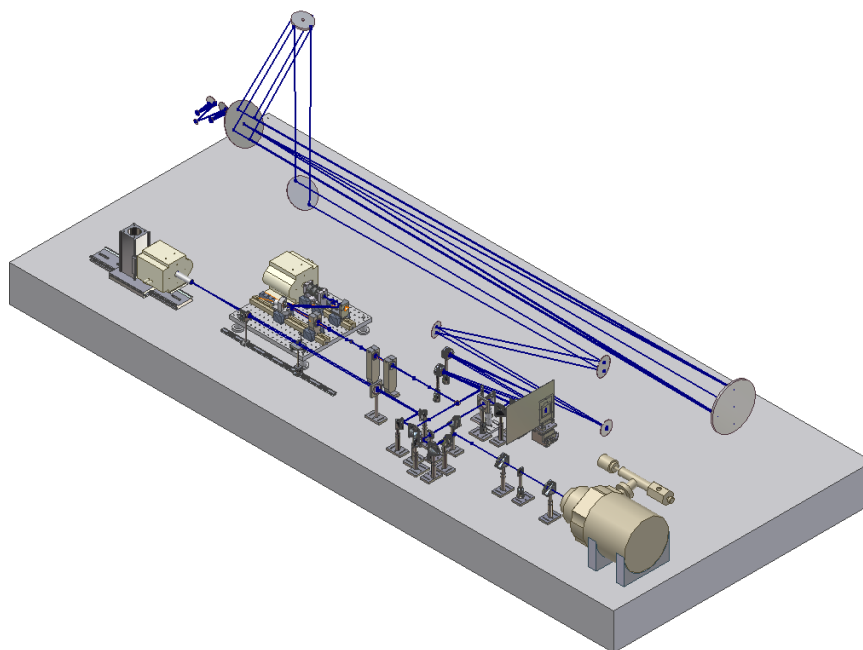


Figure 1. Schematic HOT setup overview including the SHWS, PWS and the IR path.



HIGH ORDER TESTBENCH

SHS and PWFS comparison test report

Doc:
Issue: 1.0
Date: 18/05/09
Page: 9 out of 80

All the optical elements and subsystems are installed and aligned checking aspects as: pupil size, conjugate planes, homogeneity illumination and F number. Both mirrors are characterized in terms of voltage-stroke behaviour, coupling, IF, defective actuators. The optical quality was checked on different points of the setup. The bimorph mirror was used to reduce the static aberrations to be under the specifications, thus a WFE of 50 nm RMS was achieved (measured on the WFS path).

5 System Characterization

5.1 Light sources

The bench is feed with two types of input sources. The first one called “*standard source*” (SS) goes through the turbulence generator, so is affected by the phase screens. For this case we use a 8 μm fiber to simulate a point source.

The second source is called “*alternative source*” and goes through an alternative path avoiding the turbulence generator. This alternative source is needed for all the calibration operations and static aberration studies. A 62.5 μm fiber is used on this case to feed the source.

White light is used to feed the sources for both calibration and experimental cases. This white light is generate by an halogen lamp using a power supply to regulate the intensity. A laser is also used but only for alignment operations ($\lambda = 0.633 \mu\text{m}$).

Figure 2 shows the intensity as a function of the voltage apply to the lamp power supply. Plotting the intensity as a function of v^2 a linear behaviour is recovered and the slope shows the resistance of the lamp. We realized that for low voltage range (~ 5 volts) the resistance changes due to the different temperatures. In this range stabilities differences were daily observed, so it is required to check the number of photons before any measurement, especially on low flux conditions.

5.2 Turbulence generation

The turbulence is generated using two phase screens in reflection with a diameter of 50mm. The optical setup provide an $f/16.8$ beam to the test bench. The phase screens can rotate independently. Both phase screens are located in pupil planes conjugated with the deformable mirror. The diameter of the beam on the phase screens is ~ 6.7 mm.

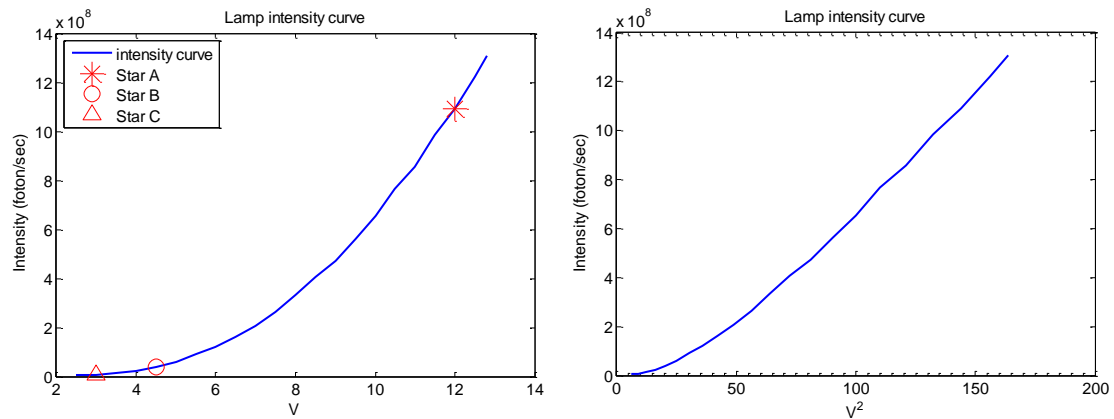


Figure 2. Lamp intensity curves measured with the SHS. (a) Left: Lamp intensity as a function of the voltage. The flux corresponding for high and low flux conditions cases used on the experiments is superimposed to the curve (4 magnitude differences between A-B and 1.5 magnitude differences between B-C). (b) right: Lamp intensity as a function of square voltage showing the variation of lamp resistance caused by the temperature.

Phase screens have been calculated for different kinds of seeing (AD4):

- 2 identical phase screens producing a seeing of 0.5" with reduced low order aberrations
- 2 identical phase screens producing a seeing of 0.85" with reduced low order aberrations
- 2 identical phase screens producing a seeing of 0.65" with full Kolmogorov turbulence

The low order reduced phase screens are required to avoid saturation of the micro-DM which has limited actuator stroke of about two microns. The low spatial frequency spectrum of turbulence in this case is the one that would be left after correction by a 60 actuator bimorph deformable mirror.

The 0.5" phase screens (reduced low order aberrations) are installed on the HOT bench and used for the experiments explained in next sections. The spatial resolution characterization done previously with a commercial Shack-Hartmann HASO 64 is shown in Figure 3.

The equivalent wind speed for the turbulence generated was measured on open loop using the SHS following Conan et al, 1995 (RD5). The turbulence generator is configured with both phase screens turning on opposite sense (same turbulence direction) at minimum speed. A coherence time of ~ 150 s for the turbulence was measured computing the temporal autocorrelation of the subapertures slopes.

The atmospheric behaviour reproduced by rotating phase screens should follow the Taylor's hypothesis and be considered as "frozen turbulence". Thus, computing the spatiotemporal cross-correlation of the slopes measurements we should see a clear peak crossing the pupil as showed on Figure 4. The wind speed found is 1.3 m/s taking on account a 8 m pupil.

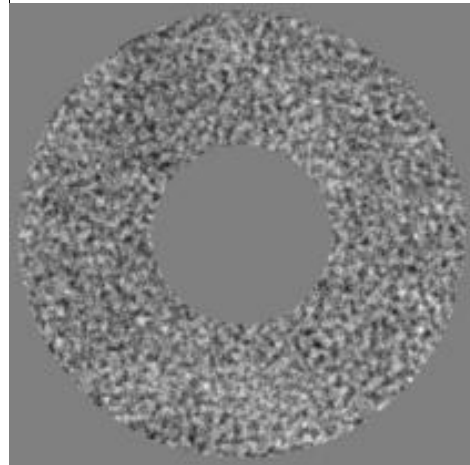
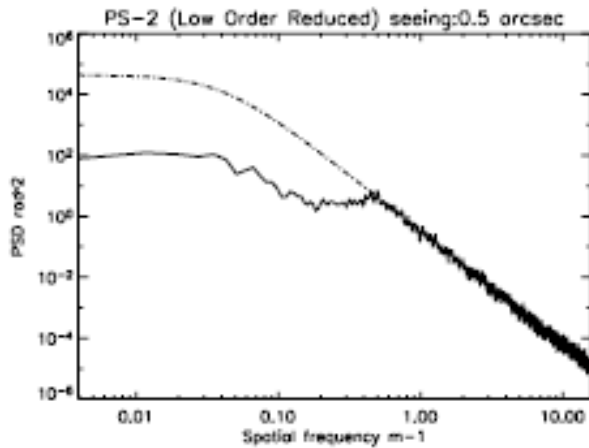


Figure 3. 0.5" phase screen characterization. (a) left: Power spectrum (b) right: Wave-front map.

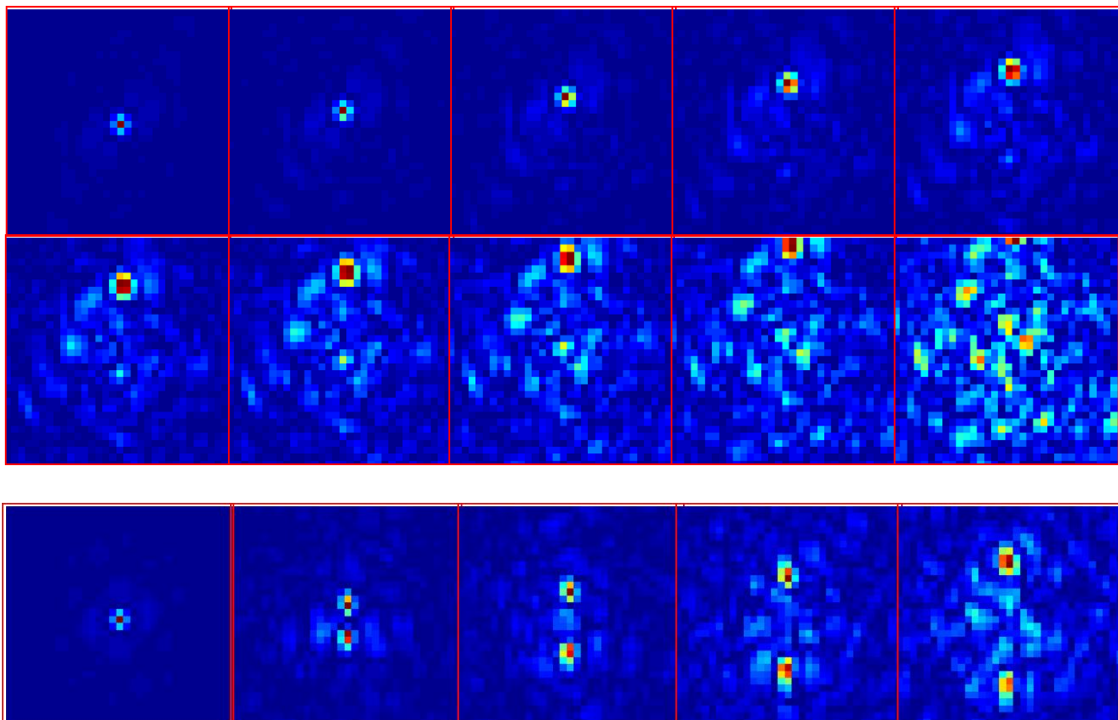


Figure 4. (a, up) Series of 10 images representing the spatiotemporal cross-correlation taken 200 ms. A correlation peak is clearly visible and moves uniformly away from the center at a speed 1.3 m/s. Each image show only half of the pupil. (b, down) Two correlation peaks are visible when we change the sense of the phase screens movement.



5.3 Boston Micro DM

The deformable mirror used for compensated the turbulent wavefront is a micro MEMS device from Boston Micromachines. It is a 10.8 mm squared deformable mirror with 340 μm actuator pitch for a total of 32x32 actuators.

Two BMMs were characterized in terms of stroke and linearity finding similar behavior (noted as BMM1 and BMM2) using a commercial FISBA interferometer. The measured mechanical stroke is 1.53 μm PTV (0.83 μm interactor stroke) and 11% of coupling between actuators. The stroke versus voltage for an electrostatic actuator do not follow a linear relation, instead, it could be approximated by a quadratic law (RD3). Measuring the stroke-voltage curve this behavior was observed, and it was also found the anomalous behavior predict by the theory at high voltages. Thus, the effective voltage range is 165 volt with a bias value of 114 volts.

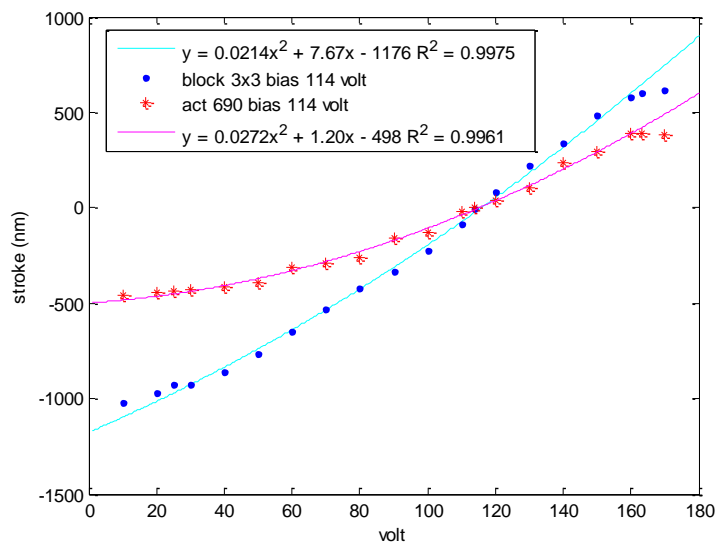


Figure 5. Plot of the quadratic volt-stroke behavior of the BMM.

The flatness of the mirror was also measured. The center of the mirror is quite flat but the slope increase quickly approaching to the edge (4 last actuators rows) achieving a maximum value of 700 nm. This value is quite high and produced a diffraction cross on the PSF. The MACAO DM is used on the bench to correct the static aberrations and was also able to correct partially this effect.



HIGH ORDER TESTBENCH
SHS and PWFS comparison test report

Doc:
Issue: 1.0
Date: 18/05/09
Page: 13 out of 80

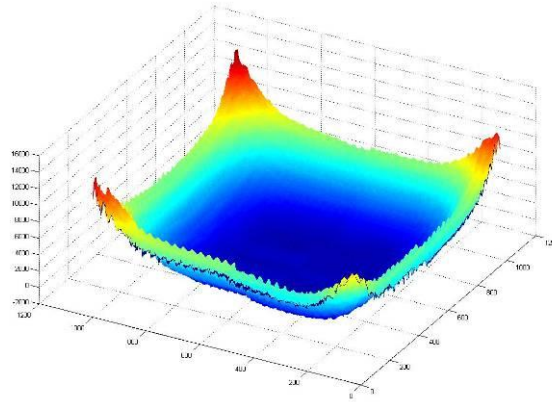


Figure 6. Tridimensional representation of the flatness of the mirror.

The measurement of the IF for all the actuators was required for the modal base reconstruction and for defective actuators detection. There are 2 inactive actuators inside the pupil by mirror design (they act as pin connection for ground base and TTM control).

In addition for the BMM1 one inactive actuator was found inside the pupil. This actuator would introduce a new error on the wavefront since it is stuck (stays always at 0 volt position). 4 defective actuators were detected inside the pupil for BMM2 but on this case they are linked and could float with the other actuators. These actuators would not contribute on the wavefront correction but at least would not introduce a new error. This is the reason why the BMM2 was finally selected.

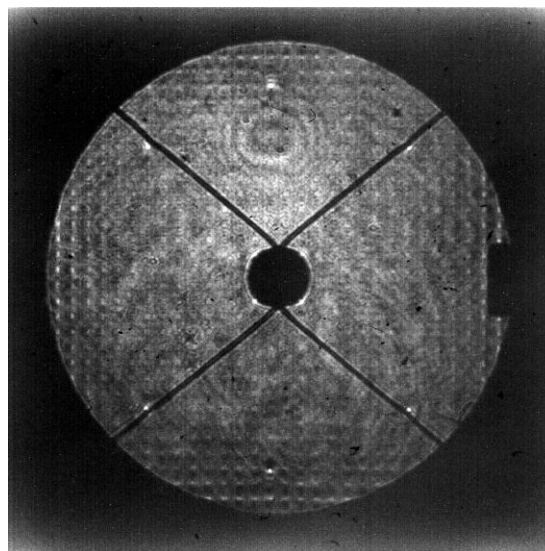


Figure 7. Pupil plane image on the SHS setup. We could see the shape of the VLT pupil and the edge cut to hide the inactive actuators.



HIGH ORDER TESTBENCH
SHS and PWFS comparison test report

Doc:
Issue: 1.0
Date: 18/05/09
Page: 14 out of 80

A modification on the pupil mask shape was done to hide the area of the two inactive actuators by design (even if some active actuators are hidden too).

The electronics to drive the micro-DM have been produced by Shaktiware. Besides commanding the MEMS1024, Shaktiware also provided a small electronics box that can command the MACAO TTM with $\pm 10V$. The corrective drive electronics (CODE) is accessible by TCP connection through two main links. House-keeping link (HKL), a non real time communication (configure the CODE, inquire status) and high-speed data link (HSDL), the real-time, low latency data link on which the real-time control commands are sent to the CODE.

5.3.1 BMM problematic

During two years the BMM2 was used on the bench for normal AO operations (sensor calibration, close loop ...). After this time, defective actuators began to appear. First, the HVA boards were checked to rule out electronic causes.

The problem consists on loss of actuator stroke. Most of the defective actuators lose all the stroke from the first moment, while others seem to keep some movement capacity until they stuck completely at resting position.

The BMM manufacturing company was contacted in order to have some information about this problem but they could not help. Contacting other BMM users, a possible explanation was found. A combination of high voltage and water vapor inside the actuator produces the electrolysis of the H_2O molecule. The negatively-charged OH^- ions are attracted to the anode, and then form $SiOH$, which combines with more OH^- to make SiO_2 (glass, which is NOT conductive), releasing molecular hydrogen. Thus, the actuator lost the stroke since it could not create the electrostatic force. The BMM was imaged with a microscope to confirm the oxidation, as shown in Figure 8.

The number of defective actuators increased until it was not possible to drive the mirror (up to 30 defective actuators). The BMM2 was ruled out and BMM1 was reinstalled on the bench for the comparison experiments. The only problem is that the quality of the measured IF is a bit worse and has a bigger slope on the mirror edges.



HIGH ORDER TESTBENCH
SHS and PWFS comparison test report

Doc:
Issue: 1.0
Date: 18/05/09
Page: 15 out of 80

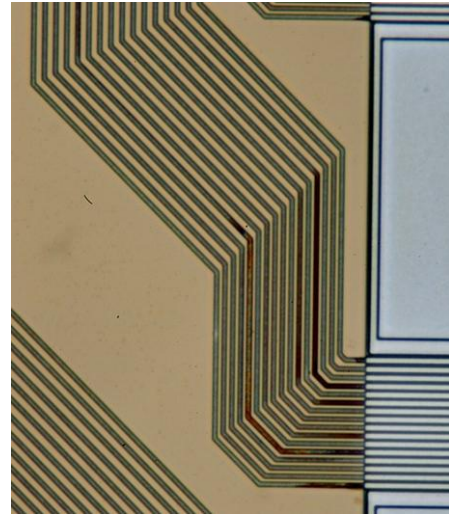
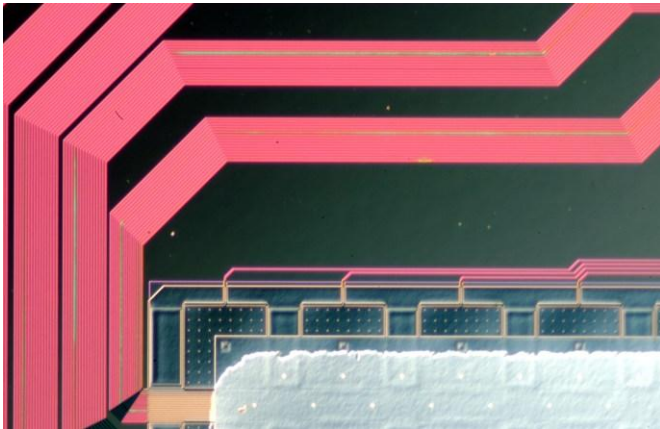


Figure 8. Microscope images of the BMM connections done on the LESLIA laboratories. (a) left: differential interferential contrast interferometer image (b) right: direct microscopic inspection. The different color on the electronic lines (green compare to the pink on the left image, brown compare to the green on the right image) is a clear sign of oxidation.

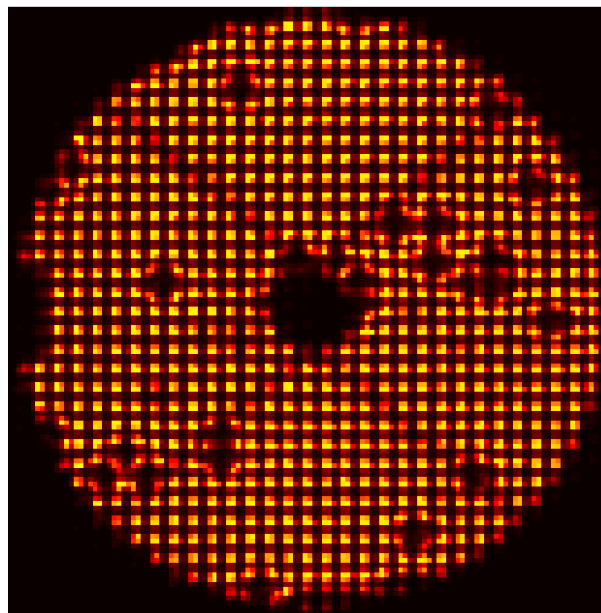


Figure 9. SHS CCD image showing the effect of the defective actuators. When the BMM actuators are set to the bias voltage the defective actuators stay at 0 volt position.

5.4 Infrared Test Camera

The original infrared camera ,RASOIR, was substituted with the Infrared Test Camera (ITC) because of vacuum leak problems. The ITC detector is a Hawaii array (1K x 1K) with 4 quadrants (512x512). The camera incorporate internal optics designed to enable a pixel-scaled of 5.3 mas/pix. The camera is cooled until 103 – 107k under vacuum conditions of 10^{-5} mbar for optimal performance.

The ITC controlled software let us set the exposure time (minimum 1.8s) and offers a continuous image. For long exposure time the camera records short images and give the mean image as result.

The ITC offers the possibility to use different filters (J,H,K) narrow and broadband placed on an internal wheel. On the HOT bench is used the broadband H filter (centre at 1.6 μm $\Delta\lambda/\lambda=20\%$) combined with a H narrow external filter placed in front of the ITC window (centre at 1.6 μm $\Delta\lambda/\lambda=1.4\%$).

In addition a neutral density wheel is required to avoid saturation on the ITC, since the light intensity is define by the WFS. Thus, changing the level we maximize the signal for each flux conditions. The non linearity range begin around 10000 – 11000 counts .

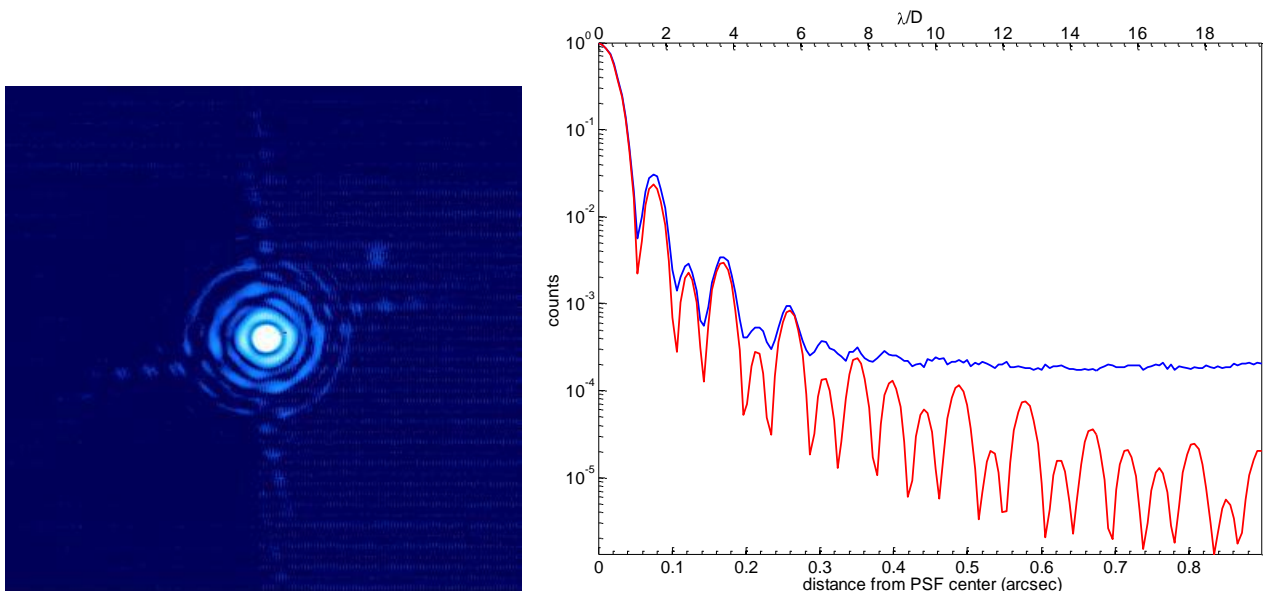



Figure 10. (a) left: PSF image obtained with the ITC camera on the IR path. (b) PSF profile (blue) compare with the theoretic one (red). The SR estimate is ~95%.

	HIGH ORDER TESTBENCH SHS and PWFS comparison test report	Doc: Issue: 1.0 Date: 18/05/09 Page: 17 out of 80
---	--	--

6 HOT Shack-Hartmann wave front sensor

6.1 Introduction

The HOT Shack-Hartmann wavefront sensor designed by the University of Durham, is modeled with an input beam from a 8 m class telescope with a 400 m focal length (F/50). The WFS provides a plate scale of 0.5 arcsec/pixel, with 31x31 subapertures, each detected on 4 x 4 pixels of a 24 μm pixel CCD. The detector used, as on the PWFS, is a 128x128 pixel electron multiplying CCD Andor iXON L3 (AD12). This camera is a sub-electronic readout noise at 400 Hz frames rate working under L3 multiplication gain (0.07e- rms read noise).

The WFS could also work as a SFSHS (Spatial Filter Shack-Hartmann Wave Front Sensor) adding pinholes with different sizes on the entrance focal plane of the SHS setup (1.25, 1.5 and 1.8 λ/d). In addition a pinhole covering the full 2 arcseconds subaperture is used on the normal SHS operation as field stop to reduce the crosstalk between subapertures.

A fiber could be installed on the focal plane as reference source for zero slopes measuring.

More details on the design could be found on AD14 and AD1.

6.2 Optical alignment

The SHS is aligned taking special care on collimation, pupil plane location, subapertures and actuators matching on the correct Fried geometry and rotation between LA and CCD. A magnification around 1.03 is found between subapertures size and actuators pitch. Details of the alignment could be find on AD1.

6.3 Slope reconstruction

The SHS HOT slope acquisition is based on a C software WPU emulation (Wave front Processing Unit) implement by the SPARTA group at ESO. The WPU Server process acquires continuously the pixels from the fiber serial FPDP and compute the gradients with a simplified algorithm. The slopes are acquired on real time (around 100 Hz) by MATLAB using a set of MEX functions that acts as bridge between the C and the standard MATLAB code. Thus, the slopes are easily available for the analysis and close loop implementation.

The slopes are computed with a basic four-bin slopes detection algorithm:

$$Slope = \frac{w_1 \cdot a_1 + w_2 \cdot a_2 + w_3 \cdot a_3 + w_4 \cdot a_4}{a_1 + a_2 + a_3 + a_4}$$

Where $w_1 \dots w_4$ are the scalar weighting functions applied to the outputs of the detector elements $a_1 \dots a_4$.

The weighting factors (w_1, w_2, w_3, w_4) used are equal to (-1.5, -0.5, 0.5, 1.5).



HIGH ORDER TESTBENCH
SHS and PWFS comparison test report

Doc:
Issue: 1.0
Date: 18/05/09
Page: 18 out of 80

6.4 SHS characterization

6.4.1 SHS linearity

In order to achieve better performance on close loop it is necessary to know the SHS behavior on terms of linearity and crosstalk. The TTM is used to obtain the linearity curve of the sensor since we need to produce known variances tilts on the wave front. The two TTM axes will be called channel 0 (Y slopes) and channel 1 (X slopes). Both channels are controlled in the range -1 to 1, where 0 is the zero position (it will be called “normalized units” (nu)). These values correspond to a voltage range from -10 to 10 volts. Thus, the amplitude of the mount is 500 mas per 0.1 nu. Slopes measurements are acquired for different positions of the useful range of the two TTM axes.

First we check visually on the sensor which is the TTM range necessary to produce a displacement of 1 pix in the centroids position. This value is approximately 0.082 nu, but the slopes measured are around 0.6 pix instead of the 1 pix expected. This is caused by a clearly aliasing between subapertures. To reduce the effect of the crosstalk a field stop (pinhole) covering the full 2 arcseconds subaperture is installed on the focal plane. The mean linearity curves for both cases are showed on Figure 11 and the main parameters founded are summarized on Table 1.

We can summarize the differences between the cases with and without pinhole as follow:

- A) The tilt dynamical range gives the maximal turbulence that the WFS can measure. In both cases it is the same, since this parameter depends on the SHS design (i.e. weights for the slopes calculations).
- B) The slopes dynamical range increases a 13%. This parameter depends on the crosstalk between subapertures. Since, by design there is not a guard band between the 4x4 pixels of each subaperture, the sensor suffer from an important crosstalk, the use of the field stop reduce it clearly.
- C) The difference on behaviour between subapertures is not important. Only some subapertures in the edge and under the spider present a smaller slope dynamical range. We will need to take care of it when the interaction matrix acquisition will be taken, so the slope dynamical range map per subaperture calculated is necessary.



HIGH ORDER TESTBENCH

SHS and PWFS comparison test report

Doc:
Issue: 1.0
Date: 18/05/09
Page: 19 out of 80

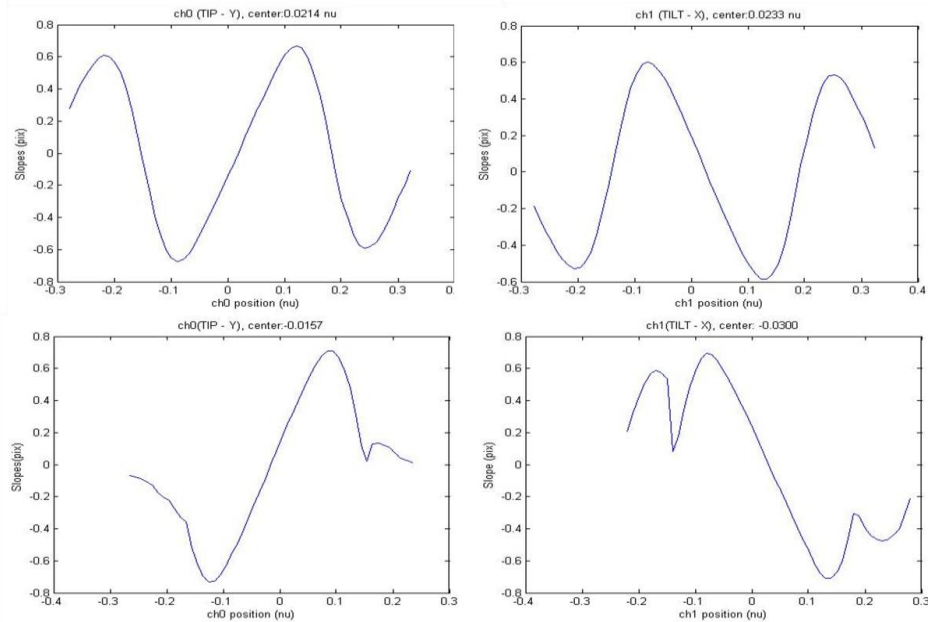


Figure 11. Mean linearity curve on X and Y for the SHS. Up: Without pinhole. Down: with pinhole.

Without pinhole:	With pinhole:
CH0: max = -0.67 ± 0.08 pix min = 0.67 ± 0.08 pix; Dinamical range (tilt) = 0.21 ± 0.01 nu. Dinamical range (slope) = 1.3 ± 0.1 nu. Linear range slope: 7.7 pix/nu	CH0: max = 0.73 ± 0.07 pix min = -0.75 ± 0.07 pix; Dinamical range (tilt) = 0.21 ± 0.01 nu. Dinamical range (slope) = 1.5 ± 0.1 pix Linear range slope: 8.1 pix/nu
CH1: Max = 0.60 ± 0.08 pix min = -0.59 ± 0.09 pix Dinamical range (tilt) = 0.21 ± 0.01 nu. dinamical range (slope) = 1.2 ± 0.1 pix. Linear range slope: 7.1 pix/nu Mean dynamical range is 1.05 ± 0.05 arsec.	CH1: Max = 0.70 ± 0.08 pix min = -0.72 ± 0.07 pix Dinamical range (tilt) = 1.4 ± 0.1 nu. dinamical range (slope) = 0.21 ± 0.01 nu. Linear range slope: 7.6 pix/nu Mean dynamical 1.05 ± 0.05 arsec.

Table 1. SHS linearity parameters. (The linear range is considered 85% of the max-min dynamical range).

6.4.2 Sensor sensitivity in Fourier space.

The goal is to verify that the sensitivity of the slopes measurements have a well defined dependency with the aberrations spatial frequency k . On the SHWFS being a slope sensor, the variance of the measurements is expected to be $\propto k^2$. This assumes a correction factor (RD4) $1/\text{dsinc}((dk))^2$ due to the finite sampling with sub-aperture of size d .

The method used consists on building a set of sinusoidal mirror modes on the BMM with 1 to 15 cycles/pupil frequency. The analyzed slope variance measured by the SHS for this set of modes are shown in figure X. The first 11 modes have a good adjustment to a square curve, but higher frequencies do not fit since the BMM is not able to well reproduce



the modes. If now we take on account the corrective factor, it is shown that for the highest modes the adjustment to the curve is better.

On Figure 12a is shown the relation between the phase produce by the sinusoidal modes and the field intensity (PSF). As the theory predict, now the field in the focal plane is the unaberrated field due to diffraction plus a series of weighted replications at distances proportional to the frequency. The spatial filter SHS exploits this relationship between the frequency content of the phase aberration and the field intensity and PSF (RD8).

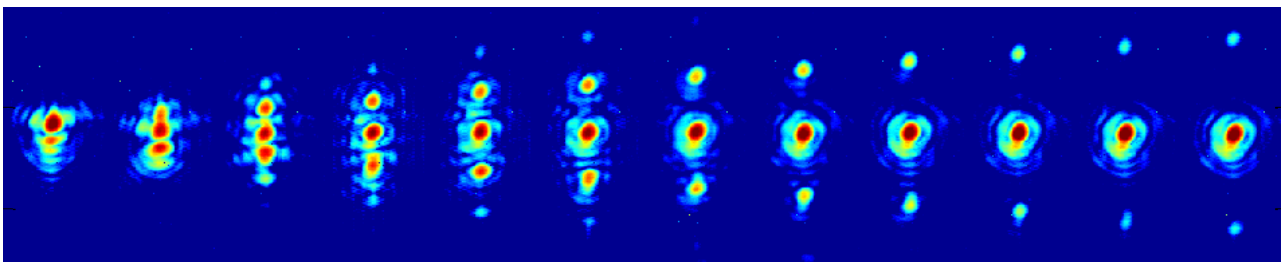
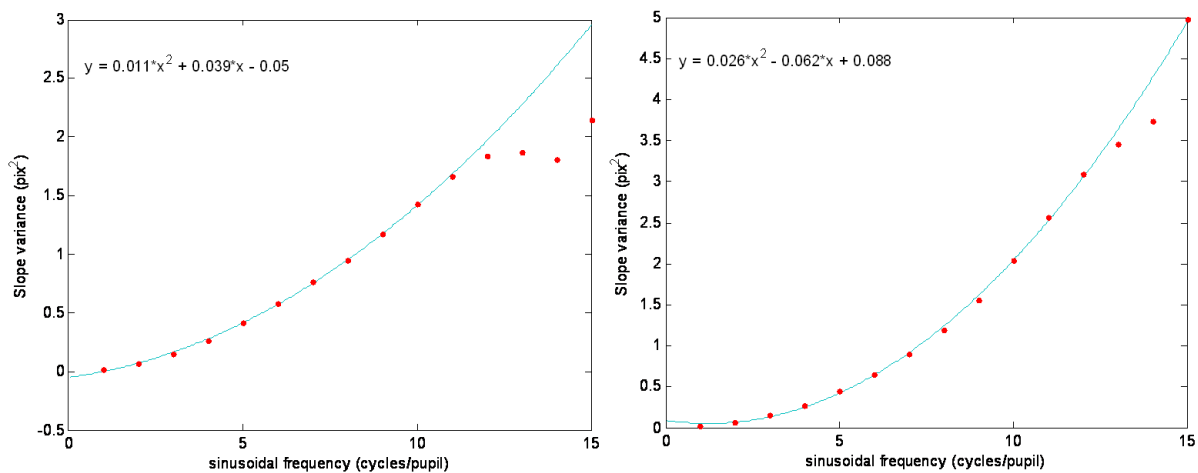



Figure 12. (a) Up: Variance slope study on function of the sinusoidal mode frequency produced by the BMM. On the left adjustment without correction factor applied. On the Right adjustments taking on account the correction factor. (b) down: Focal plane images on the scientific path showing the effect of the sinusoidal modes. Increasing the frequency (1 – 12 cycles/pupil) the PSF replications move away from the central PSF. For frequencies 5 and 6, the second order speckle is shown clearly. The images are taken with the IR – ITC camera on band H.

	HIGH ORDER TESTBENCH SHS and PWFS comparison test report	Doc: Issue: 1.0 Date: 18/05/09 Page: 21 out of 80
---	--	--

6.4.3 Spatial filter shack-Hartmann

The performance of the classic Shack-Hartmann wave-front sensor increase by using a field stop (pinhole) at a focal plane before the wave-front sensor. This pinhole acts as a spatial low-pass filter on the phase avoiding aliasing errors (RD8).

The spatial filter for the SHS should be $\sim \lambda/d$ in size. We add some margin to the λ/d to improve sensor linearity and dynamic range. Thus three spatial filters are foreseen 1.25, 1.5 and 1.8 λ/d . Assuming $\lambda \sim 700$ nm and f/48 beam focus the corresponding sizes are: 1.3, 1.6 and 1.9 mm.

The correct alignment of the pinhole is an import factor to assure the stability of the sensor on close loop and is handicapped by the small size of the pinhole and the few number of pixels per subaperture.

To align the SF, first, the loop is closed without SF (no turbulence). Thus, tip and tilt errors are removed assuring that the PSF on the entrance focal plane is aligned with the subapertures. Now, a temporally reimaging lens is placed after the SHS collimator to recover the image of the PSF on a mini CCD camera. The SF is placed on the focal plane taking into account that the superposed image of SF and PSF are centred.

It is important to check that the SF is on the correct focal plane. Without removing the mini-ccd a diffuse light is installed just before the SF (loosing the image of the PSF). The SF is displaced on z-axis until the edges appear sharp on the mini-ccd. Thus, the PSF and SF are focussed on the the same plane.

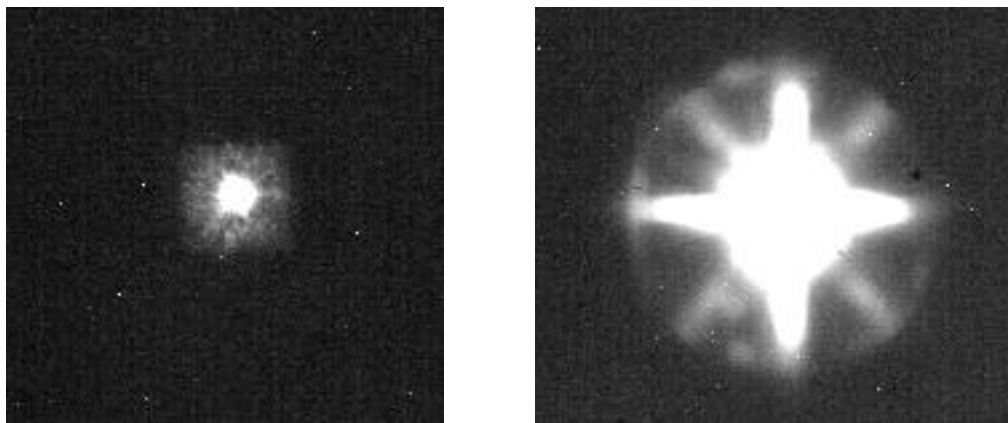


Figure 13. Image of the reimaged pupil plane on the mini-CCD used for centring the SF. (a) Left: Image of the PSF through the 1.8 λ/d SF. (b) Right: Saturated image of the PSF through the 2 arcseconds field stop. It is visible a cross on the PSF caused by the absence of flatness of the BMM. The faint cross at 45 degrees is caused by the spider mask.

Another way to center the SF use directly the SHS sensor. Installing a diffuse light before the SHS (as explained before) we will see the subapertures illuminated on the SHS, since the SF will act as a light source. Displacing the SF a tip-tilt will be created on the



subapertures. The SF is centred with the subapertures when the tip-tilt seen on the subapertures is minimized.

It is checked that both methods give the same result. The stability of the loop with SF is quite sensible to this alignment, specially on the focus position. If it is not good centred we see how the actuators of one side saturated quickly.

We tried to close the loop with the $1.5 \lambda/d$ SF. Without turbulence it was possible to close it but some actuators on the edge were saturated. With turbulence, the loop was not stable and the actuators saturated quickly. We try to acquire a new interaction matrix through the SF, but the problem persisted.

We installed the $1.8 \lambda/d$ SF. Increasing the size of the pinhole the stability of the loop should be better. The loop seems to be stable with and without turbulence for loops of around 5 minutes. But as we will explain on the experiments comparison, some instabilities appears, and specific regions of actuators saturated. In addition, no increase on the SR performance was achieved. Also on this case, a new IM was acquire trough the SF. But the loop diverge quickly.

Subapertures linearity curves for the $1.8 \lambda/d$ SF were measured to check possible problems. We found quite different behaviour for different subapertures, both on the slope and the dynamical range. The reason of this loss of linearity was not yet explained and will be object of near future studies. The linearity curve for some anomalous subapertures are shown in Figure 14.

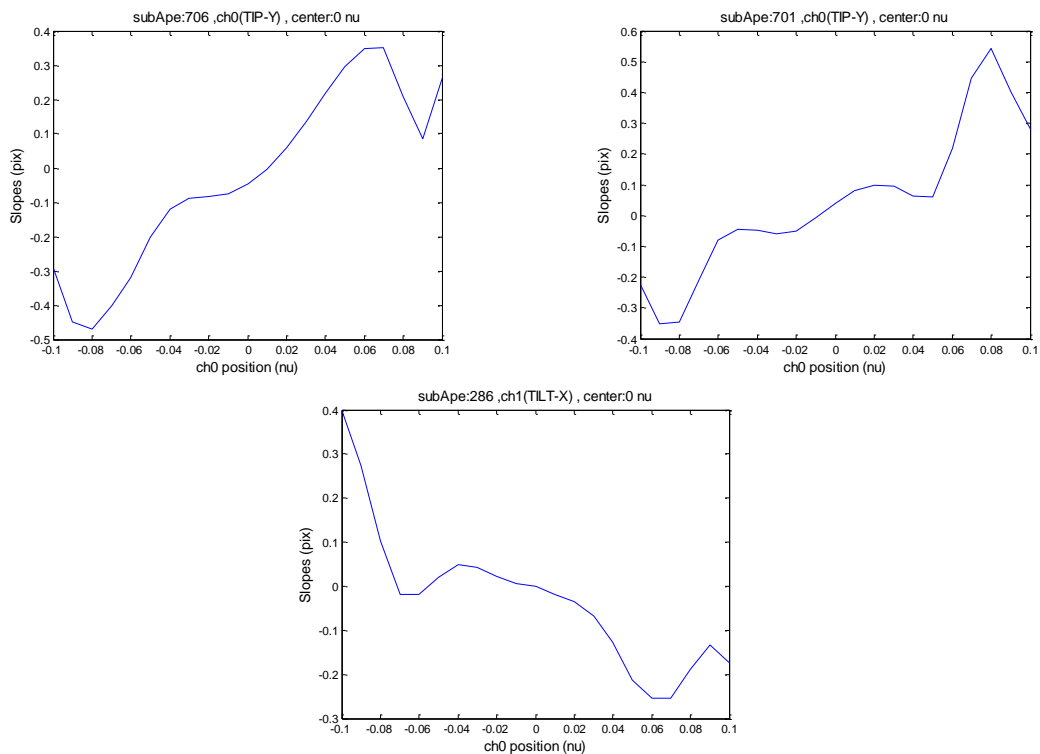


Figure 14. Example of anomalous linearity curves for some subapertures (the normal linearity curve for a subaperture could be found on section 6.4.1).

6.5 Modal control implementation

The modal control follows the PUEO method inspired from Gendron & Lena, 1994 (RD6, RD7). The reconstructor is obtained as a combination of a zonal interaction matrix and a modal base defined as:

$$\begin{aligned} R &= B \cdot G \cdot B^{-1} \cdot D^+ \\ \vec{a} &= R\vec{c} \\ \vec{c} &= D\vec{a} \\ \vec{a} &= B\vec{m} \end{aligned}$$

Where \vec{a} is the actuator vector, \vec{c} the measurement vector (slopes) and \vec{m} is a coefficients mode vector. D is the zonal interaction matrix that goes from actuators to measurements (slopes), B is the modal base matrix (goes from modes space to actuators space). G is a diagonal matrix where the i^{th} element is the gain on the mode i .

We considered 718 subapertures illuminated on the SHS. We do not use the subapertures outside the pupil, the central obstruction and 10 more on the pupil side (hidden by the pupil mask too). In the original pupil mask the subapertures corresponding to the spider were badly illuminated. In the actual, the spiders size was reduced, thus, these subapertures are available for the wave front measurement. There are 792 actuators surrounding the subapertures configured. The final number of actuators controlled will increase since an external ring of slaved actuators is added. The subpupils and actuator map is showed on Figure 15.

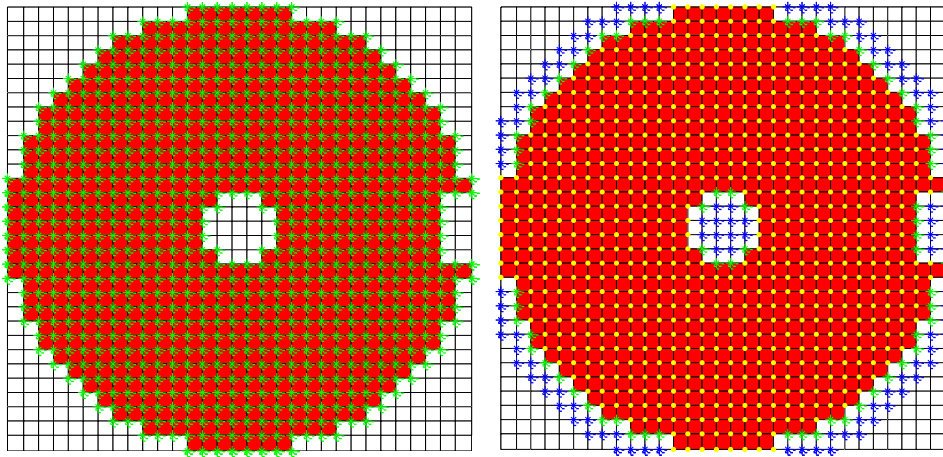


Figure 15. (a) Left: View of the subpupil map showing the valid actuators. (b) Right: Slaving actuators map. On yellow, normal active actuators, on green, master actuators, and on blue, slaved actuators.



6.6 Calibration

The zonal calibration is obtained using a Haddamard matrix (instead of a simple diagonal matrix). This pattern is largely demonstrated (RD2) to maximize the SNR on the sensor. In other case, the calibration time required for similar SNR would be extremely long for a 1024 actuators system. The Haddamard matrix apply 1024 voltage patterns, all the actuators are calibrated, and only at the end of the process the active actuators are selected. 10 measurements are taken for each Haddamard pattern (10 up and 10 down) at a frequency of around 20 hrzs. 5 cycles are measured to obtain better SNR.

In a first step the calibration is done using the same bias voltage for all the actuators (114 volt). The interaction matrix measured is used to close the loop removing static aberrations. Thus, the mirror voltage pattern that minimize the slopes on the SHS is obtained. This pattern is used as bias for a new interaction matrix. The dimension of the acquired IM is 1436 x 1024 (slopes x actuators). The final IM is reduced on size (1436 x 792) since we keep only the active actuators.

The IM inversion is required to obtained the reconstructor. The SVD algorithm from matlab is used to compute the inversion truncating the last 24 modes (Figure 16), corresponding with a truncate value for the eigenvalues of 0.5 (~ 120 conditioning number). This is the optimal value found, truncating more modes, the close loop do not correct the turbulence, and if more modes are used, actuators saturation appears and the loop divergence.

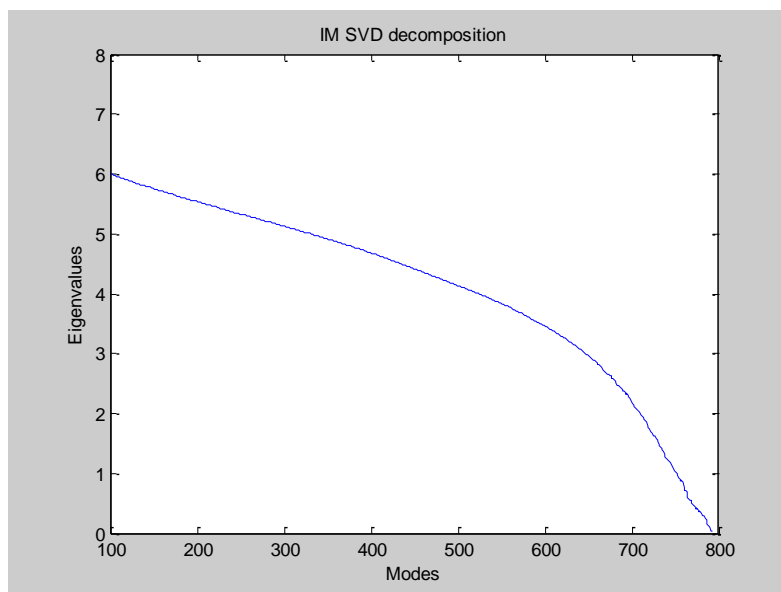


Figure 16. Plot of the eigenvalues obtained from the SVD computation of the zonal IM. (Condition number 1565).

The signal on the calibration is optimized looking for the maximum actuator stroke. For that a set of IM's are taken with increasing values of the actuator stroke applied for the Haddamard patterns. For each pattern it is verified that the signal produced on the SHS do not

saturate the linear range for each subaperture taking on account the individual linearity curves measured on the characterization (section 6.4.1).

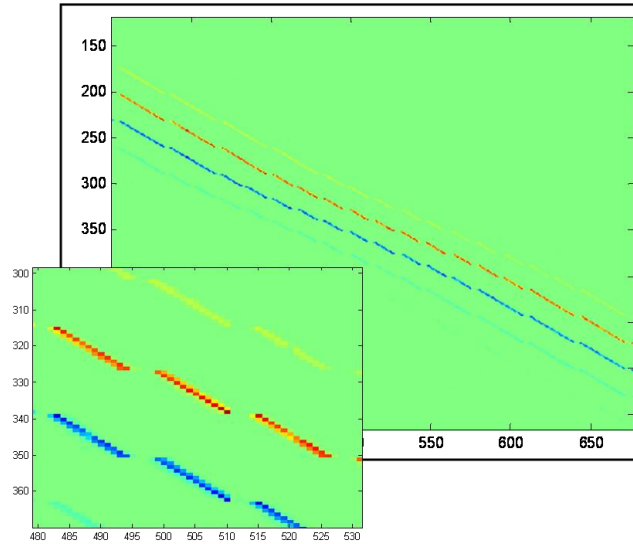


Figure 17. Image of a section of the IM matrix.

6.7 Modal base

The modal base construction is inspired on the method develop by Gendron (RD11) and applied previously, for example, on the Keck AO, but was not tested before for larger actuator AO systems. The specific algorithm used is the same used to obtained the modal base for the XAO system of SPHERE.

The idea is to obtain a Karhunen-Loève base where the modes are orthogonal and uncorrelated simultaneously. For this we take into count the mirror space, i.e, the real measured influence functions and the atmospheric profile we want to correct. Diagonalizing the geometric covariance matrix produces orthogonal modes, and the eigenvectors of the statistical covariance matrix produces uncorrelated modes. Then, a double diagonalization operation of both matrices gives the desired base that allows us to go from mode space to actuator space.

We consider the projection of the turbulent wavefront space onto the space defined by the DM influence functions, noted E_{wf} . We want to find the Karhunen-Loeve (KL) basis noted Q of the subspace E_{wf} with respect to the tip-tilt free turbulence wavefronts. We note C_φ the covariance matrix of the tip-tilt free turbulence wavefronts. Then the problem is to define Q so that:

$$\begin{aligned} Q^T C_\varphi Q &= \Lambda \\ Q^T Q &= I \end{aligned}$$

where Λ is a diagonal matrix and I is the identity matrix.



Thus the covariance matrix of the KL modes is diagonal (first equation) and the basis is orthonormalized (second equation). We denote F the influence function matrix which describes the pixels map of the wavefront front from the control voltage vector. F is an isomorphism between the space of control voltages E_{cv} and E_{wf} . We define B , the matrix of vectors of E_{cv} , so that:

$$Q = FB$$

B is the KL basis expressed in the control voltage space.

We denote Δ the “scalar product” matrix of the influence functions: $\Delta = F^t F$ and G the turbulence covariance matrix of the influence functions: $G = F^t C_\varphi F$.

The simultaneous double diagonalization is obtained with the following procedure:

1. Diagonalize Δ so that $M^t \Delta M = D^2$, where M is the eigenmodes matrix of Δ and D^2 its Eigenvalues.
2. Normalize the eigenvectors M of Δ with respect to the square root of their eigen values:
 $M = M' D^{-1}$
3. Express G in the normalized eigenmodes basis M of the DM: $G' = M^t G M$
4. Diagonalize G' such as $A^t G' A = \Lambda$ where A is the eigen modes matrix of G' and Λ is the eigen values matrix of G' , i.e. of both the DM and the turbulence, A is given in the eigen space of the DM.
5. Express A in the control voltage space leading to $B = MA$.
6. compute the modal basis $Q = FB$.

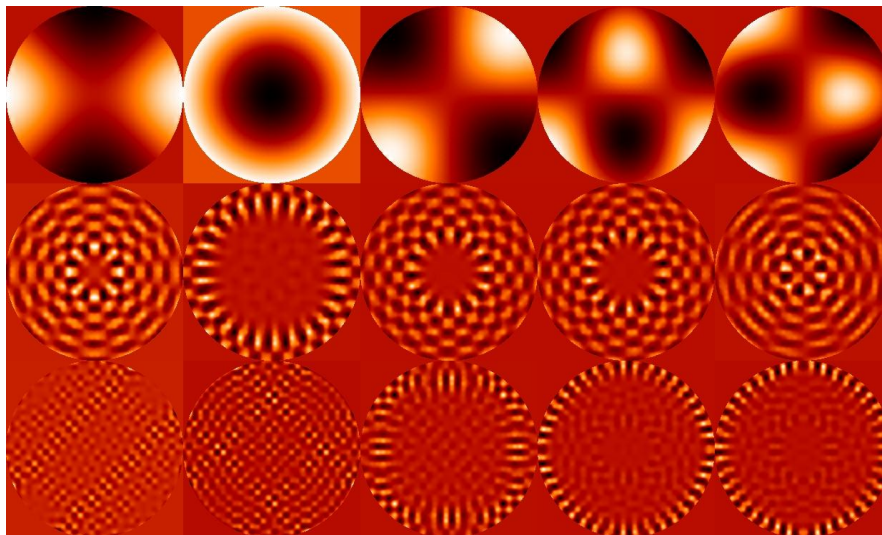


Figure 18. Example of modes for three different range, first row low orders; second row middle order; third row high order.

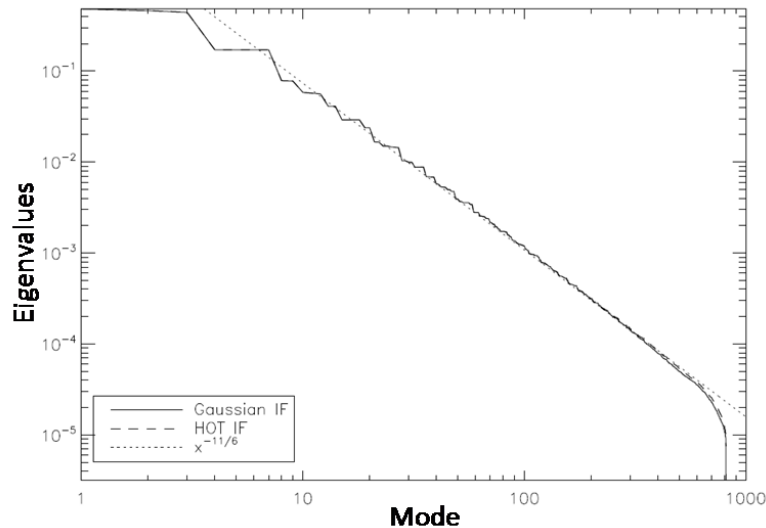


Figure 19. Eigenvalue dependency of the K-L base for Kolmogorov turbulence.

The behaviour is similar for all the actuators (except for the actuators on the edge) and the only difference is the position on the IF matrix. So, a median IF function is calculated using the information from the internal actuators and a second one for the edge actuators. Then this media IF's substitute the individual IF's, keeping the position on the IF matrix. Thus, the errors on the IF measurements are eliminated although minor individual actuator information is lost. This median IF matrix is used as input for the modal base reconstruction

We consider a circular pupil without obstruction perfectly center on the BMM. To choose the valid actuators for the mode computation the pupil is projected on the IF and only the actuators witch effective IF after been cut by pupil reach 50% of the peak of the complete IF are selected. Thus, 812 actuators are considered.

An atmosphere following a von Karman spectrum with $L_0 = 50$ m and $r_0 = 0.2$ m is considered for the computation (piston and tip-tilt removed).

This original modal base B (812 modes) is truncated until the number of modes desired to control. In the standard case we select a modal base matrix of 413 modes. In addition the actuators used to create the modal base are more than the ones controlled on the real pupil (792). The extra non active actuators are removed from the modal base matrix for dimensional reasons.

As for the IM case, an inversion of the modal basis matrix B is required to compute the reconstructor. On this case 10 modes are truncated from the inversion matrix.

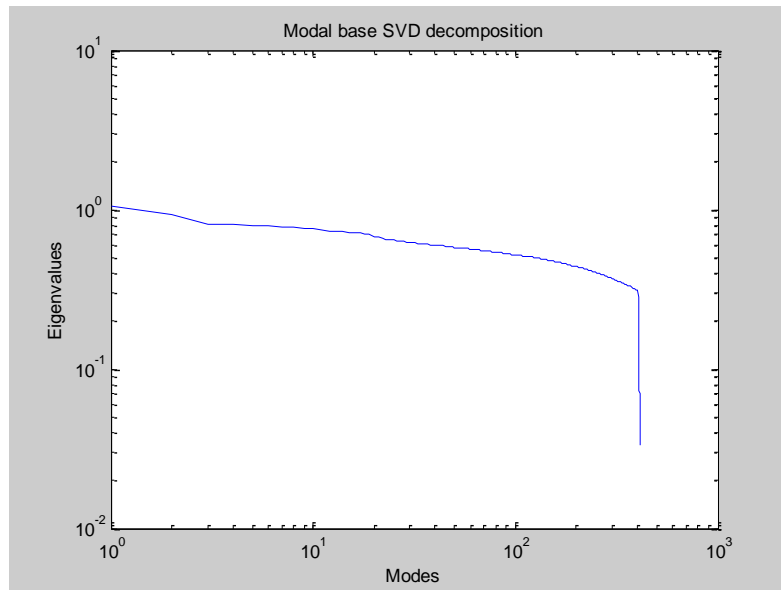


Figure 20. Plot of the eigenvalues obtained from the SVD computation of the modal base B (792 act x 400 modes, condition number 32).

6.8 Slaving

The interactor stroke is only $0.83 \mu\text{m}$. This could be a limitation trying to correct high order modes, since these ones requires higher strokes specially for the actuators on the pupil edge and could produce saturation. To solve this problem we consider as actives a ring of actuators just outside the pupil but they will be controlled as slaves of master actuators inside the pupil. Thus, the effective stroke of master actuators will increase. There are 110 slaved actuators controlled by 70 masters. The master and slave actuators map is shown in Figure 15.

Some modification on the acquired IM are required. Now the effective stroke of the master increase, and the effective IF is the addition of both, master and slave IF. To consider this effect on the IM matrix we add the column corresponding to the slave to the column of the master. This is the final IM matrix considered for inversion on the reconstructor.

In addition, also on the control loop the command calculated for the master will be sent to the slaved actuator.

6.9 Loop control

The RTC control is easily programmable on MATLAB, since it incorporates a package for TCP connection. Thus, the RTC can be implemented under MATLAB since both, slopes acquisition and TTM and BMM, are accessible. Specific routines are implemented for IM acquisition, reconstructor computation and an interactive GUI for close loop control.

The BMM is controlled following a square law displacement vs voltage. In this way, all the BMM commands are always computed on displacement units and only in the moment the commands are sent to the mirror, a set of functions convert the displacement values to voltage units. The delay caused by this additional operation was measured to be negligible.

The voltage range goes from 0 to 200 volt equivalent to -1 to 1 on the HVA control. So, we assume a displacement range from 0 to 1 for the voltage range -1(0volt) → 1(200volt) .

Thus, the equation to convert voltage to displacement and vice versa is:

$$D = \frac{(V + 1)^2}{4}$$

$$V = 2\sqrt{D} - 1$$

On this way, if the input for the Haddamard calibration are on displacement units, the reconstructor will transform slope space on displacement space. Since the IF's are measured as the mirror would have a linear behaviour, with this approx any extra normalization on the IF matrix is required for the modal base creation.

This approximation allowed simplifying the control since the square behavior is transparent and makes easier operations such as the calibration.

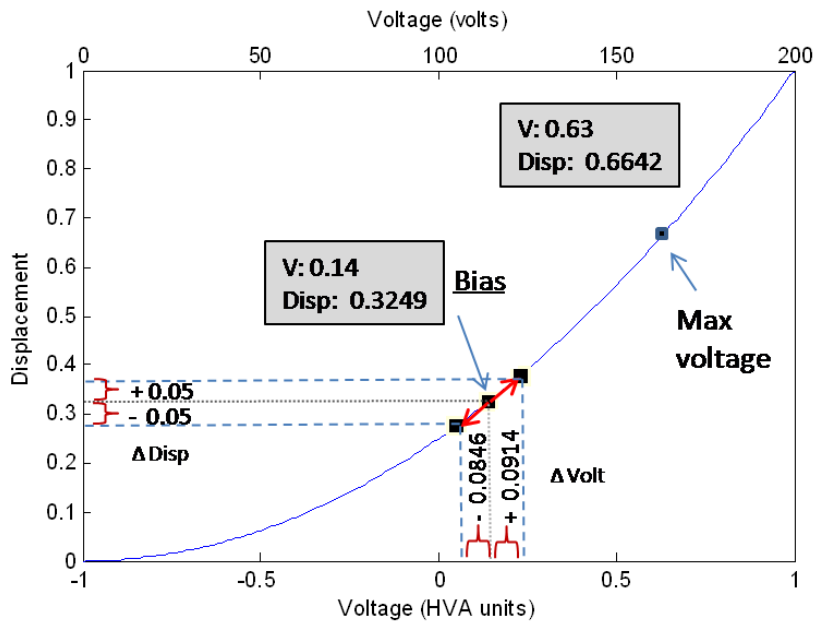


Figure 21. curve showing the quadratic law used for the BMM control. The red arrows show the delta displacement from the bias used for the calibration. A displacement delta of 0.05 is used as input for the Hadamard pattern. The curve returns us the equivalent values in voltage units to apply to the BMM.



HIGH ORDER TESTBENCH
SHS and PWFS comparison test report

Doc:
Issue: 1.0
Date: 18/05/09
Page: 30 out of 80

A simple algorithm is implemented for the loop control. Two devices are controlled simultaneously, the TTM and the BMM. The TTM has two channels for tip and tilt correction, so the BMM modal reconstructor is piston and tip-tilt free. An IM for the TTM is measured on the calibration (in this case actuators and modes commands are equivalent) and the TTM reconstructor is obtained through a simple inversion. The tip and tilt commands are calculated from the WFE measured using this reconstructor. Then we calculate the residual WFE after removing the tip and tilt contribution. Finally, the BMM commands are computed applying the modal reconstructor to this residual WFE.

The commands computation is done through a common integrator controller modified with a simplified anti-windup circuit with gain 1 and using the modal reconstructor.

The loop parameters (gain, speed, reconstructor, bias ...) are controlled by a matlab graphical interface. In addition, the GUI lets us visualize the TTM position and voltage pattern apply along the loop, apply offsets and records slopes sequence. The control interface under matlab is quite heavy on computation time, as result, the maximum loop speed is ~65 Hz (without recording slopes data it could reach 85 Hz).



7 Pyramid wave front sensor

7.1 Introduction

The Pyramid wave front sensor (PWFS) (RD12, RD13, RD14) used in the HOT experiment is a PWFS with tilt modulation (RD15) designed by INAF – Osservatorio di Arcetri. As for the SHS, there are 31 sub-apertures across the pupil diameter and is using the detector 128x128 pixel electron multiplying CCD Andor iXON L3 (AD12). In Figure 22 is reported a sketch of the optical configuration and a picture of the PWS. All the design details can be found in AD 15.

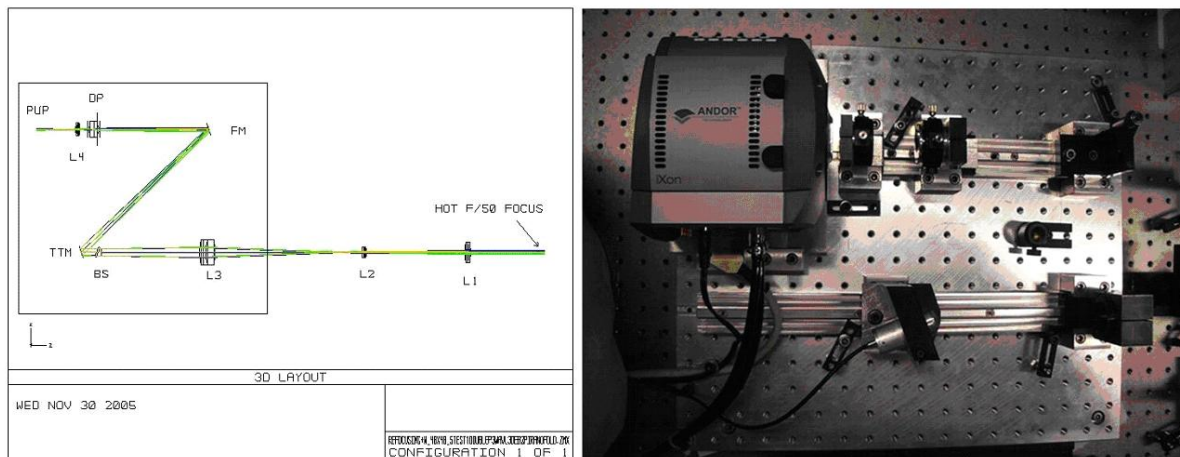



Figure 22. (Left): The Zemax optical scheme of the PWFS. The HOT main bench focus is located in the bottom-right and is feeding a refocusing system (L1 and L2) that changes the F/ from F/50 to approx F/15. Then L3 is creating an image of the pupil on the tip-tilt mirror (TTH). After a folding on a plane mirror (FM), the beam is focused on the glass pyramid (DP) and hits the camera lens (L4) that creates 4 pupil images on the sensor plane (PUP). (Right): A picture of the PWFS installed on the HOT bench. The box on the top-left is the L3 CCD camera.

7.2 Optical Alignment

In this section we describe the procedure done to obtain the fine alignment of the PWFS on the HOT bench, supposing that the sensor's internal alignment and a first alignment on the bench have been already performed. That means that we consider to have the optical beam passing through the sensor's optical elements within an accuracy of $\sim 1'$ in angle and 0.2mm of displacement with respect to the ideal sensor's optical axis.

The goal of the fine alignment is to reach the desired matching between BMM actuators and sensor subapertures. As for the SHS, the Fried geometry needs to be met. In order to achieve this, the magnification of the pupil image on the CCD had to be adjusted so that the

	HIGH ORDER TESTBENCH SHS and PWFS comparison test report	Doc: Issue: 1.0 Date: 18/05/09 Page: 32 out of 80
---	--	--

actuator pitch (d_{act}) matched the size of one sensor subaperture (d_{sa}). Moreover, each BMM actuator had to be imaged on the intersection of four sensor subapertures. All of this can be translated into requirements on the pupil image magnification ($r = d_{act}/d_{sa} = 1$), shift ($0.1 d_{sa}$) and rotation ($0.1 d_{sa}$ corresponds to $\approx 2^\circ$) of the actuator grid with respect to the CCD pixel grid.

7.2.1 Magnification and rotation correction

The pupil acquisition techniques reported in section 7.3 allow to measure the pupil image diameter on the CCD but do not guarantee that $r=1$, and they are also insensitive to the rotation. A dedicated measurement has been performed in order to measure r with an accuracy of 3%. This was achieved by moving each single actuator belonging to a column of the BMM and recording a CCD frame when the i^{th} actuator is pushed up ($f_u(i)$) and down ($f_d(i)$). Then, for each actuator we computed $f(i) = f_u(i) - f_d(i)$ (see Figure 23) and we detected the position (x,y) of the maximum (or minimum) of $f(i)$ for each of the four pupils. If $r = 1$, we expect to have $y(i) = c \pm i$, where c is an arbitrary constant. Otherwise, if $r > 1$ or $r < 1$, $y(i)$ shows jumps in opposite directions. Examples of these measurements are shown in Figure 24. Once a wrong value of r is measured, the magnification can be adjusted by moving the sensor's camera lens along the optical axis and consequently adjusting the CCD position on the new pupil's image plane.

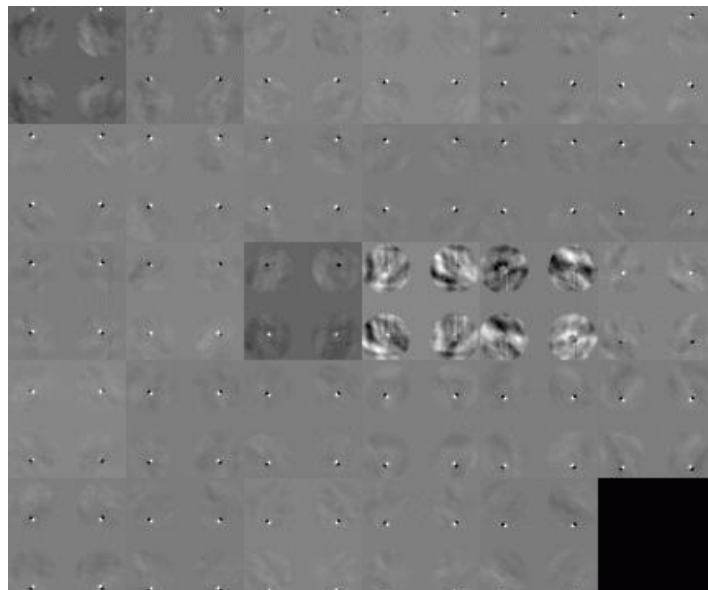


Figure 23. In the picture are shown the difference between the frames when each single actuator of a column is pushed up and down ($f(i)$). The four pupils are present in each frame. In each pupil are easily recognizable the maximum and minimum of intensity due to the light flux unbalance caused by the moved actuator. Note that the effects of the central actuators are not visible because they are hidden by the pupil's central obstruction.

Regarding the rotation, we expect $x(i)$ to be constant if the rotation error between actuator and pixel grids is below $1/30 \text{ rad} \sim 2 \text{ deg}$ (see Figure 25). In the case of a measured misalignment the CCD or the BMM has to be rotated with respect to the optical axis.

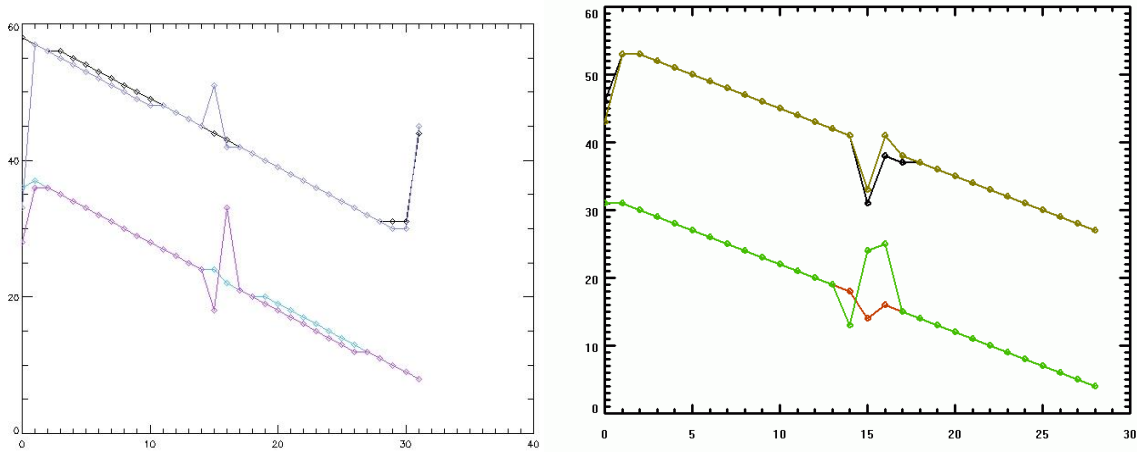


Figure 24. In the vertical axis are reported the vertical positions (in pixels) of the maximum of intensity ($y(i)$) for the four pupils (different colors) as a function of the moved actuator (i) (horizontal axis) of a single column of the BMM. The left plot shows the typical behaviour when the ratio $r = d_{act} / d_{sa} < 1$ of about $1/30$: the dependency is not straight, as expected, but present a single jump in all the four curves. The right plot shows the same measurement when $r = 1$ within $1/30$.

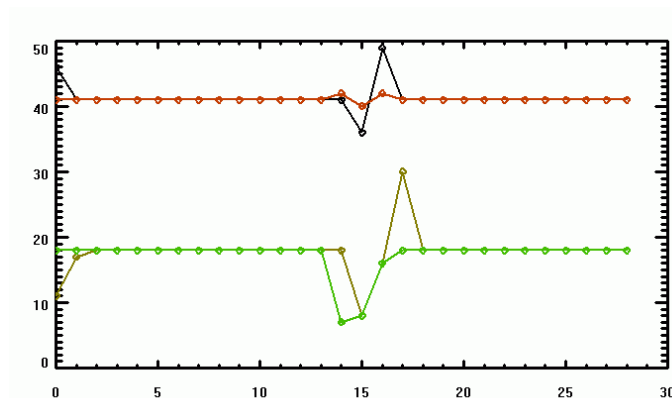


Figure 25. Similarly to Figure 24, here are reported the horizontal positions (in pixels) of the maxima for each of the four pupils. All the maxima on each pupil have the same horizontal coordinate, meaning that the relative rotation between the pixel and actuator grids is lower than 2 degrees.

7.2.2 Shift correction

Using the Fried geometry, the maximum relative shift ($0.5d_{sa}$) between the actuator and pixel grids, as well known, drives the sensor insensitivity to the waffle mode. So, the shift can be detected applying the highest spatial frequency modes on the deformable mirror. In order



HIGH ORDER TESTBENCH
SHS and PWFS comparison test report

Doc:
Issue: 1.0
Date: 18/05/09
Page: 34 out of 80

to disentangle the shifts in x and y directions, we applied separately two different patterns to the BMM. The patterns were created simply pushing up and down alternately actuator columns (for x shift) and rows (for the y shift). Once one of the pattern is applied to the BMM, a series of CCD frames are recorded for different grid shift values. The grid relative shift can easily be changed on the PWFS using the cinematic mount of the camera lens. For a small displacement, the camera lens x - y movement simply translates the pupil image plane with respect to the CCD pixel grid. Sampling in this way a range of d_{sa} in both axis, the best shift position can be identified maximizing the contrast on the pupil images.

Of course the best contrast is simultaneously achieved on the four pupil images for the same grid shift, under the hypothesis that the four pupil centres are separated by an integer number of pixel in both axis. By 'integer' we mean within the accuracy we want to correct the shift, let's say about $0.1 d_{sa}$. Unfortunately one of the four faces of the pyramid presents a wrong basis angle. The difference between this angle and the other three generates a misplacement of the corresponding pupil image. The positions of the pupil images on the CCD have been measured with the method described in section 7.3 and the resulting pupil positions are reported in Table 2. The estimated centre positions show that particularly one of the pupils (#3) has a distance to the others differing from an integer value of 0.4 and 0.3 in the x and y axis respectively. This prevented the achievement of the optimal shift in both axis.

After the polishing of the HOT-PWFS pyramid, a new technique of angle control has been identified, allowing the correct pupil arrangement on the CCD plane within a error of $0.1 d_{sa}$, as demonstrated on the PWFS developed for the LBT adaptive optics system. In case of HOT follow-up a new and corrected pyramid could be installed substituting the one used for the described experiment.

Pup #	Radius (pix)	Centre x position (pix)	Centre y position (pix)
1	20.23	39.88	39.33
2	20.21	40.04	81.00
3	20.12	81.74	39.33
4	20.14	82.12	81.16

Table 2. In the table are reported the pupil radii and the coordinates of the centres on the CCD pixel grid (A CCD frame showing the location of the four pupils is presented in Figure 26a). These values have been estimated using the pupil registration procedure described in section 7.3.



7.3 Pupil acquisition and signal computation

The pyramid x- and y- signals are computed from the four pupil images [Figure 26(a)] formed on the CCD —denoted as $I_i(x, y)$ where $i=\{1,2,3,4\}$ — as follows :

$$s_x(x, y) = \frac{I_3(x, y) + I_4(x, y) - I_1(x, y) + I_2(x, y)}{\bar{I}}$$
$$s_y(x, y) = \frac{I_1(x, y) + I_3(x, y) - I_2(x, y) + I_4(x, y)}{\bar{I}}$$

where \bar{I} is the average intensity per subaperture:

$$\bar{I} = \frac{1}{n_s} \sum_i \sum_{x,y} I_i(x, y)$$

and n_s is the number of subapertures. The coordinates (x, y) of the four pixels (one on each pupil image) associated with each subaperture needs to be determined beforehand. This mapping is known as *pupil registration*, and will be briefly described below.

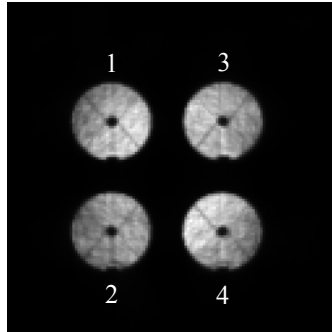
As a first step, a long-exposure CCD frame is acquired [Figure 26(a)] at a high modulation amplitude in order to minimize diffraction and static aberration effects, and obtain a more uniform illumination across the pupil images. Then, the center coordinates of each of the four pupil images are estimated. Once the centers are found, it is possible to determine the coordinates of the four pixels associated with a given subaperture.

The next step in the pupil registration procedure is to determine the *valid subapertures*. We have developed two different approaches to do this. The first one consists in estimating the radius R of the pupil image (in pixel units) from the CCD frame mentioned above, and defining as valid all subapertures within the circle of radius R . This method has the disadvantage that some dimly illuminated subapertures (e.g. at the perimeter of the circle, or behind the central occultation) will be also selected. To avoid this problem, we developed a second method to determine the valid subapertures based on a subaperture by subaperture analysis, as outlined below.

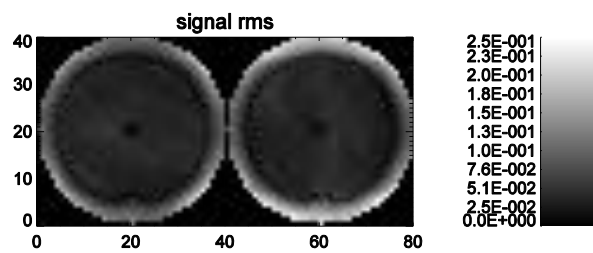
The second method to determine the valid subapertures is illustrated in Figure 26. As a first step, the pyramid signals rms is computed from a set of N frames for all the subapertures within a much larger circle of radius R' [Figure 26(b)]. Then, the ratio between the signal rms and the mean intensity per subaperture, σ/I , is computed [Figure 26(c)]. Note that dimly illuminated subapertures exhibit a large ratio σ/I value. Finally, valid subapertures are selected as those ones whose ratio values are below a selected threshold [Figure 26(d)]. A total of **730 valid subapertures** were selected in this way.



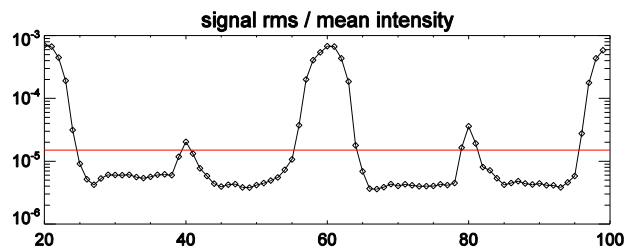
(a)



(b)



(c)



(d)

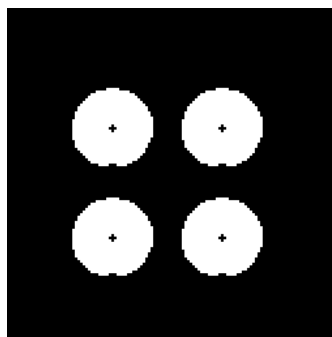



Figure 26. Pupil registration process. (a) CCD frame showing the four pupil images $I_i(x, y)$, $i = \{1, 2, 3, 4\}$. (b) x- and y- signal rms computed from N CCD frames over a much larger circle of radius R' . (c) Profile along the center showing the ratio between signal rms and mean intensity per subaperture, σ/I . A threshold of 1.5×10^{-5} is shown in red. (d) Map of valid subapertures (a total of 730) obtained with the threshold shown in figure (c).

	HIGH ORDER TESTBENCH SHS and PWFS comparison test report	Doc: Issue: 1.0 Date: 18/05/09 Page: 37 out of 80
---	--	--

7.4 Modal control

In this section we will describe the way the modal basis was created. Basically, the selected modes were computed from Karhunen-Loeve (KL) modes projected onto the BMM influence functions. Tip and tilt modes were controlled with the TT mount of MACAO. Several intermediate steps were required to ensure the good performance and stability of the final modal basis, as we will describe below in detail.

7.4.1 Computation of pure KL modes

KL functions do not have analytic expressions but they can be expressed as a linear combination of Zernike modes by diagonalization of the Zernike covariance matrix given by Noll. We have assumed a Kolmogorov turbulence and a normalized turbulence strength of $D/r_0 = 1$ in the computation of the Zernike covariance matrix. Piston mode was also included but its variance (in theory infinity) set to a large value. Note that at this point Zernike modes are defined on a circular pupil without central occultation.

A large number of Zernike modes was required to generate properly a given set of KL modes. For instance, as seen in Figure 27, more than 4000 Zernike modes were required to generate accurately about 2000 KL modes. We will consider just a subset of these KL modes. As we will discuss further below, we will require in the end less than 700 KL modes in the creation of our final modal basis.

These KL modes are orthogonal on a circular pupil without central occultation. Hence, we needed to re-orthonormalize these modes on a circular pupil with a central occultation whose diameter is 14% of the pupil diameter, as in the actual pupil mask.

Finally, it was required to filter out the tip and tilt components from the KL modes. The tip and tilt modes will be actually controlled with the TT mount of the MACAO DM, and considered separately. The *pure* tip/tilt-free KL modes are ready to be projected onto the BMM influence functions.

7.4.2 Matching the BMM optical alignment

The 1024 BMM influence functions (IFs) were measured at ESO with a FISBA interferometer. It is important to make sure that the relative positions of the IF measurements with respect to the pupil mask match the actual BMM optical alignment. This was actually done from the analysis of the laboratory image shown in Figure 28(Left), in which a symmetrical set of actuators was activated, and from which it was possible to estimate the relative displacements, the pitch scale, and the diameter of the pupil mask. Figure 28(Right) shows an equivalent image generated with the measured IFs and with the pupil mask superimposed at the right position with the estimated size (in this case 30.3 pitches in diameter).

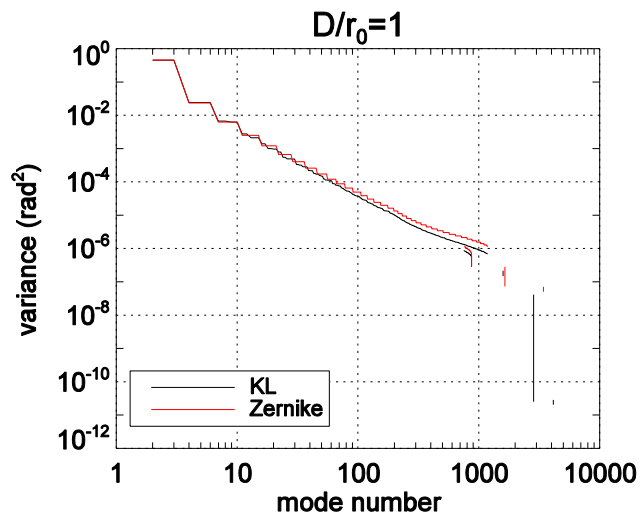


Figure 27. Variance of Zernike and KL modes for Kolmogorov turbulence ($D/r_0 = 1$). Note that the last KL modes do not follow the required statistics. A larger set of Zernike modes would be required to compute accurately these last KL modes.

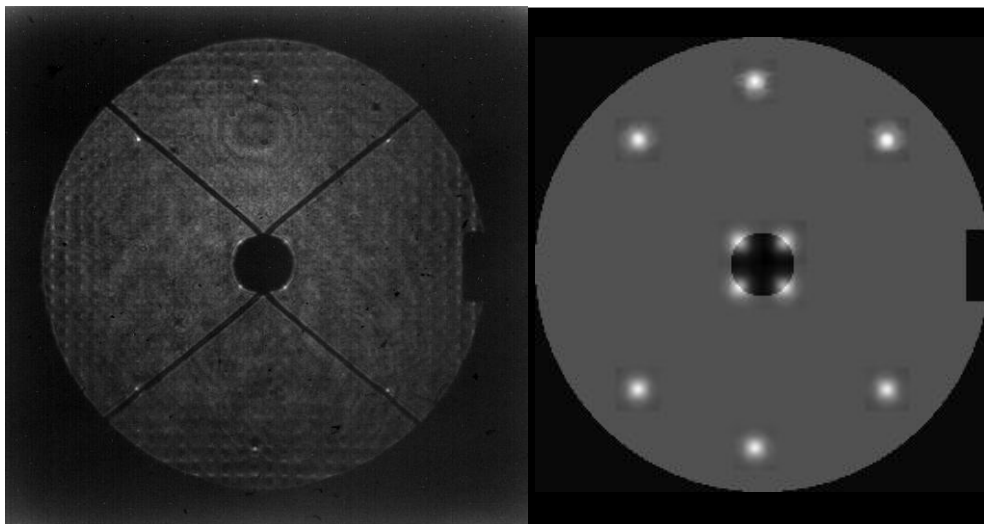



Figure 28. (Left) BMM image with a set of 10 activated actuators required to align the BMM with respect to the pupil mask. (Right) Equivalent image generated with the measured influence functions. The pupil mask (including the additional rectangular region, but not the spiders) is also superimposed at the right position determined from the analysis of the experimental image.

	HIGH ORDER TESTBENCH SHS and PWFS comparison test report	Doc: Issue: 1.0 Date: 18/05/09 Page: 39 out of 80
--	--	--

7.4.3 Selection of independent, master and slave actuators

We now need to decide which actuators are going to be controlled, and how they are going to be controlled (either as an independent actuator, a master, or a slave). We used two different strategies to take this decision, as we will describe below.

The first strategy uses the IF measurements available. Indeed, once we have estimated the actual pupil mask characteristics (i.e. size and position with respect to the IF measurements) as described in section 7.4.2, we can determine which actuators lie within the pupil mask. Following this approach, slaves could be selected as those actuators for which the 50% of their influence function's FWHM lied outside the pupil mask.

The second strategy is based on the analysis of the response of each actuator on the pyramid sensor signals (i.e. a zonal interaction matrix), as shown in Figure 29. In this case, those actuators that produce a peak-to-valley WFS response above a predefined threshold are considered to be independent.

We should note that the final number of slaves is a critical parameter that requires some trial and error (aided with numerical simulations or laboratory experiments). Indeed, if an actuator which was considered to be independent saturates often during the closed-loop operation, then it is actually better to turn it into a slave.

Figure 30(Left) shows an example of a set of controlled actuators selected using the second method described above. A total of 821 actuators were selected. From this set of actuators a total of 88 (shown in dark in the figure) were defined as slaves. The corresponding master actuators are also indicated in the figure. The master for each slave was selected as the closest independent actuator in the radial direction. Note that some masters may have more than one slave. Finally, note that a total of 686 independent actuators resulted in this configuration.

The master-slave information can be expressed in a $n_{act} \times n_{ind}$ matrix, where n_{ind} is the number of independent actuators and n_{act} is the total number of controlled actuators. This *slaving matrix* is a sort of diagonal matrix, as shown in Figure 30(Right). The j-column is associated with the j-independent actuator. If the j-actuator is a master, there will be an additional '1'-value at the row associated with the corresponding slave.

As we will outline in the next section, slave-master information is included in the modal basis. We verified (both with numerical simulations and with laboratory experiments) that this approach can effectively reduce the saturation of border actuators, as it happens when no-slaving control, or when the slaving information is not taken into account in the creation of the modal basis.



HIGH ORDER TESTBENCH
SHS and PWFS comparison test report

Doc:
Issue: 1.0
Date: 18/05/09
Page: 40 out of 80

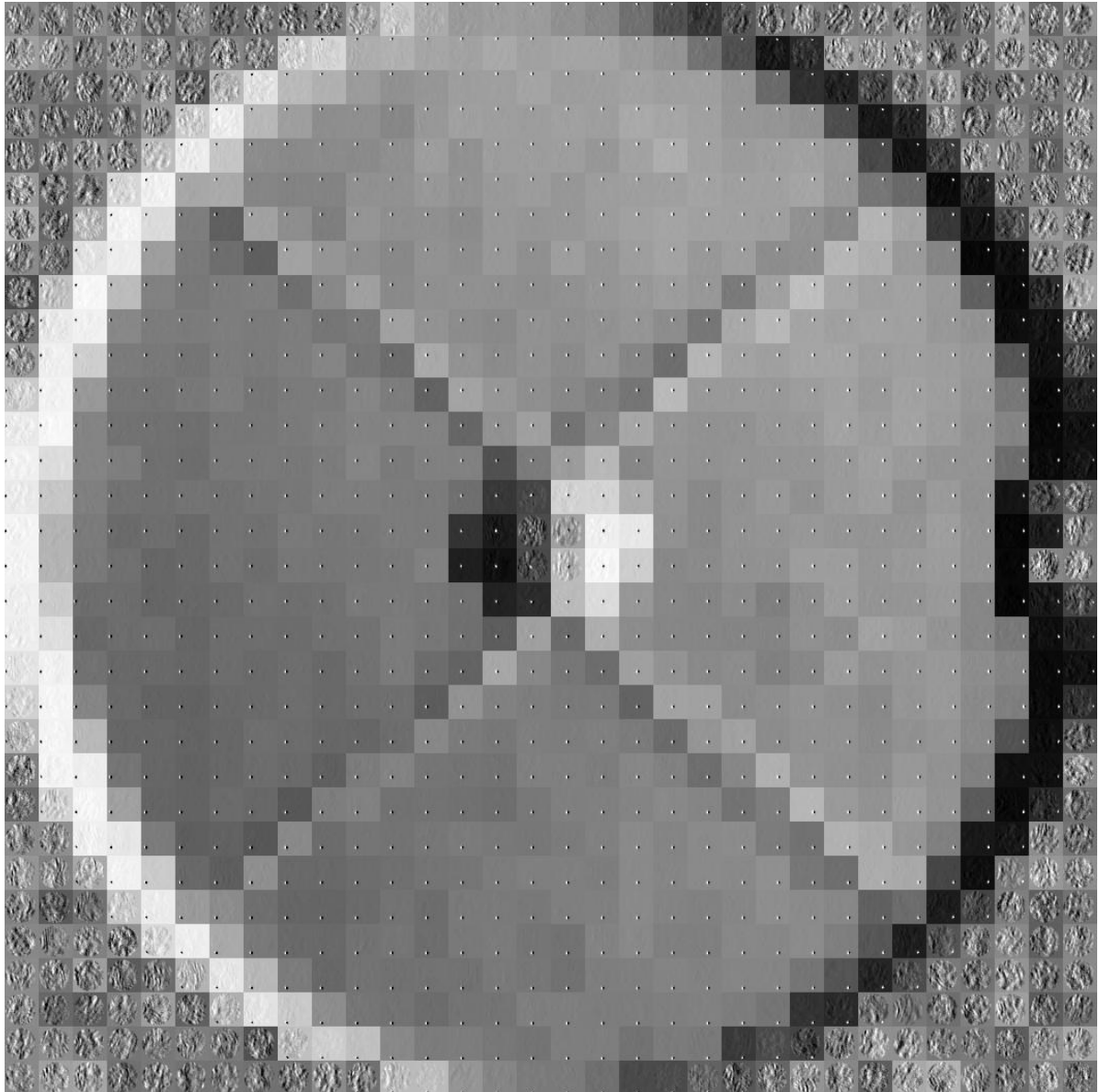


Figure 29. Representation of the pyramid sensor signals (x-slopes) obtained when each of the 1024 actuators is commanded at a time. The position of the sensor signal within the 32x32 grid indicates to which actuator it is related. Each signal display has been rescaled. Note that those signals associated with the actuators totally out of the pupil show just local turbulence.

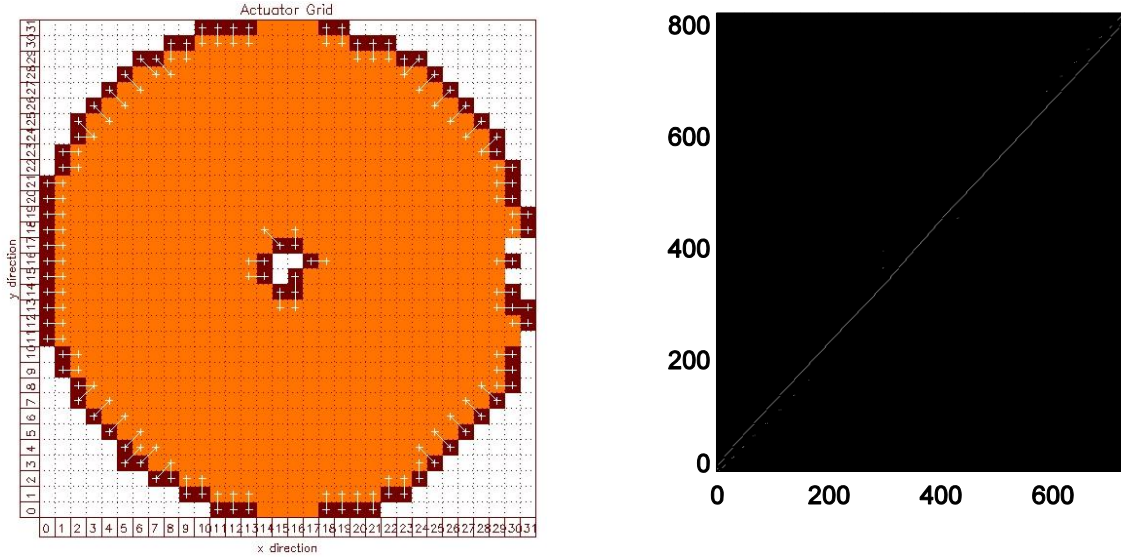


Figure 30. (Left) 32x32 actuators grid showing in color a total of $n_{act}=821$ selected actuators. The 88 slave actuators are shown in dark color, and their respective masters are indicated with a link. A total of $n_{ind}=686$ independent actuators resulted in this configuration. (Right) The 821x686 matrix representing the master-slave relationship for this configuration. Black represent a '0'-value whereas white represents a '1'-value.

7.4.4 Fitting of pure KL modes by the BMM influence functions

We will outline in this section the procedure followed to project the pure KL modes onto the BMM influence functions. It is important to note that all BMM influence functions must be expressed in displacement units per squared-Volt in order to take into account the quadratic-law behaviour of the BMM (section 6.9).

Considering that the influence functions and the pure KL modes are sampled in a grid of $n_{pix} \times n_{pix}$ pixels, we can define the *pure KL matrix* \mathbf{K} as a $n_{pix}^2 \times n_{mod}$ matrix containing the n_{mod} KL modes to be projected, and the *influence matrix* \mathbf{N} as a $n_{pix}^2 \times n_{act}$ matrix containing the influence functions of all the controlled actuators. Denoting \mathbf{S} the *slaving matrix* defined in section 7.4.3, we can compute the effective influence matrix \mathbf{N}_1 as:

$$\mathbf{N}_1 = \mathbf{N}\mathbf{S}. \quad (1)$$

Note that the size of \mathbf{N}_1 is $n_{pix}^2 \times n_{ind}$. The projection of the pure KL modes onto the BMM influence functions is computed as:

$$\mathbf{M}_f = \mathbf{N}_1^\dagger \mathbf{K}, \quad (2)$$

where (\dagger) denotes the generalized inverse. \mathbf{M}_f is an $n_{ind} \times n_{mod}$ matrix; the j -column of \mathbf{M}_f contains the BMM commands vector to be applied in order to produce the "best fit" of the j^{th} mode. The shape of the fitted modes can be computed as:

$$\mathbf{K}_f = \mathbf{N}_1 \mathbf{M}_f, \quad (3)$$



where the size of \mathbf{K}_f is clearly $n_{pix}^2 \times n_{mod}$. The cross-product matrix of the fitted modes is computed as:

$$\Delta_f = (1/n_p) \mathbf{K}_f^T \mathbf{K}_f, \quad (4)$$

where n_p is the total number of pixels within the pupil mask. It is important to realize that the orthonormality of the fitted KL modes is no longer guaranteed (Figure 31). Therefore, the fitted KL modes need to be re-orthonormalized on the pupil mask. Since Δ_f is a positive-definite matrix, its Cholesky factorization can be expressed as:

$$\Delta_f = \mathbf{L} \mathbf{L}^T, \quad (5)$$

where \mathbf{L} is a lower-triangular matrix. It should be clear that the final number of re-orthonormalized modes (n'_{mod}) should be limited to $n'_{mod} \leq n_{ind}$; otherwise the Cholesky factorization do not converge. The shapes of the orthonormal fitted modes, \mathbf{K}_{fo} , can now be computed as:

$$\mathbf{K}_{fo} = \mathbf{K}_f (\mathbf{L}^{-1})^T, \quad (6)$$

and, similarly, the matrix containing the BMM command vectors that produce these modes can be computed as:

$$\mathbf{M}_{fo} = \mathbf{M}_f (\mathbf{L}^{-1})^T. \quad (7)$$

Of course, the number of fitted modes considered in \mathbf{K}_f and \mathbf{M}_f are limited to n'_{mod} . The piston mode, which was also considered in the fitting process described above, can now be eliminated. We should emphasize that the rest of the modes in \mathbf{K}_{fo} are by construction orthogonal to piston. As a consequence, the modal control implemented in this way becomes piston-free.

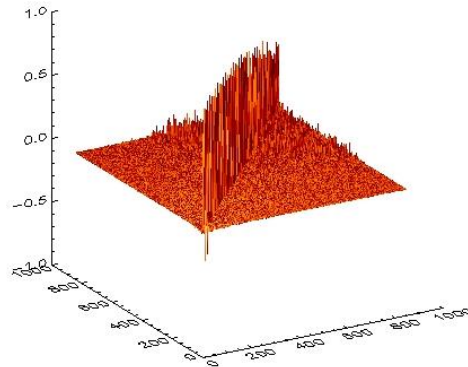



Figure 31. Cross-product matrix (Δ_f) of a set of 850 fitted KL modes using the actuator's configuration presented in Figure 30. Note that the matrix is not equal to the identity matrix putting in evidence the non-orthonormality of these fitted modes.

	HIGH ORDER TESTBENCH SHS and PWFS comparison test report	Doc: Issue: 1.0 Date: 18/05/09 Page: 43 out of 80
---	--	--

Based on this procedure to create a modal basis, and using the actuator's configuration presented in Figure 30, we computed a total of 665 orthonormal modes. As an example, some of these modes are shown in Figure 32.

7.5 Pyramid's tilt modulation

The pyramid's tilt modulation is used to adjust the sensor's sensitivity. It plays an important role in the system optimization process versus seeing. Unfortunately, a differential focus between the alternative source (used for interaction matrix acquisition) and the standard source (used with the turbulent phase screens) was present on the HOT set-up. The focus of the sensor has been optimized for the standard source. Hence, a static defocus was always present during the interaction matrix acquisition. In order to keep the sensor in the linear regime, the modulation had to be increased up to the value of $20\lambda/D$. Interaction matrices with lower modulation amplitudes were not possible to acquire. Since theoretical considerations show that the optimized tilt modulation values are of the order of few λ/D , we decided not to explore modulation values higher than $20\lambda/D$.

As a consequence, we maintained the modulation fixed to $20\lambda/D$ for all the experiments presented in this report.

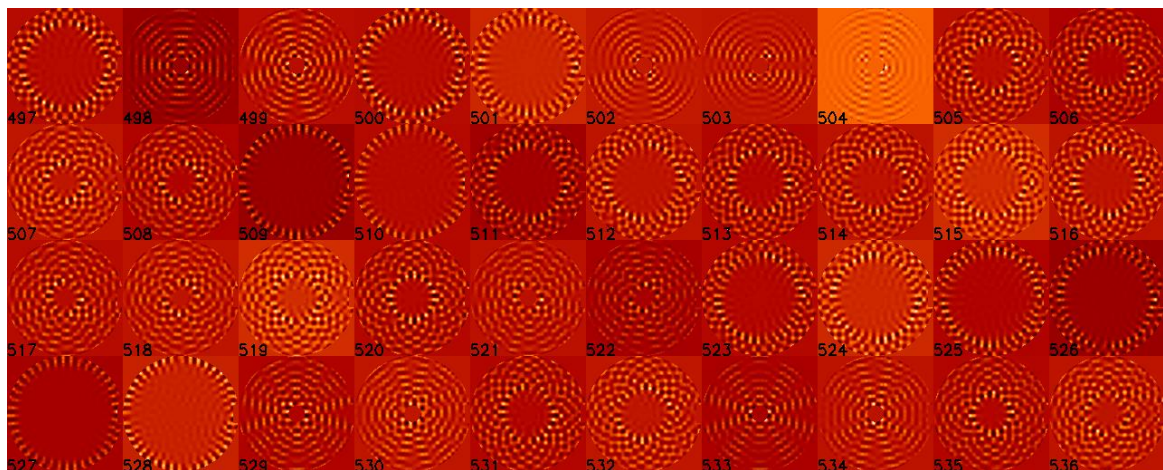
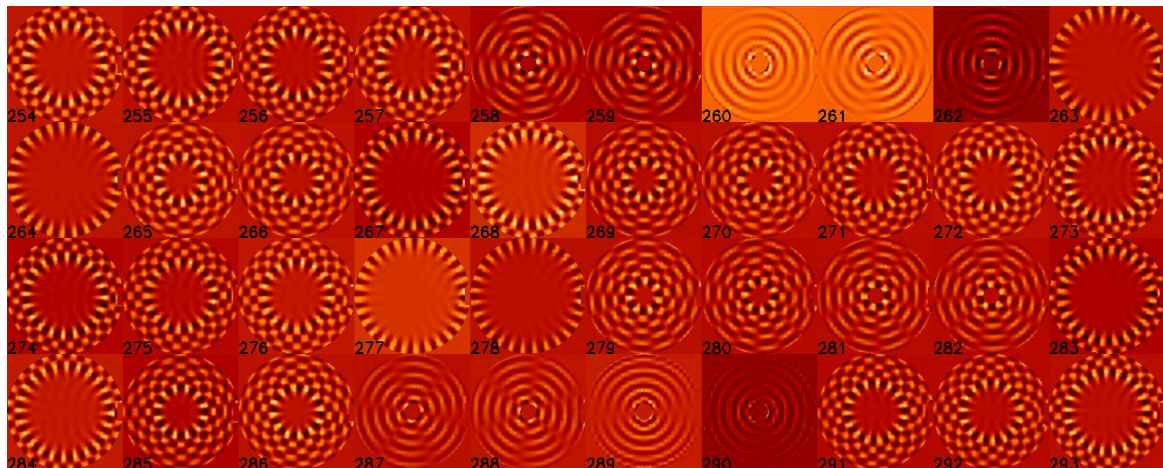
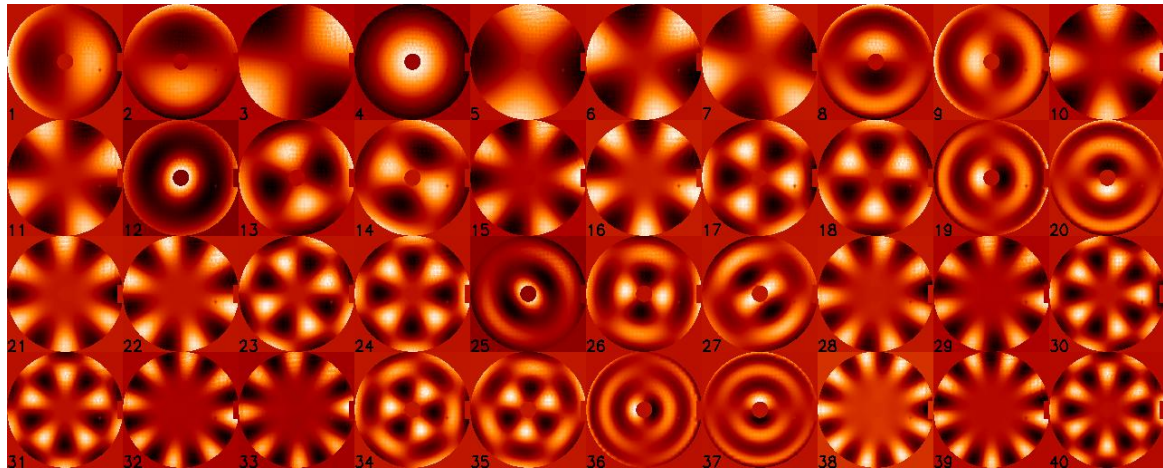


Figure 32. Example of some piston/tip/tilt-free KL modes fitted by the BMM using the actuator's configuration shown in Figure 30 and re-orthonormalized on the pupil mask.



7.6 Interaction matrix acquisition

We have decided to calibrate directly the system's *modal* interaction matrix. Once the modal basis has been created, the modes can be applied to the BMM using the “*modes to commands*” matrix \mathbf{M}_{t0} defined in equation (7). Recall that the modes generated by the BMM are tip-tilt free. The tip and tilt modes are corrected with the TT mount of MACAO, and the corresponding interaction matrix has also been acquired with the method described below.

The j^{th} column of the interaction matrix, denoted as $IM(j)$ and corresponding to the sensor signal vector S associated with the j^{th} mode (\mathbf{m}_j), was computed as:

$$IM(j) = \frac{S(+A\mathbf{m}_j) - S(-A\mathbf{m}_j)}{2A} \quad (8)$$

where A is an amplitude factor. Note that in this way, the signal due to the static aberrations are filtered out, as long as the signal due to the static aberration plus the measured mode \mathbf{m}_j is kept in the linear range.

Special attention has been made to the calibration of higher-order modes. It is important to recall that the pyramid signals are, as a first approximation, proportional to the first-derivative of the wavefront. Hence, higher signal amplitudes are expected from higher-order modes due to their stronger local gradients. In order to prevent signal saturation we decided to scale the amplitude A as the square root of the mode number j . This scaling was done up to mode 200. After this mode a constant amplitude was applied.

The interaction matrix was calibrated using the *alternative source* (no phase-screen distortions present). However, to avoid optical disturbance due to lab local convection, slow drifts of the set-up, and all other possible slow perturbations, we took the positive and negative measurements mentioned above as short exposures one after the other. Then, several couples of measurements were taken and their difference averaged to provide a better estimate of the measured signal vector. In our case, the short-exposure time was set to 10ms. The time delay between short exposures varied between 30ms and 150ms.

As an example, Figure 33 shows the measured pyramid signals $[s_x, s_y]$ corresponding to the first 40 modes shown in Figure 32. A total of 10 short exposures were taken for each signal. The time required to acquire each signal was about 2 seconds. Hence, for a total of 667 modes (665 BMM fitted modes + tip and tilt), the time required to calibrate a full interaction matrix was approximately 20 minutes.

Finally, the reconstruction matrix was computed as the generalized inverse of the full (BMM+TT) interaction matrix.

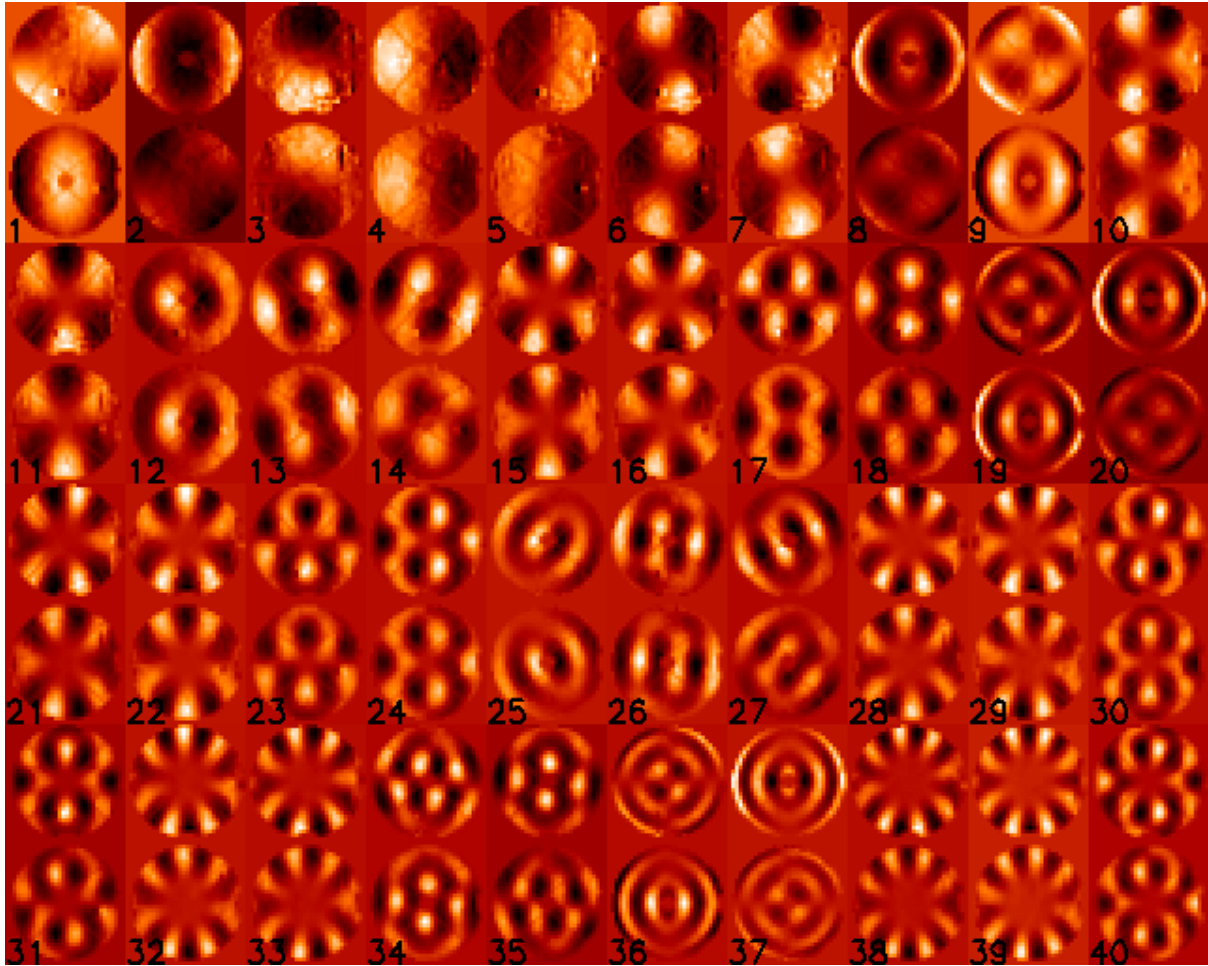


Figure 33. Example of pyramid signals corresponding to the first 40 BMM fitted modes shown in Figure 32. Both x- and y- signal patterns are shown for each mode.

7.7 Control loop analysis

7.7.1 Loop control implementation

The real-time computer (RTC) was implemented using a commercial PC running Linux. While not a strictly real-time system, this proved to be sufficient to control the CCD and the mirrors up to 82 Hz, with a small jitter of ± 1 Hz. The real-time control software was programmed in C while the user interface and the calibration procedures were written in Python to allow flexible modifications.

Both the BMM and the TTM were controlled through a TCP connection. The total time delay was roughly estimated by applying a step command to each mirror and measuring the time after which the response was seen on the CCD. In this way, the total time delay was estimated to be about 2 frames.



A quadratic voltage control is required for the BMM. This was also implemented in the pyramid's RTC following the procedure outlined in section 6.9.

The RTC was able to save at full speed the temporal sequences of CCD frames, sensor signals, and mirror commands. As we will discuss below, we used this set of data to evaluate the performance of the system.

7.7.2 Performance metrics and system parameters

We will summarize in this section the performance metrics used to evaluate the performance of the HOT system using the pyramid wavefront sensor. Based on the acquired real-time data (i.e. sensor signals and mirror commands) we estimated the following performance metrics:

- Sensor signals rms
- Commands saturation (percent of saturation time)
- Modal variance distribution in open and closed loop
 - Residual phase variance (σ_ϕ^2), estimated as the sum of the closed-loop (residual) modal variances plus a fitting-error term.
- Rejection transfer functions (RTFs)
 - Correction bandwidth (BW), defined as the frequency at which the rejection transfer function (RTF) reaches 0dB.

Details on how these performance metrics were estimated will be discussed in the following sections. We should note that these metrics are useful to evaluate the performance without looking directly at the image on the infrared camera.

The free system parameters that were tuned to optimize the performance were:

- Number of controlled modes
- Sampling frequency
- Integrator controller's gain

It is important to recall that the effect of the tilt modulation on the system performance could not be investigated for the reasons explained in section 7.5.

7.7.3 Effect of the number of controlled modes

We will evaluate in this section the system performance —signal rms, and residual phase variance— as a function of the number of controlled modes (667, 595, and 406) for the modal basis built on the actuator's configuration shown in Figure 30.

The open-loop and closed-loop time sequence of each mode can be computed from the acquired slopes and the modal reconstructor. The residual (phase) variance, σ_ϕ^2 , can be estimated as the sum of the closed-loop modal variances. However, in order to compare the residual variance of loops using a different number of modes, we added a 'fitting error' term extracted from the open-loop modal variances, as stated below:

$$\sigma_\phi^2 = \sum_{j=1}^n \sigma_{CL,j}^2 + \sum_{j=n+1}^m \sigma_{OL,j}^2 \quad (9)$$



where $\sigma_{CL,j}^2$ and $\sigma_{OL,j}^2$ denote, respectively, the closed-loop (residual) and the open-loop (turbulence) variance of the j^{th} mode; n denotes the number of controlled modes, and m denotes the maximum number of modes available (in the present case $m=667$).

The flux level was set to the maximum, the sampling frequency was set to 82Hz, and the integrator's gain was set to either 0.8 or 0.6. Table 3 presents a summary of the experimental results, and the modal variances for some of the considered cases are shown in Figure 34. Note that the best performance (minimum signal rms and residual variance) is attained with 667 modes and $g=0.8$. However, note that some anomalous peaks appear on some of the highest modes (Figure 34).

Let us now analyse the performance in terms of command's saturation. As shown in Figure 35, note that in the case of 667 modes the set of actuators at the upper pupil border are always saturated. Reducing the number of controlled modes to 595 solves the saturation problem in this region. Another set of actuators at the upper-right border becomes now the most saturated ones, but not dramatically (saturation time $<9\%$ of the total closed-loop time). Reducing further the number of controlled modes to 406 does not change the overall saturation time (the most saturated actuator becomes now one located besides the central occultation).

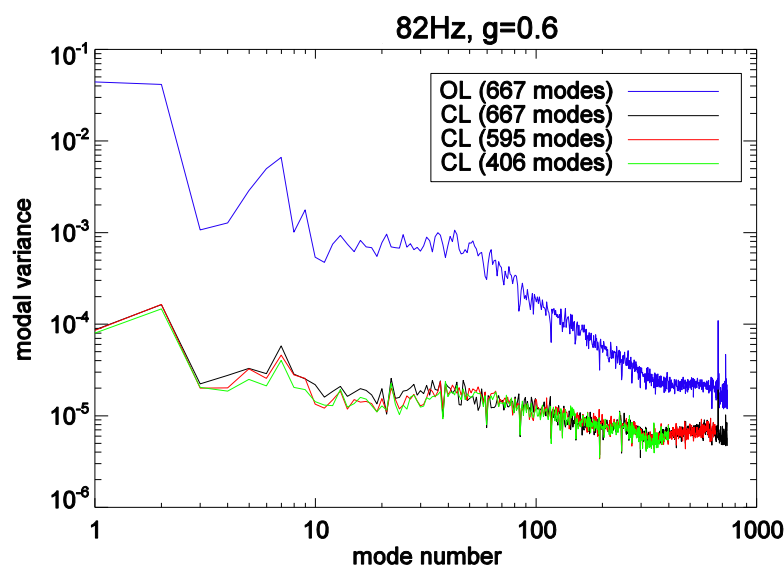


Figure 34. Modal variances obtained when controlling a different number of modes (High flux, 82Hz, $g=0.6$). The performance metrics are summarized in Table 3, and the commands' saturation analysis is shown in Figure 35.



HIGH ORDER TESTBENCH
SHS and PWFS comparison test report

Doc:
Issue: 1.0
Date: 18/05/09
Page: 49 out of 80

Number of modes	Gain (g)	Signal rms	residual variance
667	0.8	0.0693	0.00433
667	0.6	0.0778	0.00599
595	0.6	0.0776	0.00655
406	0.8	0.0830	0.00772
406	0.6	0.0901	0.00904

Table 3. Performance metrics as a function of the number of corrected modes (High flux, 82Hz, $g=\{0.6,0.8\}$). The actuator's configuration used was shown in Figure 30. The best performance is shown in shade. The modal variances of some cases are reported in Figure 34.

We should say that changing the master-slave configuration may solve these problems. In particular, note that those actuators at the upper pupil border that suffer saturation should actually be slaved down (Figure 30). As a future improvement, a new modal basis should be created with an updated master-slave mapping.

7.7.4 Estimation of Rejection Transfer Functions

The modulus of the turbulence rejection transfer function (RTF) of the j^{th} mode, denoted as $RTF_j(\omega)$, can be estimated as:

$$RTF_j(\omega) = \sqrt{\frac{PSD_{CL,j}(f)}{PSD_{OL,j}(f)}} \quad (10)$$

where $PSD_{CL,j}(f)$ and $PSD_{OL,j}(f)$ denote respectively the closed-loop and the open-loop temporal power spectral density of the j^{th} mode. It is important to note that an RTF under-estimation error may occur if open-loop slopes exhibit some saturation. This was actually the case in some data streams collected, as shown in Figure 36. Therefore, some under-estimation of the RTFs is expected.

When the integrator's gain (g) is the same for all the controlled modes, it is possible to estimate an *average RTF* for the BMM —denoted as $RTF_{DM}(f)$ — and for the TT mount of the MACAO —denoted as $RTF_{TT}(f)$ — simply as:

$$RTF_{DM}(f) = \langle RTF_j(f) \rangle \quad j \neq \text{tip, tilt} \quad (11)$$

$$RTF_{TT}(f) = \langle RTF_j(f) \rangle \quad j = \text{tip, tilt} \quad (12)$$

where $\langle \cdot \rangle$ denotes an ensemble average.



HIGH ORDER TESTBENCH

SHS and PWFS comparison test report

Doc:
Issue: 1.0
Date: 18/05/09
Page: 50 out of 80

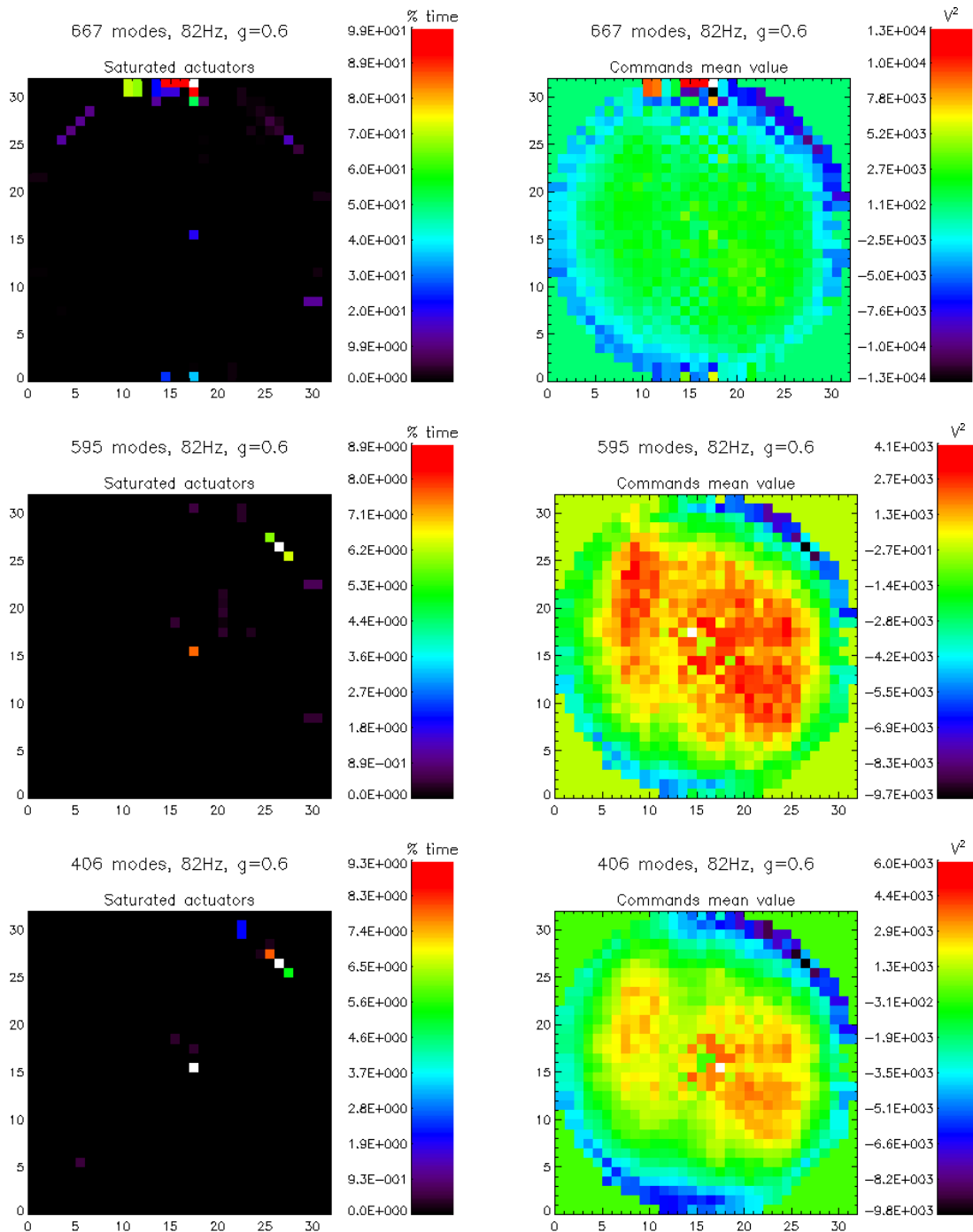


Figure 35. Analysis of commands saturation for different number of modes. (Left) Percent of the time during closed-loop operation that each actuator command was saturated. The commands range was set to $\pm 114^2 = \pm 1.3 \times 10^4 V^2$. (Right) Mean value of each command signal (in V^2 about the bias position) during closed-loop operation.

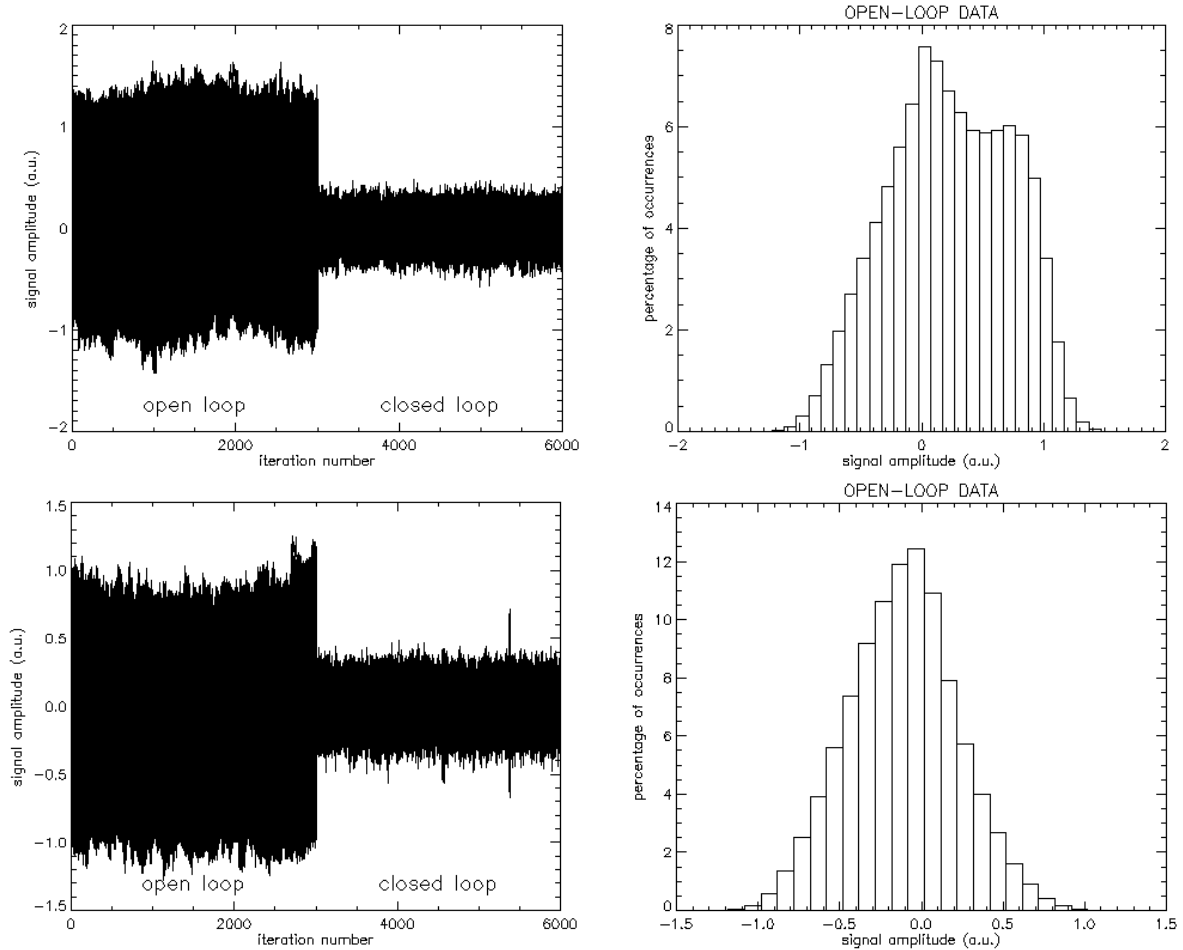


Figure 36. (Left) Overplot of all pyramid-sensor signals collected in two different data streams. The loops were closed from iteration number 3000. Note that the signals present some saturation during the open-loop operation (signal amplitude > 1). (Right) Open-loop signal's amplitude histogram. Note the stronger signal saturation in the data set shown in the first row (related to the particular position of the phase screens).

Since tip and tilt modes evolve slower than higher-order modes, a proper estimation of the TTM RTF would require a considerable large number of samples to estimate the required temporal spectra. Hence, we have decided to evaluate the temporal characteristics of the correction (bandwidth, overshoot, etc) by analysing only the BMM RTF. We will study in the following section the characteristics of the temporal correction as a function of the integrator's gain.



7.7.5 Effect of the integrator's gain

We will present in this section some experimental results that illustrate the impact of the integrator's gain (g) on the system performance. As it is well known, the correction bandwidth (BW) increases with the gain of the integrator controller. On the other hand, the band pass of the noise transfer function (NTF) also increases with the gain. Therefore, for a given flux level, it is possible to find an optimal gain that minimizes the residual phase variance by finding a compromise between turbulence rejection and noise propagation.

Figure 37 shows the modal variances and the BMM RTFs obtained with different gain values, and the performance metrics —signal rms, total residual variance, and correction bandwidth (BW)— are summarized in Table 4. Two sampling frequencies were investigated: 65 and 82 Hz. The flux level was set to the maximum. A slightly higher flux was obtained at 65Hz since the integration time was longer. The number of modes was fixed to 561.

Let us first comment on the BMM RTFs characteristics illustrated in Figure 37. Note that, as expected, the correction bandwidth increases with the gain and that, beyond the BW, the RTF exhibits an overshoot that also raises in amplitude with the gain. Since in this experiment the flux level is high (and therefore the propagated noise is low) increasing the gain effectively reduces the total residual variance and the signal rms, as reported in Table 4. Firstly, note that a better performance is obtained at 82Hz with respect to the 65Hz in all cases. For the case of 82Hz, the maximum gain considered ($g=1.4$) actually gives the best performance. On the other hand, for the case of 65Hz, a gain of $g=1.2$ already deteriorates it. In particular, notice the worsening of the correction for the high-order modes as the gain increases in the 65Hz-case. This behaviour could be related to an instability problem. Indeed, at lower sampling frequencies the pure time delay becomes more significant and the maximum allowed gain becomes limited due to stability constraints.



HIGH ORDER TESTBENCH

SHS and PWFS comparison test report

Doc:
 Issue: 1.0
 Date: 18/05/09
 Page: 53 out of 80

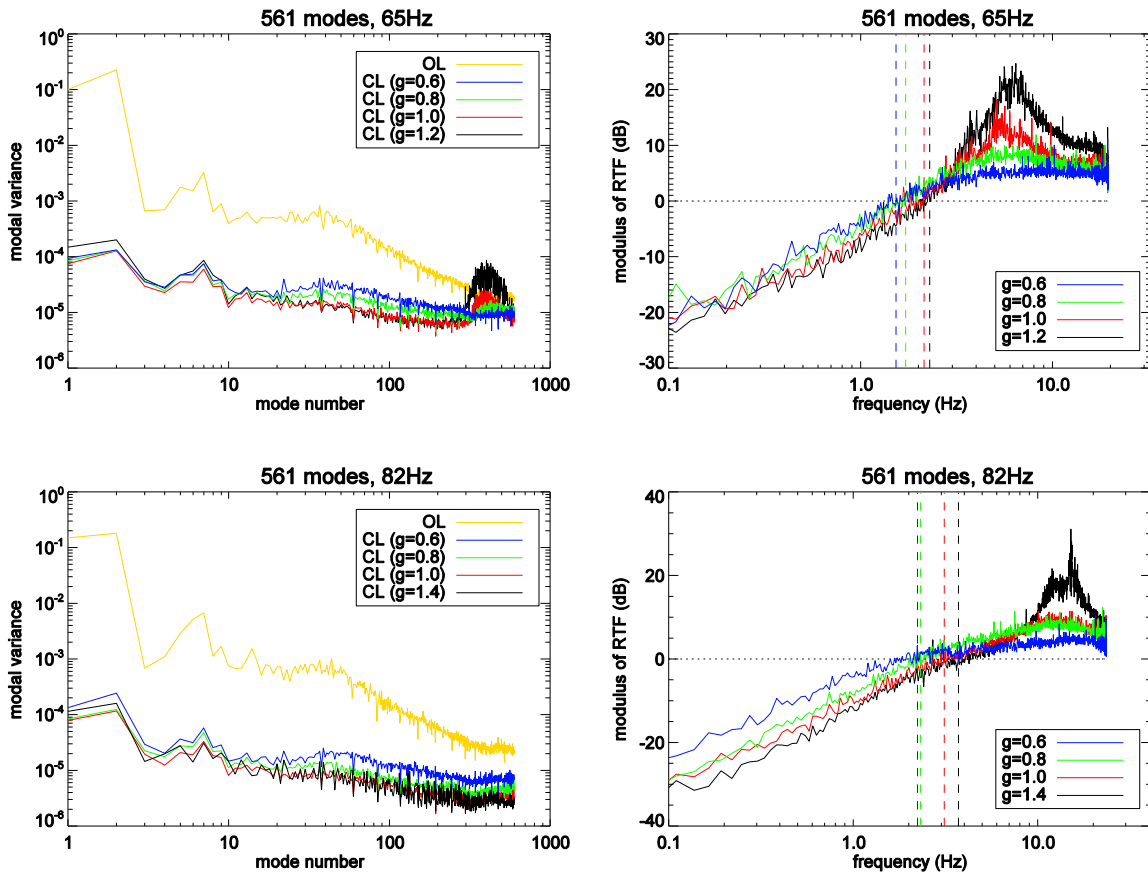



Figure 37. Effect of the integrator's gain on the modal variances (*Left*), and on the BMM's rejection transfer functions (*Right*). The corresponding correction bandwidths are also indicated on the RTF plots. The performance metrics are summarized in Table 4.

65 Hz				82 Hz			
Gain (g)	Signal rms	residual variance	BW (Hz)	Gain (g)	Signal rms	residual variance	BW (Hz)
0.6	0.0920	0.00794	1.53	0.6	0.0807	0.00552	2.23
0.8	0.0893	0.00701	1.72	0.8	0.0717	0.00359	2.32
1.0	0.0849	0.00626	2.14	1.0	0.0657	0.00258	3.11
1.2	0.0973	0.01125	2.29	1.4	0.0621	0.00256	3.72

Table 4. Performance metrics as a function of the gain (g) for the data sets presented in Figure 37.

	HIGH ORDER TESTBENCH SHS and PWFS comparison test report	Doc: Issue: 1.0 Date: 18/05/09 Page: 54 out of 80
---	--	--

8 SHWFS and PWFS experiment comparison

8.1 *Experimental plan.*

Same conditions are required for the measurements to be able to compare the two types of wavefront sensors present on the HOT bench.

To assure this requirement we proceeded with an experimental plan consisting in doing simultaneous measurements with both sensors for each flux conditions. A flat mirror installed on a magnetic mount allowed us to switch easily between both sensors for each set of measurements. Thus, same experimental conditions (flux on the ITC, noise, setup stability) could be assured.

The second point to take into account is to fix the same control parameters for both sensors: sampling frequency and control bandwidth, L3 gain, etc.

Three star magnitude cases were studied. For each case we studied the SR, PSF profile and modal performance. Using the ITC two types of images were recorded. A non saturated PSF image (long exposure) and a saturated PSF image (short exposure). The first one gives the SR and PSF profile information. The second one is foreseen to study, with better SNR, the external rings of the PSF.

For each star magnitude case, and for both sensors, the experimental steps were the following:

- Check the flux detected by the sensor (without L3gain active) and adjust to the star magnitude case desired.
- Find the maximal L3gain value to apply to the CCD avoiding saturation.
- CCD background acquisition.
- Adjust density wheel position to maximize signal on the ITC. Once a position is chosen, it is kept fixed for all tests done at the same flux level.
- Closed-loop gain optimization.
- Closed the loop: record long exposure PSF image.
 - For the SHS: with and without SF.
- Record dark image (long exposure time).
- Closed the loop: record short exposure (saturated) PSF.
- Record dark image (short exposure time).

8.2 *Initial conditions.*

8.2.1 Turbulence and illumination conditions.

The 0.5" seeing phase screens were used for the experiments. As explained on section 5.2, the phase screens were set at minimum speed and turning in opposite directions (same turbulence direction). Thus, the equivalent turbulence speed for an 8-m telescope is 1.3 m/s. The HOT bench minimize the effect of internal turbulence since it is completely covered. Furthermore, the external photon contamination is also minimized.



HIGH ORDER TESTBENCH
SHS and PWFS comparison test report

Doc:
Issue: 1.0
Date: 18/05/09
Page: 55 out of 80

Regarding the illumination conditions, we decided to compare the performance of the two wavefront sensors under three different flux levels. As an initial goal, we wanted to do this comparison down to an equivalent star magnitude of 11. However, this was not possible to achieve during these experiments due to an unstable operation of the illumination lamp at low flux levels. We should note that, as a follow-up of the HOT experiment, neutral density filters could be used to reach lower illumination conditions. Table 5 shows the three flux levels considered in the comparison: maximum flux (case A), intermediate flux (case B), and lowest stable flux achieved with the illumination lamp (case C). The total number of photons per frame was measured (without L3gain active) on both wavefront sensors to make sure that similar conditions were achieved.

	SHS		PWS	
CASE	ph/frame	ph/frame/subap	ph/frame	ph/frame/subap
A	1.36E+07	1.9E+04	1.1E+07	1.49E+04
B	4.0E+05	5.6E+02	6.5E+05	8.95E+02
C	1.0E+05	1.5E+02	1.5E+05	2.14E+02

Table 5. Flux levels measured on the SHS and the PWS for each of the three study cases. The total number of subapertures considered was 718 and 730 for the SHS and the PWS respectively (CCD frequency set at 75 Hz).

Let us now estimate the equivalent star magnitudes for the three study cases. In order to do this, we need to assume a realistic sampling frequency of an XAO system. For instance, in the case of SPHERE, a sampling frequency of 1.2kHz is foreseen. Hence, let us consider that the number of photons per frame (reported in Table 5) correspond to an XAO system running at 1.2kHz. Table 6 shows the equivalent star magnitude corresponding to each of the three study cases taking into account this sampling frequency, an 8-m diameter telescope, a 0.2 transmission coefficient for the optics, a bandwidth of $\Delta\lambda=0.25\mu\text{m}$ centred at $\lambda_c=0.64\mu\text{m}$, and a zero-magnitude flux of $\phi_0=1.76\times 10^{-8} \text{ W m}^{-2} \mu\text{m}^{-1}$.

CASE	equivalent star magnitude
A	~2.4
B	~5.9
C	~7.5

Table 6. Equivalent star magnitude for the three study cases. Parameters: sampling frequency 1.2kHz, 8-m telescope, optical transmission 0.2, bandwidth of $\Delta\lambda=0.25\mu\text{m}$ centered at $\lambda_c=0.64\mu\text{m}$, a zero-magnitude flux of $\phi_0=1.76\times 10^{-8} \text{ W m}^{-2} \mu\text{m}^{-1}$.

8.2.2 L3 gain and equivalent RON

The ANDOR CCD cameras were set to the optimal conditions following the recommendations of AD12. The preamplifier gain was set to value 1 (nominally corresponds



to approximately x2) corresponding to a system sensitivity of 32.5 e/ADU (absence of L3 gain).

It is possible to change the amplitude of the clock voltages thereby amplifying the signal. Gain index values between 0 and 4096 are permitted, but it is not recommended to use gains over 3500. Figure 38 shows the system sensitivity as a function of the L3 gain index.

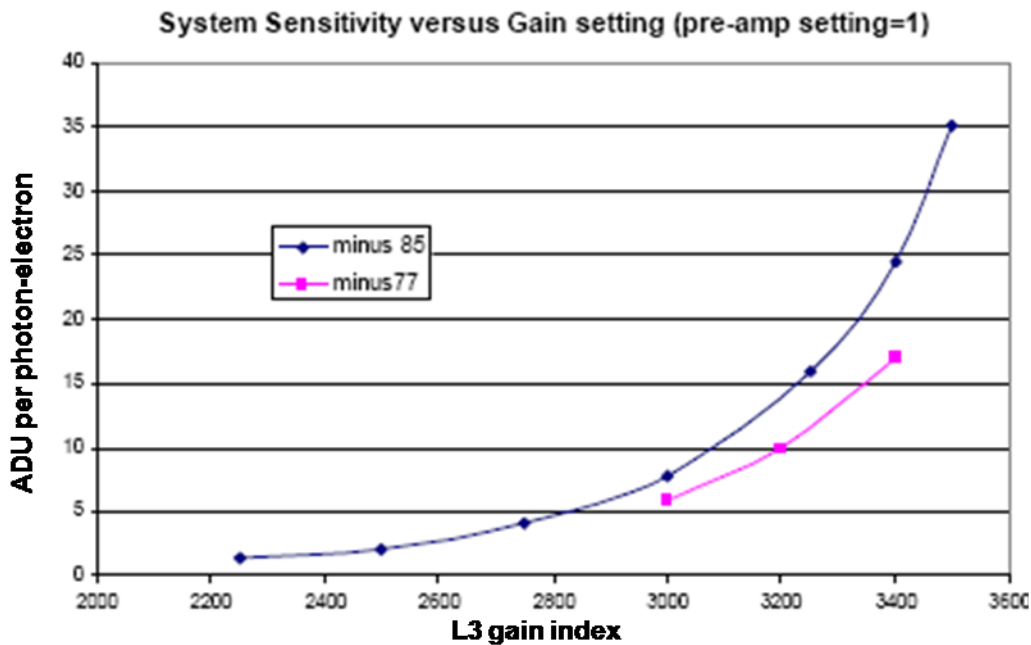


Figure 38. Curve showing the sensitivity behavior in function of the L3 gain index for cooling temperatures of minus 85 and minus 77 (Taken from AD12).

The L3 gain index was selected independently for each sensor in order to maximize the signal while avoiding saturation. The maximum value used is around ~9000 ADU, since the signal starts to go non-linear at 10,000 ADU (clipped at 16383 by the ADC range).

Table 7 shows the L3 gain index used for the different experimental cases. The equivalent sensitivity for a cooling temperature of -85 degrees was extracted from the curve in Figure 38, so it has to be considered as approximate values. Furthermore, the camera's temperature was cooled to -82 degrees for the SHS case and -77 degrees for the PWS, so a change of about 4% in gain per °C needs to be considered.

	SHS		PWS	
	L3 gain index	sensitivity (ADU/e)	L3 gain index	sensitivity (ADU/e)
star A	1950	~0.3	140	~1



HIGH ORDER TESTBENCH
SHS and PWFS comparison test report

Doc:
Issue: 1.0
Date: 18/05/09
Page: 57 out of 80

star B	3270	17-18	225	>40
star C	3500	35	220	35

Table 7. L3 gain values applied to the SHS and PWS CCD for the three flux cases. The sensitivity is obtained from the -85 degrees curve on Figure 38.

The intrinsic noise of the camera is very high; up to 200e RMS. With the L3 gain turned up high, this became insignificant (0.07 e⁻ RMS at 3500 index). The values for the different gain conditions can be extracted from Figure 39.

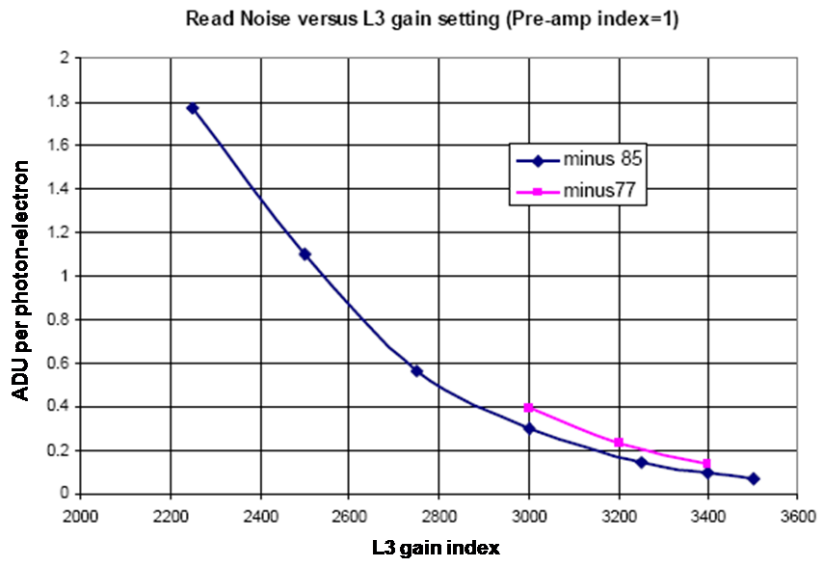


Figure 39. CCD Read out noise as function of the L3 gain index (Taken from AD12).

8.2.3 Reconstructor

The performance comparison was done using a reconstructor with the same number of modes for SHS and PWS. Thus, a modal reconstructor of ~400 modes was selected since the loop was stable for both sensors (413, SHS and 435, PWS). For the SHS the measurements were done using this reconstructor both without SF and with SF (1.8 λ/d) (As explained on section 6.4.3, a reconstructor obtained using an IM acquired through the SF performed worst).

In the case of the PWS another set of measurements were done using a reconstructor of 561 modes because the sensor was able to close the loop with a higher number of modes (not for the SHS since saturation on the BMM was detected if more modes were used).

8.2.4 Loop frequency and bandwidth.

The frequency loop was set to 65 Hz for both sensors. This was the maximum speed the SHS could run due to the RTC computing limitations on MATLAB (the PWS could run around 100 Hz). At this speed the control bandwidth of the loop for the SHS and PWS is

around 1.7 – 2.3 Hz. Thus, similar bandwidths are assured for a reasonable comparison. More details on the bandwidth characterisation can be found in sections 7.7.5 and 8.4.1.2.

8.2.5 ITC: PSF image acquisition.

For each experimental case two PSF images were acquired: non saturated and saturated. The non saturated image is used for SR estimation and profile study. The ITC linear range is up to ~10000 counts; hence, the density wheel was adjusted to have a high signal on the CCD below this limit. It is important to maintain this wheel position for the PSF acquisition for both sensors to obtain a relative comparison between profiles. A long exposure time around 15 min was required to obtain a good SNR. This long exposure time was obtained by recording a sequence of short-exposure images of around 2 sec. The exact integration times and ITC signal's peak values are reported in Table 8.

A second PSF was obtained by saturating the center of the PSF in order to have more signal on the halo and external rings. These images will allow us to study the behaviour at high order spatial frequencies. The density wheel was adjusted in order to have the maximum signal (under 10000 counts) on the first ring. In this case the integration time could be shorter, around 6 minutes.

The exposure times were also selected taking into account the fact that a high number of PSFs were needed to be recorded and the experimental time was limited.

		Exposure time	DIT integration time	ITC peak flux
star A	non Saturated	15 min 53 sec	2.5 sec	8135
	Saturated	6 min 21 sec	2.5 sec	8000
star B	non Saturated	15 min 53 sec	2.5 sec	8760
	Saturated	6 min 19 sec	5 sec	9000
star C	non Saturated	15 min 53 sec	2.5 sec	9700
	Saturated	6 min 36 sec	10 sec	4000

Table 8. Summarize table of integration times used for the different acquisition cases. The last column shows the peak intensity of the PSF. In the saturated case, the intensity value is measured on the first ring.

In the case using SF, for stars B and C, the image acquisition (non saturated) was aborted after around 9 min because the loop started to diverge. Since the loop was not stable for these cases we decided not to record the saturated images to save time.

In any case, the aborted images were analysed a-posteriori and included in this report since the PSFs presented a good quality.



8.3 PSF analysis

8.3.1 The ghosts problem

The analysis of the PSF images is hindered by the presence of several ghosts. Figure 40 shows the ghost distribution. Ghosts 1, 2 and 3 come from the BMM protective window; 1 from the external reflection and 2-3 from internal reflections. Ghosts 4, 5 and 6 are caused by the density wheel and are associated with a replication of the PSF and ghosts 1-2. In addition, another small ghost (7) appears quite near to the PSF, probably caused by the narrow H band filter or the ITC entrance window.

Ghosts 1 and 2 are the most intense and limit the study area of the PSF. The distance between the center of the PSF and ghosts is around 1.3 arcsec ($\sim 30 \lambda/D$). Figure 40(Right) shows the area of influence of the ghosts (cut levels 97 %).

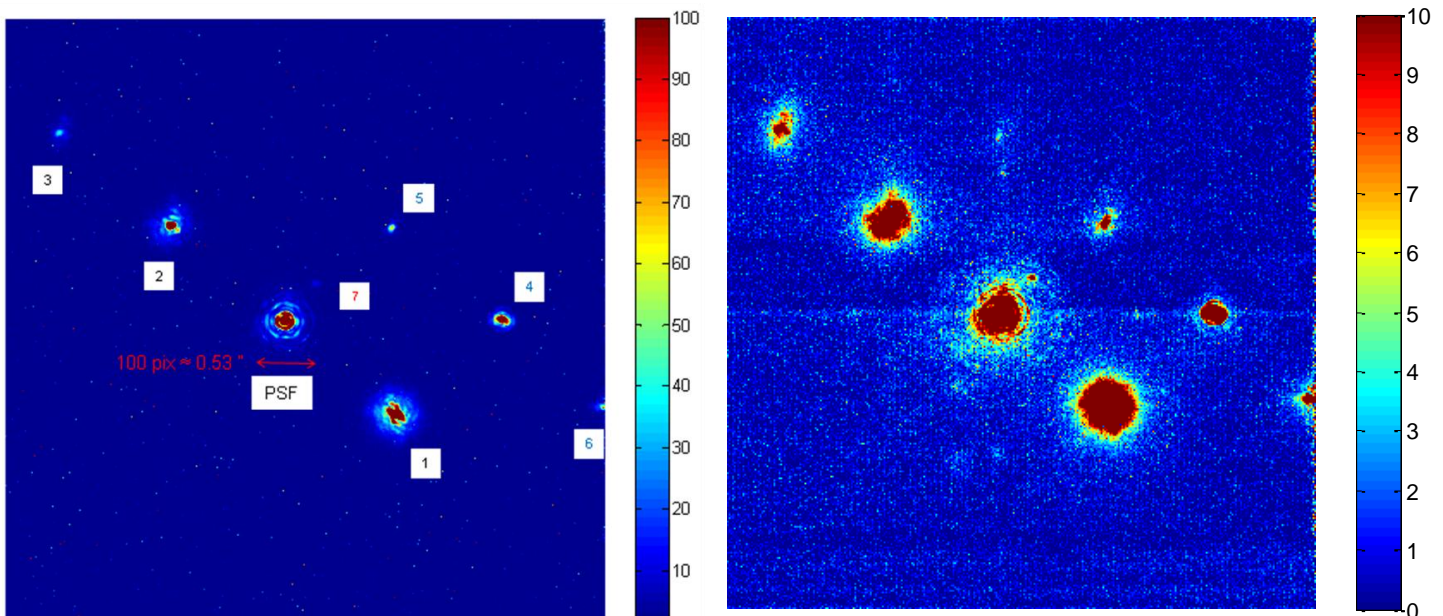



Figure 40. ITC image showing the position of the ghosts (left) and the affected area (right). The size of the full image frame is 1024x1024 pixels.

8.3.2 PSF profile and pixel scale estimation

A standard image processing is applied to the raw PSF image consisting on dark subtraction, sky subtraction and spike filtering ($\sigma_{\text{sky}} \approx 3.2$ counts).

The PSF profile is computed as an azimuthally-averaged profile covering 0.9 arcsec.

The pixel scale was estimated measuring the position of the 3rd minimum (dark ring) on the PSF profile: 25 pixels. For a circular pupil with 14% central obstruction ratio this minimum corresponds to a distance of 3.142 λ/D . Thus, the pixel scale obtained is 5.314 mas/pix ($\lambda=1640$ nm).

	HIGH ORDER TESTBENCH SHS and PWFS comparison test report	Doc: Issue: 1.0 Date: 18/05/09 Page: 60 out of 80
---	--	--

8.3.3 SR estimation

Two different routines were used for the Strehl ratio estimation. The method 1 runs under matlab and was used before on NACO. The method 2 is used for MAD and runs under IDL. Although both algorithms are based on the same principle, some difference on SR were found.

The method 1 computes the SR as the ratio between the peak intensities of the measured PSF (normalized to the total flux) and the theoretical PSF. The theoretical PSF is computed by applying the Fourier transform to a circular pupil with 14% central obstruction ratio and taking into account the pixel scale. The theoretical PSF profile are plotted with the experimental ones on section 8.5.

The method 2 is similar, the main difference consists in how the theoretical PSF is computed; in this case an analytical method is used (the PSF is computed from the 2D analytical PSF formula). The second difference is how the sky signal is computed. The method 1 analyses all the image to compute the sky signal, while the second method computes it on 4 small squares placed at the corners of a square sub-inscribing the PSF. The SR estimation is quite sensible to the pixel scale: errors of 0.1 mas produce changes on the SR of around 3%. On the other hand, the variation of the radius of the integrated flux produced small variations (in a radius region we are sure quite all the energy is computed) of around 1% using the method 2 and higher on the method 1, around 3%. In this case the presence of small ghosts (like the number 7, on Figure 40) could produce these variations. Thus, a 5% could be a good estimation of the SR global error.

8.4 Close loop optimization

8.4.1 SHS loop optimization

8.4.1.1 SHS gain optimization

The gain of the loop was optimized for the conditions of the comparison between SHS and PWS: Loop at 65 Hz and 413 modes reconstructor. In the case of the SHS the optimization was done studying the PSF performance. For each flux case a set of short PSFs (~ 3 min) were acquire with different gains. The optimal gain is chosen taking into account the maximum peak, SR and PSF profile. The PSFs for the gain optimization were acquired just before the definitive ones.

The SR and peak for the three flux cases are shown in Table 9 and plotted on Figure 41 showing the SR performance as a function of the loop gain. The PSF profiles for all the measurements can be found in the annexe.

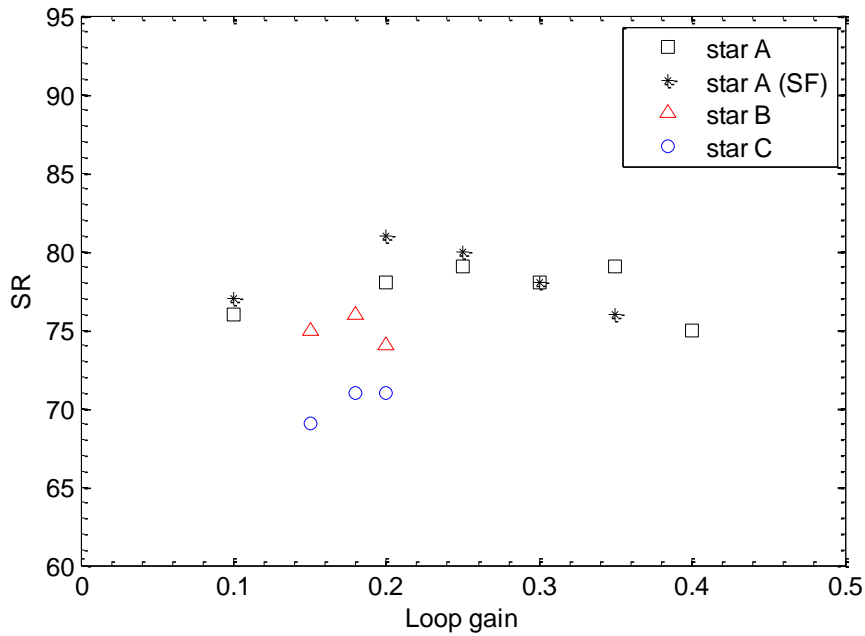


Figure 41. Plot of SR measured for different loop gain values. On black star A (high flux case, square: no SF, asterisk: SF), red triangles for star B and blue circles for star C.

STAR A		
LOOP GAIN	SR	Peak
0.1	76	11156
0.2	78	11522
0.25	79	11572
0.3	78	11483
0.35	79	11612
0.4	75	10587
0.6	24	4405

STAR A (SF)		
LOOP GAIN	SR	Peak
0.1	77	11176
0.2	81	11675
0.25	80	11528
0.3	78	11228
0.35	76	11026
0.4	27	3055
0.6	23	6885

STAR B		
LOOP GAIN	SR	Peak
0.15	75	6260
0.18	76	6346
0.2	74	6273

STAR C		
LOOP GAIN	SR	Peak
0.15	69	7139
0.18	71	7302
0.2	71	7258

Table 9. Summary of results for the loop gain optimization. SR and max peak are shown for different gain values on the three star magnitudes cases.



The working range found for high flux conditions is between 0.1 and 0.35. The optimal value is 0.25. For star B and C, we measured only between 0.15 and 0.2 to find the optimal value. For both cases the optimal value is 0.18.

The gain values chosen for the three stars on the experiments were: 0.2, 0.2 and 0.18. These results are slightly different from the optimal ones shown because at the moment of the experiments the tools for the PSF analysis were not exactly the same. Furthermore, we also took into account the PSF profiles.

The optimization for the SF case was done only for the high flux case. The optimal value was 0.2, but it was not possible to keep the loop stable in the case of a long exposure time (15 min). So, it was necessary to reduce the gain to 0.17 to obtain a stable loop. On the other star cases the loop was not stable for more than 9 min even reducing the gain (until 0.15 gain was checked). This is the reason why there was no interest to proceed with the gain study for these cases.

8.4.1.2 SHS Transfer Function

Once the gain loop parameter was selected for each studied case (flux, without/with SF), the RTF and loop bandwidth were measured.

The average RTF of the turbulence were computed as explained in section 7.7.4, since the gain is the same for all the 413 controlled modes.

The RTF was calculated taking series of ~5000 frames measured on OL and CL at a frequency loop of 65 Hz. The modal coefficients for each frame are computed from the slopes using the IM and the modal basis.

The RTFs are shown in Figure 42 and the corresponding bandwidth values are reported in Table 10.

	no SF		SF	
	gain	bandwidth	gain	bandwidth
star A	0.2	1.8	0.17	1.8
star B	0.2	1.8	0.15	2
star C	0.18	1.6	0.16	1.7

Table 10. Loop bandwidth results (Hz).

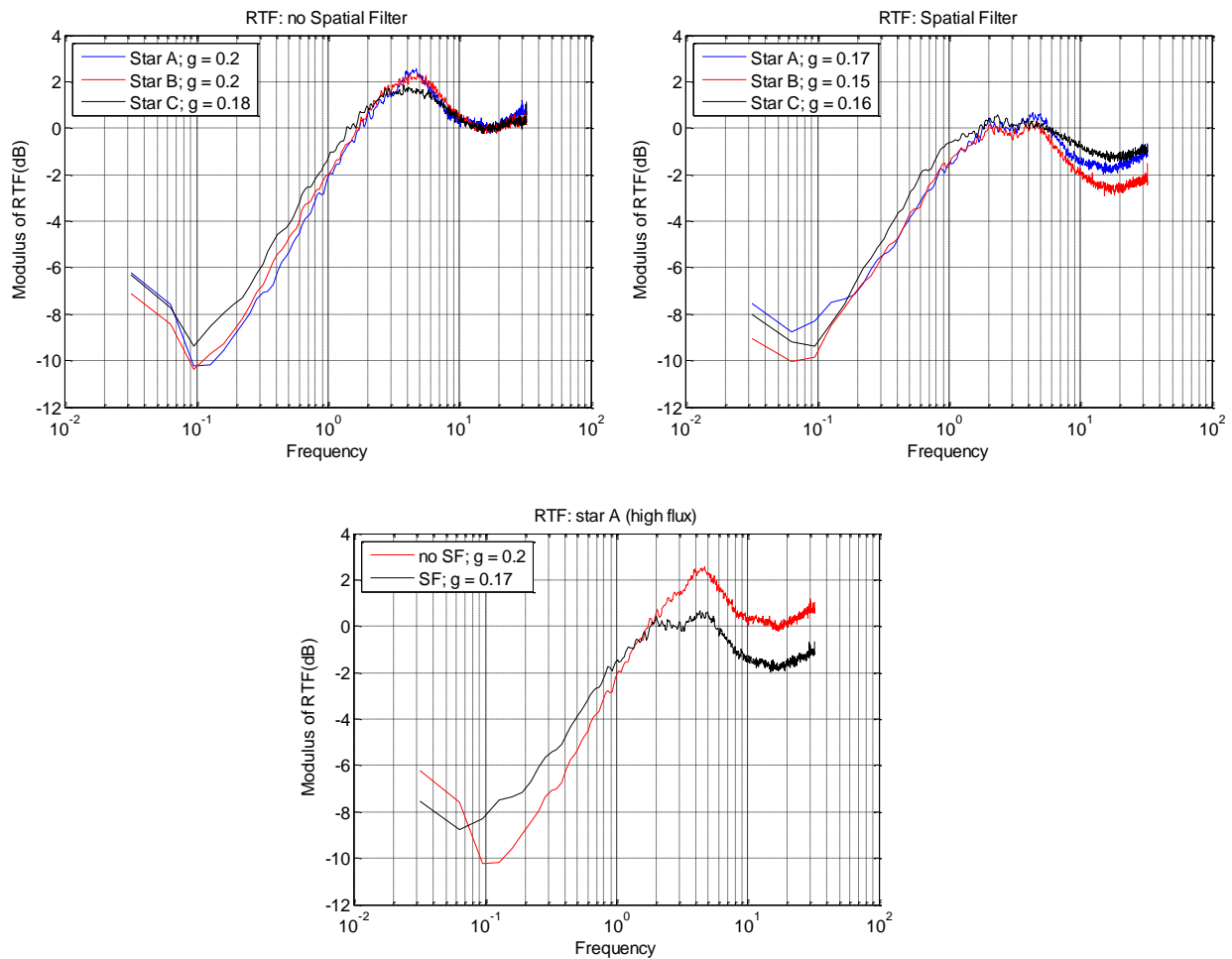


Figure 42. Plots showing the loop temporal behaviour. (a) up-left: RTF curves for the case without SF (three star magnitude). (b): RTF curves for the case with SF (three star magnitude). (c): RTF curves for the high flux conditions comparing the case with and without SF.

8.4.1.3 Modal correction versus magnitude.

The modal decomposition of the turbulence (open loop, Figure 43(a, b)), shows clearly the turbulence profile of the phase screens (Figure 3) plus an internal component coming from the bench.

Open loop curves show how the modal variance increase, for high order modes, when the flux decrease, caused by photon noise.

Figure 43(c,d) show the modal performance in closed loop for the three flux cases. As expected, reducing the flux the correction decreases. On the spatial filter case (Figure 43(d)), the second flux case gives a modal performance closer to the higher flux case. These values are too high comparing with the other flux cases. It took probably its origin in an error along the slopes acquisition.



Figure 44 compares the cases with and without spatial filter. It is clear that no increase in the performance is achieved with the use of the SF.

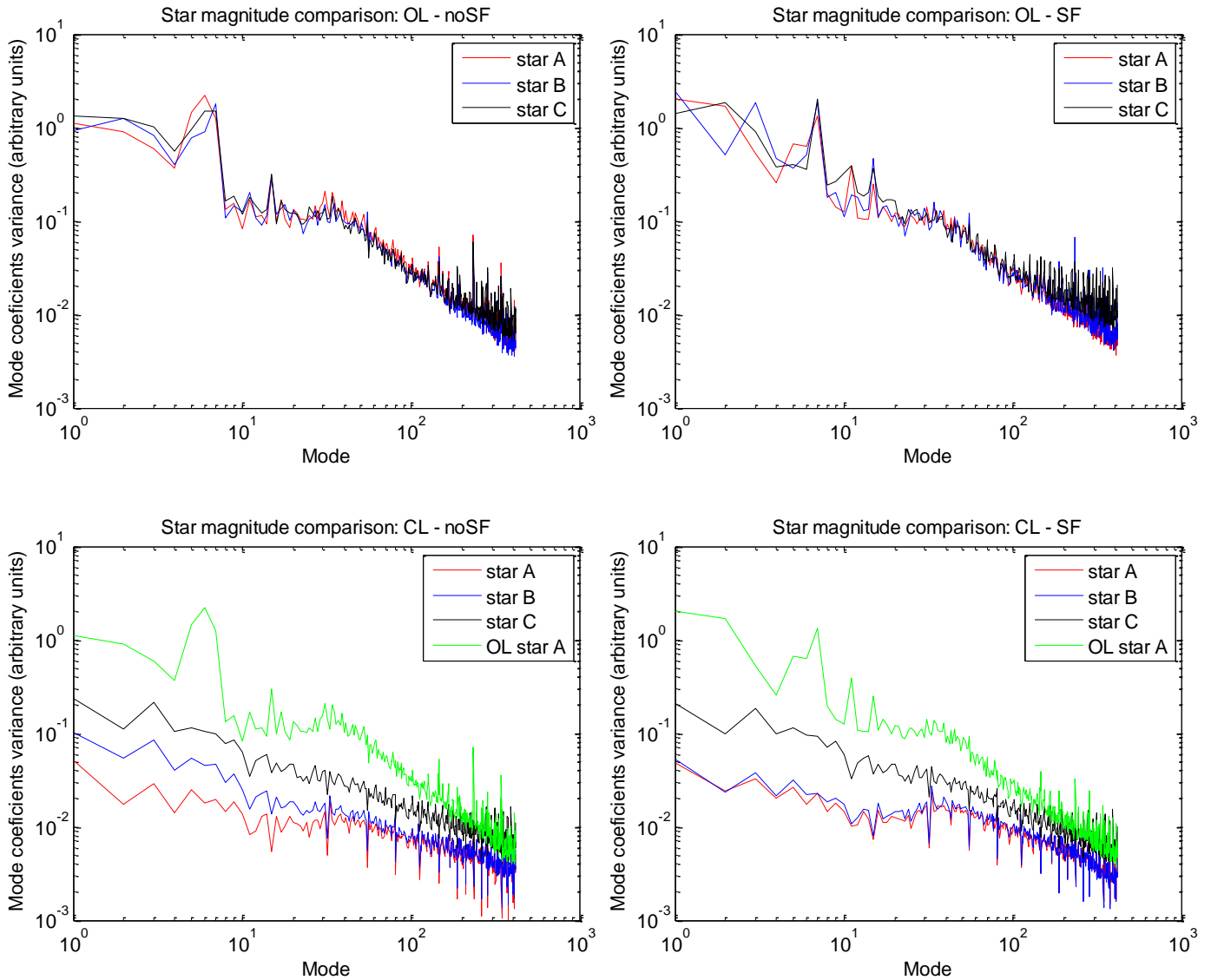


Figure 43. Modal decomposition for the three flux conditions using the 413 modal reconstructor. (a) up-left: open loop without SF. (b) up-right: open loop with SF. (c) down-left: close loop without SF (d) down-right: close loop with SF.

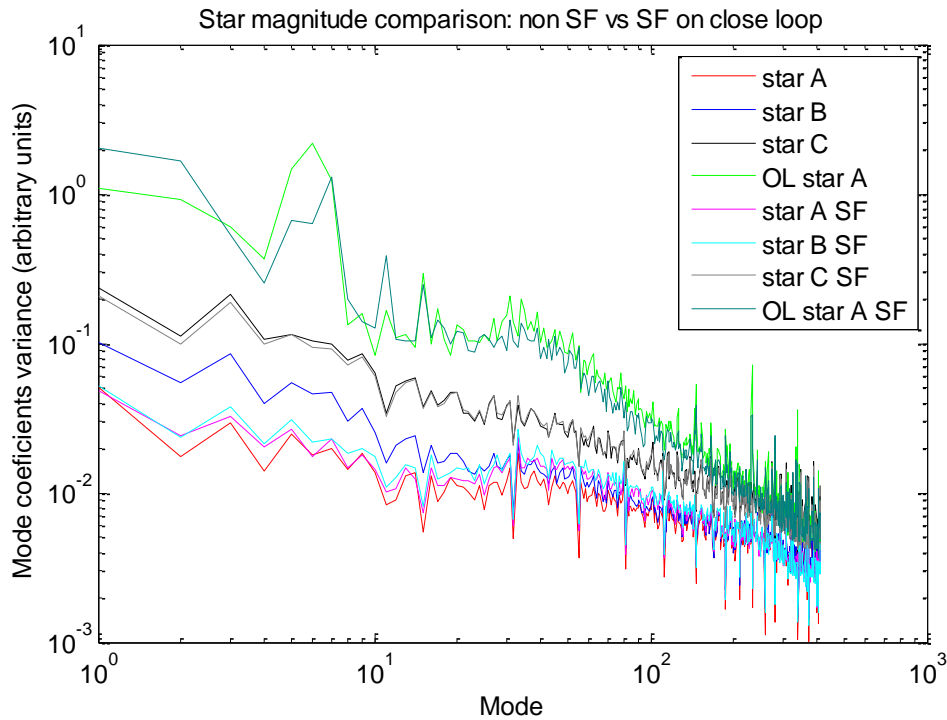


Figure 44. Modal decomposition for the three flux conditions using the 413 modal reconstructor comparing the cases with and without SF.

8.4.2 PWS loop optimization

In these experiments the sampling frequency was set to 65 Hz in order to match the maximum correction bandwidth achieved by the SH sensor ($BW \approx 2\text{Hz}$). The shape of the RTFs obtained with the PWFS were presented in section 7.7.5.

For each of the three flux levels studied, we investigated the control parameters (number of controlled modes, integrator gain) that minimized the slope rms and residual modal variance. We should note that the maximum number of modes that we considered was 561. This was to prevent the actuator's saturation effects we encounter with the chosen modal basis when controlling more than 600 modes (section 7.7.3).

Regarding the computation of the residual variance (equation 9), the maximum number of modes taken into account in the computation of the 'fitting-error' term was $m=561$. Furthermore, this term was computed using the open-loop data taken at the highest flux level, since at lower magnitudes the open-loop variances for the highest modes become dominated by propagated measurement noise, and this would lead to an incorrect fitting-error term estimation.


	HIGH ORDER TESTBENCH SHS and PWFS comparison test report	Doc: Issue: 1.0 Date: Page: 66 out of 80
---	--	---

Table 11 and Figure 45 summarize the performance metrics obtained for each set of parameters explored. Note that the best performance for the stars A and B is obtained with 561 controlled modes and $g=0.8$. On the other hand, note that for star C the number of controlled modes that minimize the slope rms and the residual variance is not the same (561 and 300 modes respectively). Further insight can be found in Figure 46(Left), in which the modal variances for the three flux levels are displayed. Note that for the lowest flux level, modes higher than ≈ 300 modes are dominated by propagated measurement noise. Therefore, it seems reasonable to cut down the number of controlled modes in order to improve the performance. In comparison, note that for star B, modal variances of higher modes are also visibly affected by propagated measurement noise (the modal variances monotonically increase after mode number ≈ 300); however, the residual modal variances are still lower than the open-loop (turbulence) modal variances. Hence, it seems reasonable to control all 561 modes in this case. As a future improvement, a modal gain integrator could be implemented in order to optimize the correction for each mode by tuning the integrator's gain.

It is important to emphasize that the optimization study presented in this section is based on the analysis of the real-time slopes instead of the PSFs. In the following section we will present the analysis of the PSFs obtained with the parameters that minimized the signal rms (561 controlled modes and different gains). Also, in order to compare the results with the SH sensor, we acquired a set of PSFs controlling only 435 modes for each of the three star cases. For the star C, it would have been interesting to study the PSF obtained when controlling 300 modes (i.e. the set of parameters that minimize the residual modal variance). Unfortunately, we did not have the time to perform these experiments.



HIGH ORDER TESTBENCH
SHS and PWFS comparison test report

Doc:
Issue: 1.0
Date:
Page: 67 out of 80

CASE A				
Number of modes	Gain (g)	Signal rms	residual variance	BW (Hz)
561	0.8	0.06699	0.00517	2.44
435	0.8	0.07913	0.00731	2.70
CASE B				
Number of modes	Gain (g)	Signal rms	residual variance	BW (Hz)
561	0.8	0.09332	0.01019	2.41
561	0.6	0.09827	0.01202	1.75
435	0.8	0.09790	0.01102	2.30
435	0.6	0.10364	0.01278	1.74
300	0.8	0.10815	0.01307	2.29
300	0.6	0.11344	0.01469	1.76
CASE C				
Number of modes	Gain (g)	Signal rms	residual variance	BW (Hz)
561	0.6	0.17116	0.03586	1.91
561	0.4	0.17185	0.03653	1.30
435	0.6	0.17167	0.03042	2.13
435	0.4	0.17648	0.03338	1.44
300	0.6	0.17777	0.02863	2.01
300	0.4	0.18344	0.03182	1.45

Table 11. Summary of performance metrics obtained for each star magnitude, and for each set of parameters explored. The best performance metrics at each magnitude are shown in shade.

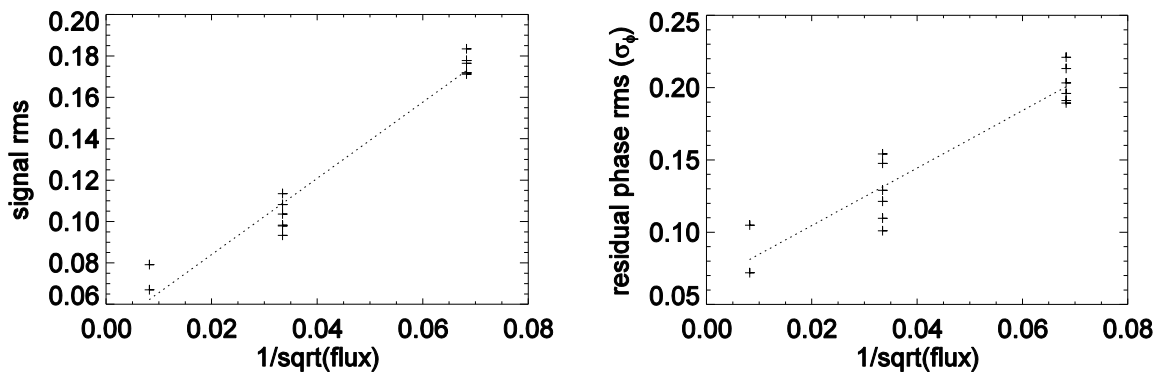


Figure 45. Summary plots showing the performance metrics obtained in all data sets as a function of the inverse square-root of the number of photons per subaperture per frame. The linear fit to the data is also shown. (Left) Signal rms. The linear fit coefficient is 1.84. (Right) Residual phase rms (σ_ϕ). The linear fit coefficient is 1.99.

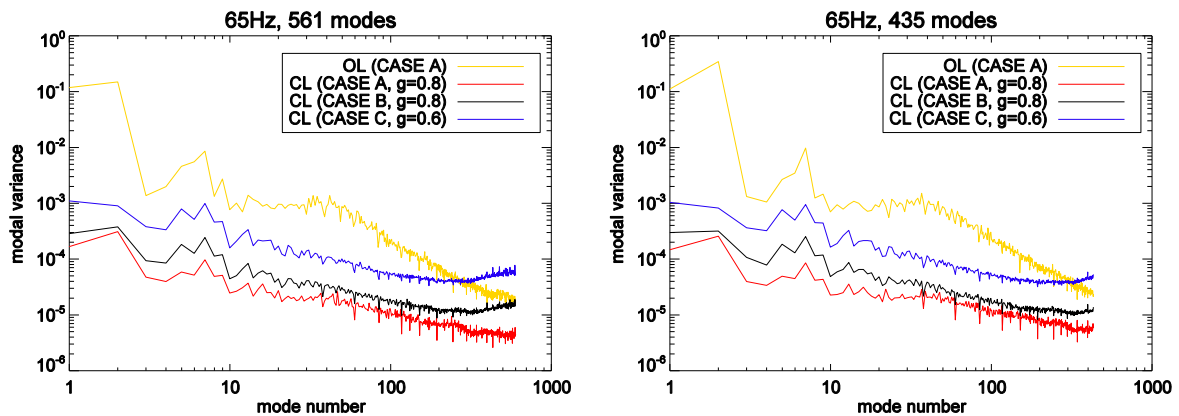


Figure 46. Modal variances for the three flux levels (CASE A, B, and C). (Left) When correcting 561 modes. (Right) When correcting 435 modes. The open-loop modal variances shown in the plot were estimated from the real-time data at the highest flux (CASE A).

8.5 PSF correction versus magnitude: Strehl ratio and FWHM

We will present in this section the comparison in performance between the SHS and the PWFS in terms of Strehl ratio (SR) and FWHM for the three flux levels (case A, B, and C) considered.

For the case A, two sets of PSF measurements were done. On the first try the PWS CCD was not cooled at the set point temperature, so the measurements were done again for both sensors (They will be referred as case A1 and case A2). Figure 47 shows the non-saturated PSFs acquired for both sensors at the three flux levels (best experimental PSFs; SHS with no SF and 413 modes, and PWFS with 435 modes). The SHS PSF images show a strange external ring of speckles whose origin is not clear.

The method to estimate the SR from the non-saturated PSFs was discussed in section 8.3.3. Table 12 reports the SR and FWHM estimates for all the PSFs analysed. First of all, note that some of the SR values reported in the table are higher than 100%. Of course, this is not physically possible. Taking into account the error of 5% in the SR estimation (section 8.3.3), these results should be simply interpreted as almost perfect correction.

For comparison, the SR and the FWHM of an uncorrected (open-loop) long-exposure PSF were also measured, resulting in a SR of 11% and a FWHM of 0.0686 arcsec. On the other hand, the FWHM of the PSF on the IR path alone (i.e. only residual static aberrations present) was also characterized, resulting in a FWHM of 0.0441 arcsec. Note that the FWHM of theoretical diffraction-limited PSF is 0.0425 arcsec.

In the case of the SHS, note from Table 12 that a slightly higher SR is obtained when no SF is used for cases A and B while for case C is the opposite. This result is not surprising taking into account the SF stability problems explained in section 6.4.3. In any case, the difference is ~3%, so once again taking into account the error of 5% in the SR estimation we could conclude that the performance is the same for both cases. In the case of the PWFS, it is interesting to note that no gain in SR is obtained when using 561 modes with respect to the 435-modes case. Taking into consideration the SR estimation error we could state that the performance with both number of controlled modes is the same.

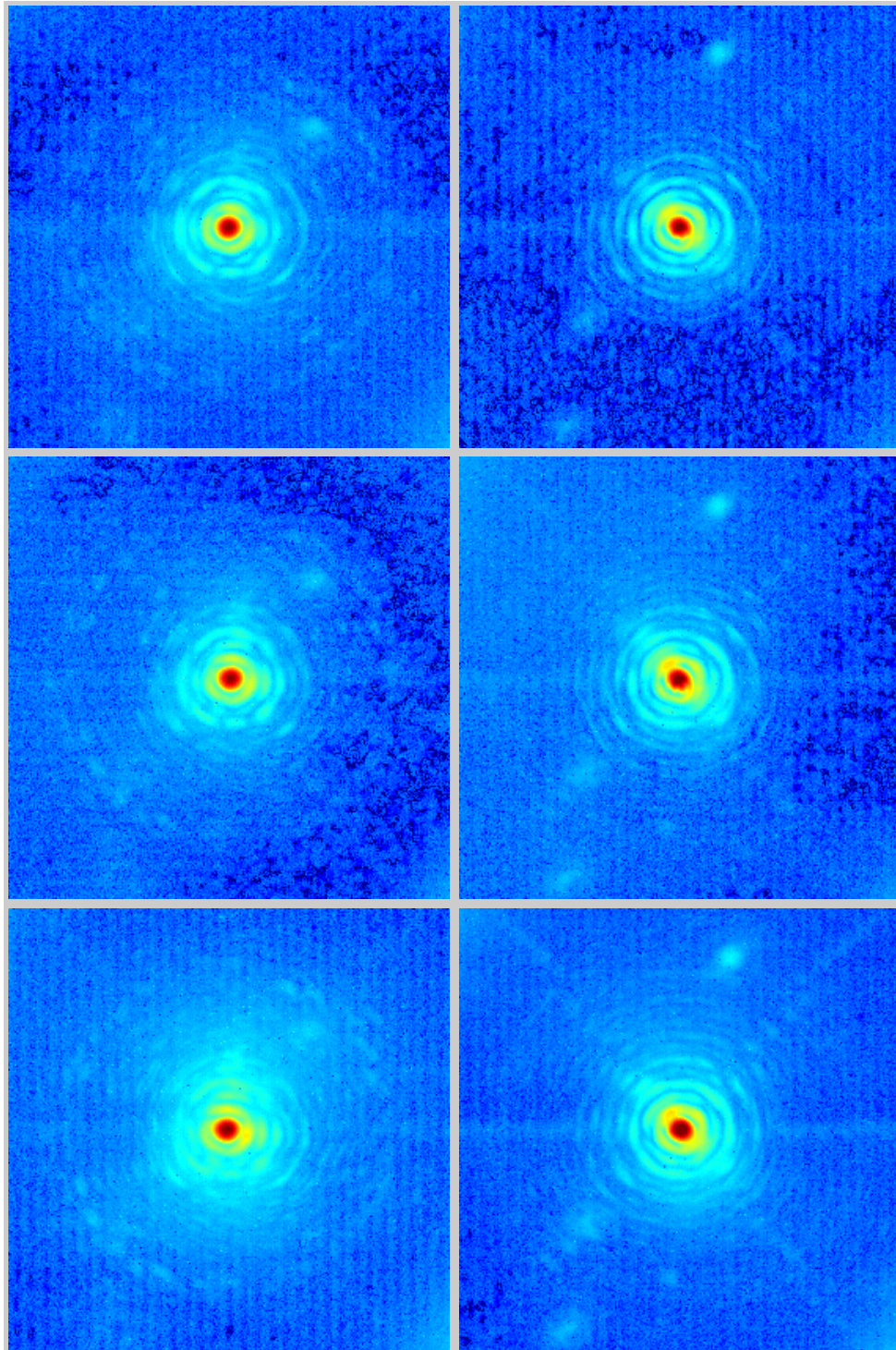


Figure 47. PSF images (non saturated) obtained for the SHS (left) and PYR (right) for the three flux cases (1st row, case A; 2nd row case B, 3rd row case C). The images are plotted with a scale $\text{PSF_counts}^{0.18}$ (Image field 0.8×0.8 arcsec). The PSF corresponds to the highest SR cases (SHS with no SF and 413 modes, and PWFS with 435 modes).



HIGH ORDER TESTBENCH

SHS and PWFS comparison test report

Doc:
Issue: 1.0
Date:
Page: 70 out of 80

	Method 1				Method 2			
	SHS		PWS		SHS		PWS	
	413 mod	413 mod SF	435 mod	561 mod	413 mod	413 mod SF	435 mod	561 mod
Star A	82	79	104	102	78	77	101	101
Star B	76	73	90	89	74	70	90	89
Star C	65	71	81	80	62	69	82	79

	Method 1				Method 2			
	SHS		PWS		SHS		PWS	
	413 mod	413 mod SF	435 mod	561 mod	413 mod	413 mod SF	435 mod	561 mod
Star A	0.045	0.045	0.038	0.037	0.044	0.044	0.041	0.041
Star B	0.045	0.046	0.038	0.038	0.045	0.044	0.041	0.041
Star C	0.046	0.045	0.045	0.044	0.045	0.044	0.044	0.044

Table 12. SR (%) and FWHM (arcsec) results for the different flux conditions and reconstructor cases. Regarding star A, we show the best result for each sensor (SHS A1, and PWS A2). As a reference, the SR and FWHM of the open loop image was **11%** and **0.0686 arcsec** respectively.

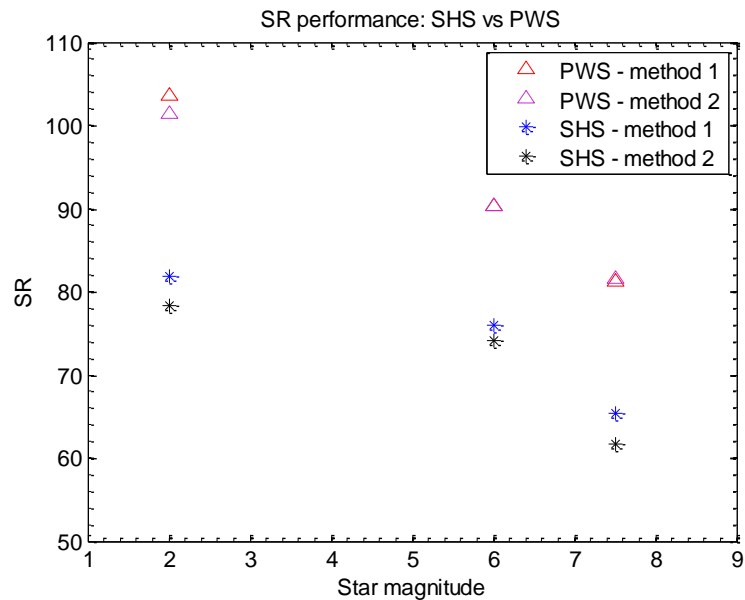



Figure 48. Plot showing the performance on terms of SR (H band) of both WFS for the three flux conditions studied (equivalent star magnitude on sky of 2, 6 and 7.5 for a XAO system at 1.2 KHz). The Strehl ratio was computed using two different methods. Taking into account the relative difference on SR, the PWS shows to perform better than the SHS.

	HIGH ORDER TESTBENCH SHS and PWFS comparison test report	Doc: Issue: 1.0 Date: Page: 71 out of 80
---	--	---

Finally, Figure 48 compares the best SR values obtained with both sensors at the three flux levels considered. Note that the PWFS shows to perform better than the SHS. From the SHS PSF images (Figure 47) it is clear that a loss of SR is due to the strange ring of speckles on the halo region.

8.6 PSF correction versus star magnitude: PSF profile and contrast

We will compare in this section the PSF correction in terms of PSF profile shape and contrast achieved at different angular distances, for the three flux levels (case A, B, and C) considered. The method to estimate the profile from the non-saturated PSFs was discussed in section 8.3.2.

Figure 49 shows the profiles for all the PSFs analysed. For the case A magnitude, as explained in the previous section, the performance was measured twice (cases A1 and A2). Note that the PSF profiles for the PWS and SHS sensor are quite similar, the mayor difference being found on the halo level. The PWFS is able to reduce better the energy inside the halo; this is consistent with the SR difference seen between both sensors (Figure 48). The differences in the shape of the first rings are caused by differential aberrations on the non common path, which are not compensated for during close-loop operation.

Figure 50 compares the experimental and theoretical PSF profiles. Only the best experimental PSFs are shown (SHS with no SF and 413 modes, and PWFS with 435 modes). The theoretical profiles were obtained from the theoretical PSF computed using the Fourier transform as explained in section 8.3.3. There is some small difference on the theoretical PSFs for the PWS and the SHS, since the integrated flux was slightly different in both cases.

As discussed in section 8.2.5, we have also acquired a set of saturated PSFs for the purpose of studying the profile characteristics with more detail. The profiles of the saturated PSFs are shown in Figure 51. Note that the profiles are similar to the non-saturated images, so no improvement in the quality of the profile was obtained, meaning that the PSF halo was not hidden by the image background. (Additional saturated profiles covering all the cases can be found in the annexe).

Figure 52 compares the contrast curves obtained for the three fluxes (left SHS, right PWS). The contrast curves are obtained renormalizing the profiles to the PSF peak. The individual contrast curves comparing SHS and PWS can also be found in the annexe.

Table 13 compares the contrast level at three different distances from the PSF center: 0.15, 0.25 and 0.45 arcsec. Note that the contrast measured with the PWS is about a factor 2 better than the SHS at the three distances considered.



HIGH ORDER TESTBENCH

SHS and PWFS comparison test report

Doc:
Issue: 1.0
Date:
Page: 72 out of 80

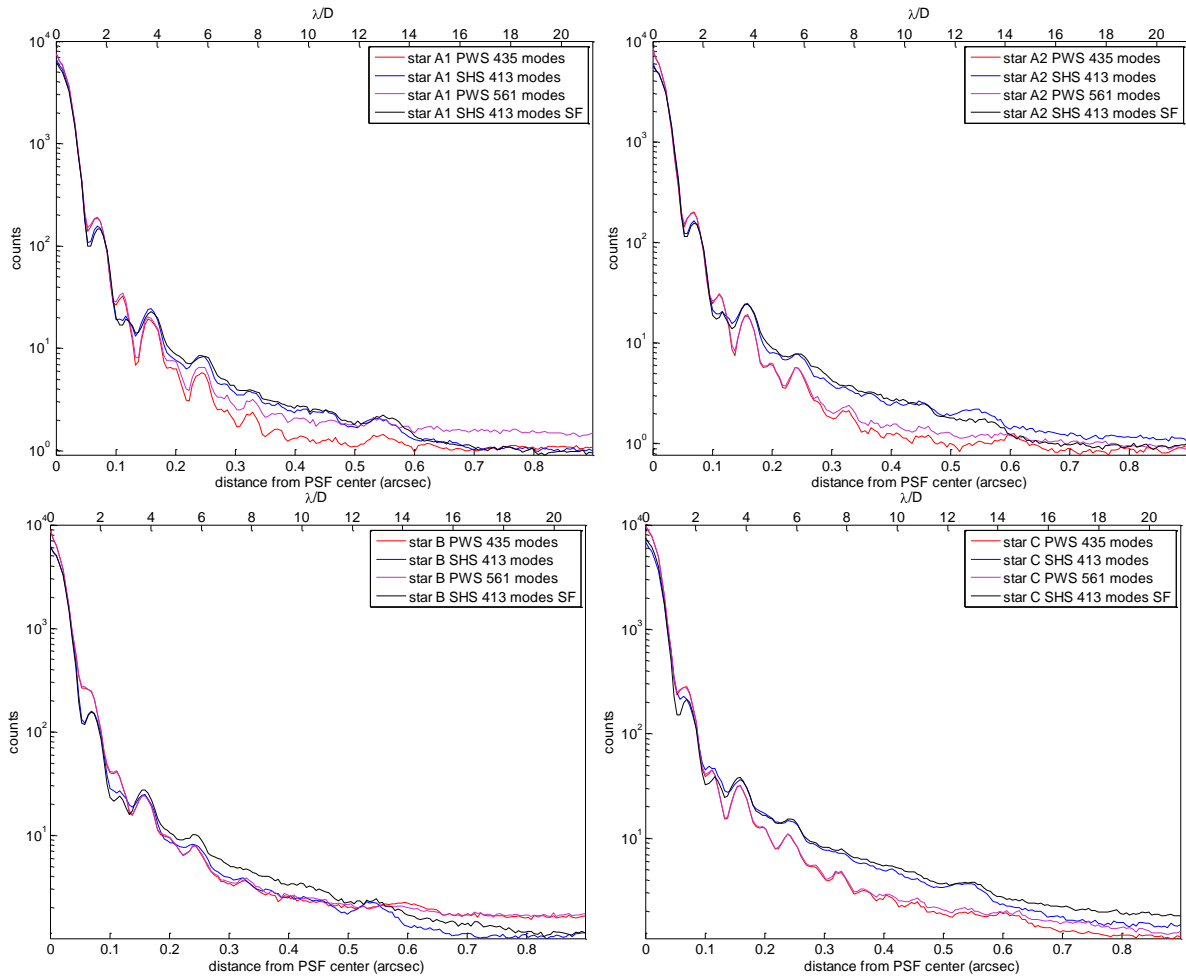


Figure 49. Profile plots estimated from all the non-saturated PSFs analysed. The two plots at the top correspond to the two sets of experiments performed for the case A magnitude. The plots for case B and case C are shown in the bottom row. The profiles obtained with the SHS (with and without SF) and with the PWFS (with 435 and 561 controlled modes) are shown in all plots.



HIGH ORDER TESTBENCH

SHS and PWFS comparison test report

Doc:
Issue: 1.0
Date:
Page: 73 out of 80

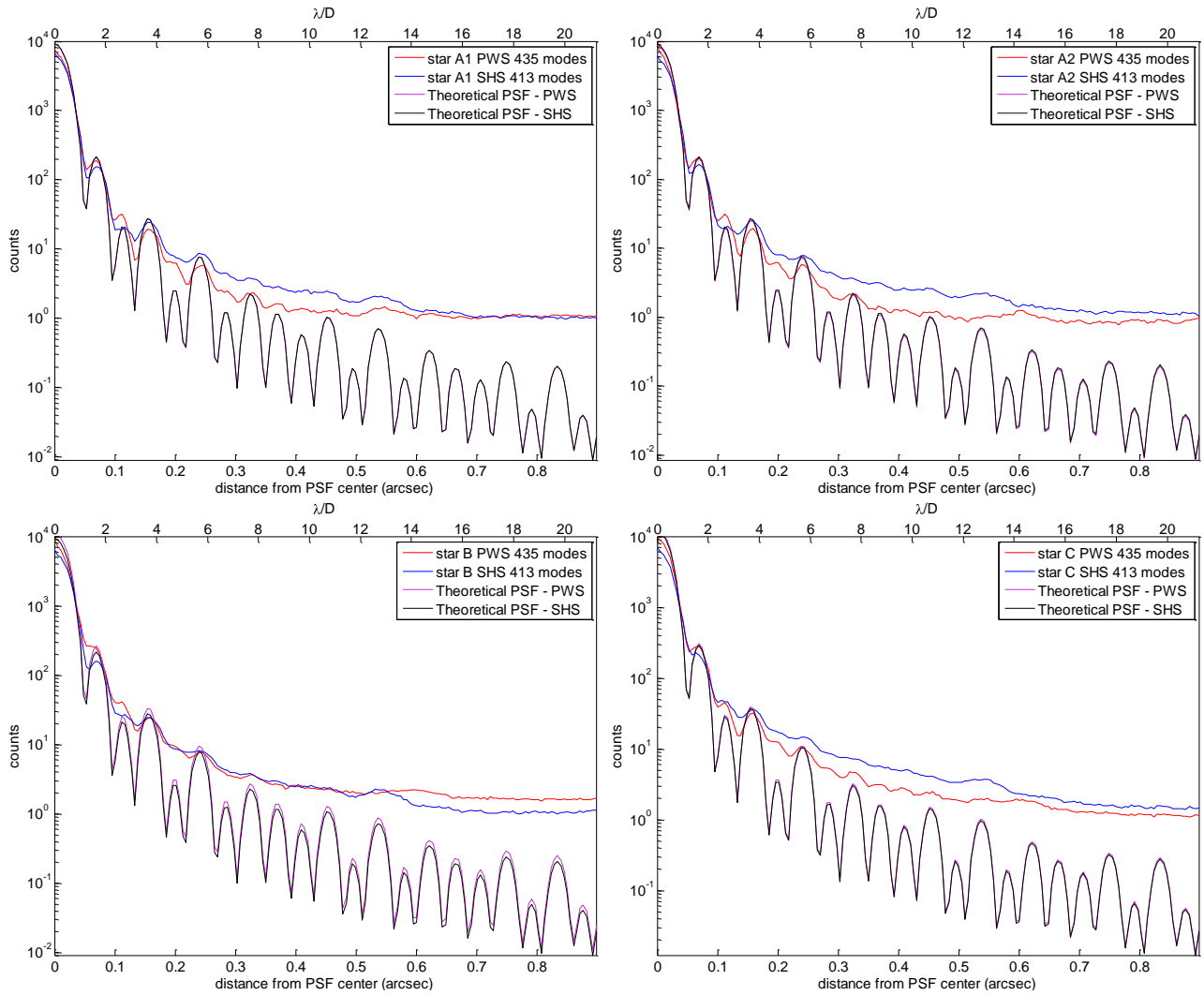


Figure 50. Comparison of experimental and theoretical PSF profiles. The experimental non-saturated PSFs shown in this figure correspond to the SHS without SF and the PWFS with 435 controlled modes. The two plots at the top correspond to the two sets of experiments performed for the case A magnitude. The plots for case B and case C are shown in the bottom row.



HIGH ORDER TESTBENCH

SHS and PWFS comparison test report

Doc:
Issue: 1.0
Date:
Page: 74 out of 80

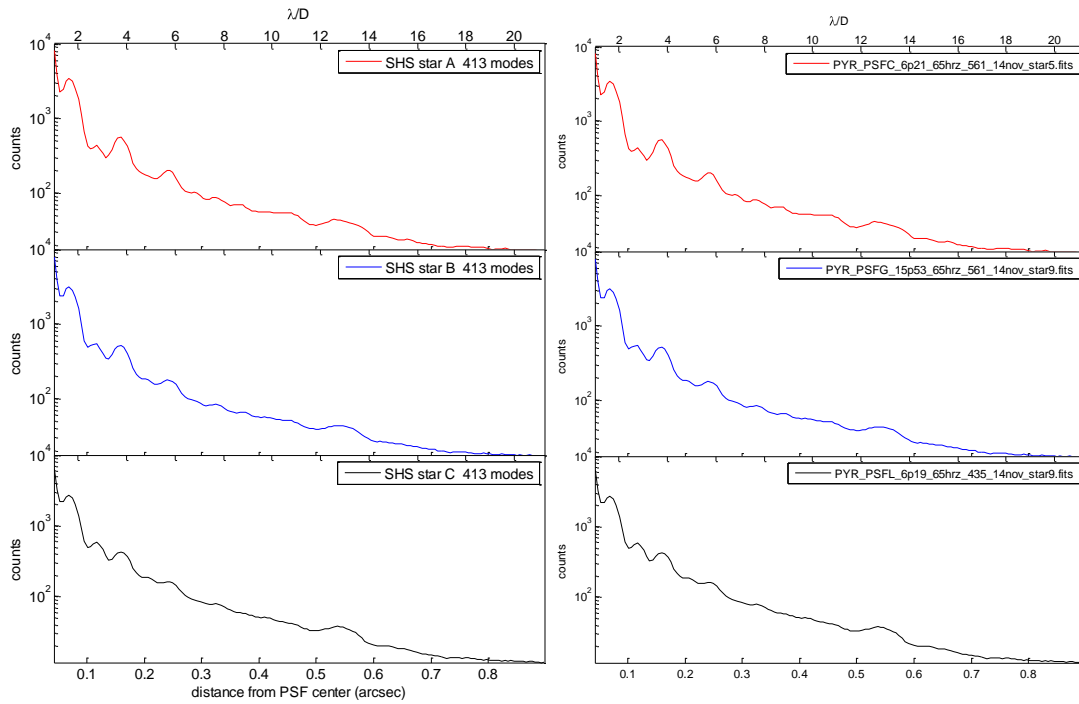


Figure 51. Profiles of the saturated PSF measurements for the three flux conditions (SHS case on the left column and PWS case on the right one).



HIGH ORDER TESTBENCH

SHS and PWFS comparison test report

Doc:
Issue: 1.0
Date:
Page: 75 out of 80

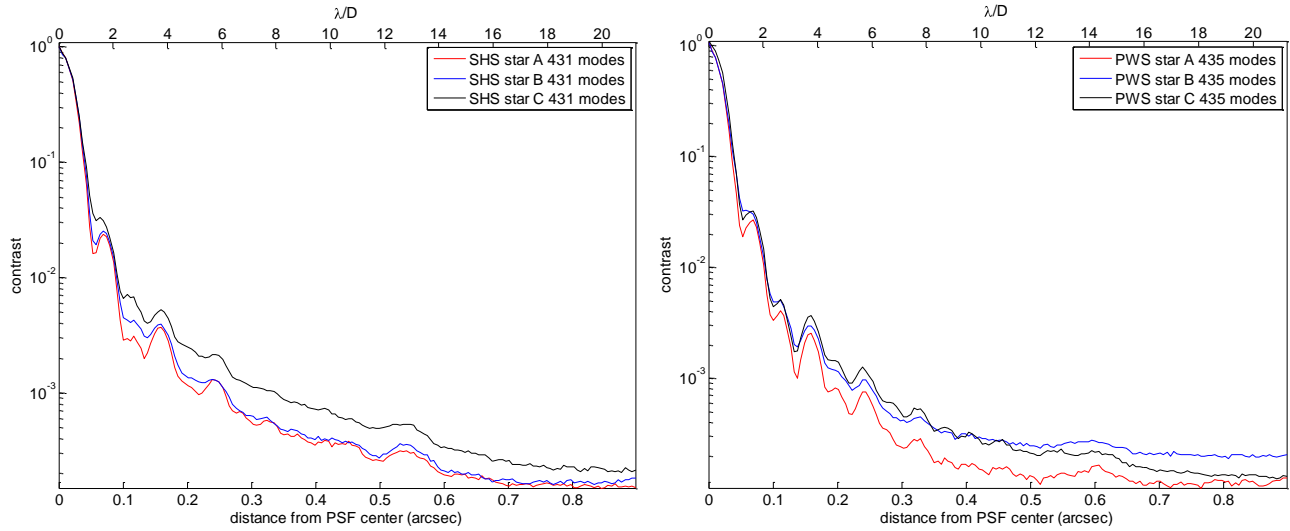


Figure 52. Compare contrast for the three flux conditions. (SHS, left; PWS, right).

SHS	0.15 arcsec	0.25 arcsec	0.45 arcsec
Star A	3.26E-03	1.26E-03	3.81E-04
Star B	3.63E-03	1.25E-03	3.73E-04
Star C	4.70E-03	2.11E-03	5.95E-04

PWS	0.15 arcsec	0.25 arcsec	0.45 arcsec
Star A	1.92E-03	6.24E-04	1.47E-04
Star B	2.47E-03	8.19E-04	2.58E-04
Star C	2.76E-03	9.50E-04	2.43E-04

(PWS/SHS)	0.15 arcsec	0.25 arcsec	0.45 arcsec
Star A	0.59	0.50	0.39
Star B	0.68	0.66	0.69
Star C	0.59	0.45	0.41

Table 13. Contrast level obtained for both sensor at different distances from the PSF center.



9 Conclusion and discussion

The described experiment studied the performance of the AO loop correction using two different wavefront sensors. Both sensors have the same number of 31x31 subapertures. The number of controlled actuators is about 700. The simulated seeing conditions was 0.5 arcsec at 550 nm during the described performance test. The AO system performance metrics were identified as system SR and PSF contrast measured on an auxiliary infrared camera in H band. A summarizing table with the achieved SR is reported below:

	SHS	PWS
Mag 2.4	82/78	104/101
Mag 5.9	76/74	90/90
Mag 7.51	65/62	81/82


The measurements show that the SR achieved by the SH sensor and PWS have a maximum value of 82% and 104% respectively.

The table shows that the SR achieved by the PWS are higher by 15%-20% in the range of fluxes analyzed. The relative gain in SR with guide star brightness is similar for both sensors, so the observed difference can largely be explained by a different peak performance for bright guide stars. The next table summarizes the results obtained for the PSF contrast at 0.25 arcsec of distance from the PSF center (numbers to be multiplied by 1e-3).

	SHS	PWS
Mag 2.4	1.3	0.62
Mag 5.9	1.2	0.82
Mag 7.5	2.1	0.95

The measurements show that both WFSs obtain results around 1e-3. The contrast measured by the PWS is about a factor 2 better than the SHS. From the considered data we state that an AO system with 31x31 subapertures and about 700 actuators can be efficiently controlled to achieve H-band SR higher than 80% and contrast better than 1e-3. The experiment so demonstrates that XAO systems can be calibrated with the accuracy required to obtain the performance estimated in numerical simulations.

These results were obtained using two different work concepts, especially in terms of calibration and modal basis creation. The SHS uses Haddamard calibration and double diagonalization method for the modal basis creation because it is the way the XAO system of SPHERE will work. In the other hand, the PWS uses a modal calibration as foreseen for the PWS that will be installed in the LBT AO system.

	HIGH ORDER TESTBENCH SHS and PWFS comparison test report	Doc: Issue: 1.0 Date: Page: 77 out of 80
---	--	---

The presented results were achieved by using 413 and 435 correcting modes with the SHS and PWS respectively. In the case of the SHS, the 413 modes were the highest number of modes that ensured loop stability. In the case of the pyramid, a test has been done using 561 correcting modes. In this case, the SR was slightly lower than with 435 modes. However the WFS signal rms was reduced by a relevant amount (see Table 11). A possible explanation is that small non common path aberrations limits the SR achieved with the PWS so that no SR improvement results from a PWS signal reduction at the very high correction level achieved.

Meanwhile, the SHS control strategy has been improved, and a new set of measurements of the SHS performance were recorded. The peak SHS SR has improved to 93%. Also, the performance of the SHS using a spatial filter was further investigated. It is hampered by the reduced linear range of the SHS when using the filter especially in case of actuator saturation of the MEMS DM. How to efficiently make use of a spatial filter with the SHS will be subject to further investigation.

At the same time along these experiments, it was possible to study the possibilities and limitations of new technologies. For example, the EMCCD has demonstrated its performance as a baseline detector for the next generation of AO systems. On the other hand, micro deformable mirrors are suitable for bench testing, but reliability issues related to oxidation and actuator failures need to be resolved before using them at the telescope.

New experiments will be carried out on the bench to study different coronagraphs under realistic AO conditions and the effect of a primary segmented mirror on the AO performance.



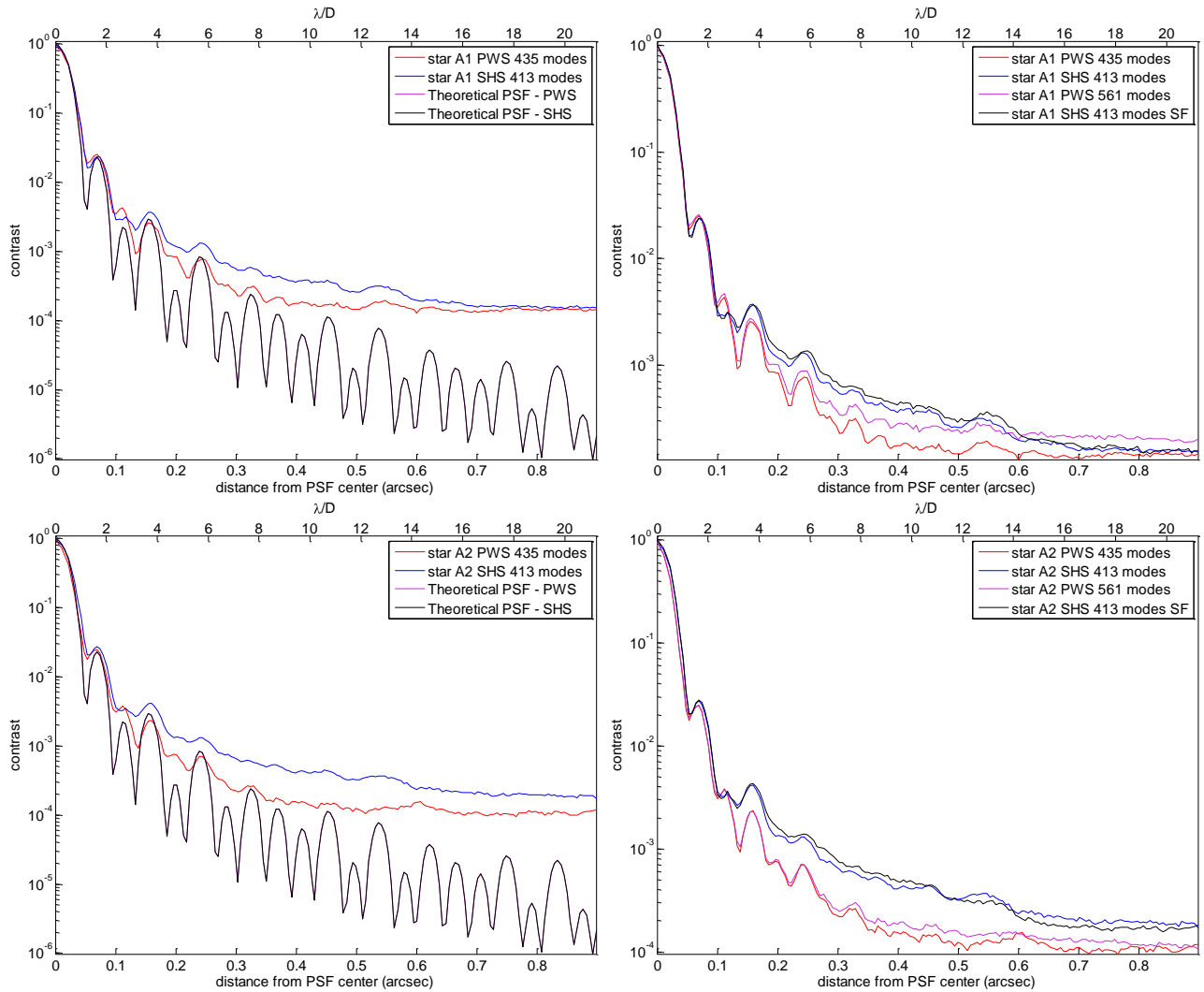
HIGH ORDER TESTBENCH

SHS and PWFS comparison test report

Doc:
Issue: 1.0
Date:
Page: 78 out of 80

10 Annex

PSF contrast scale:

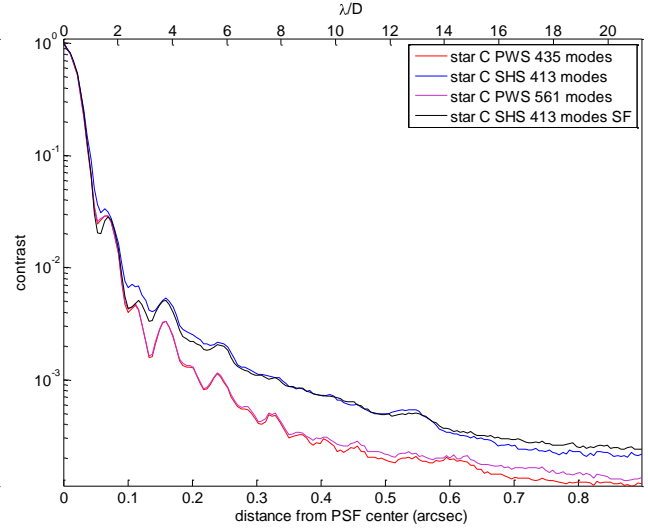
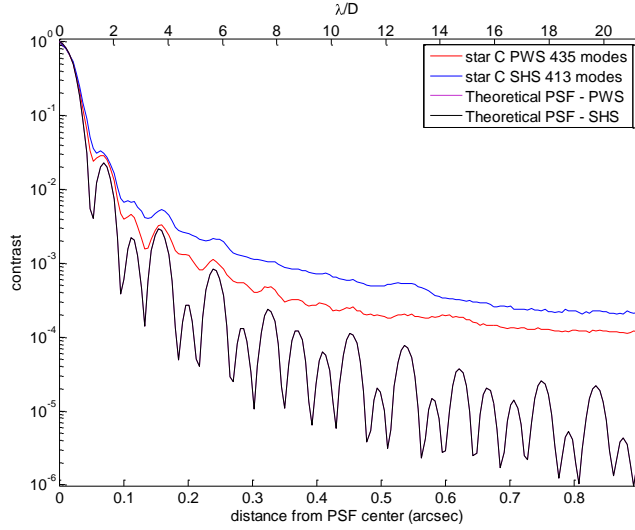
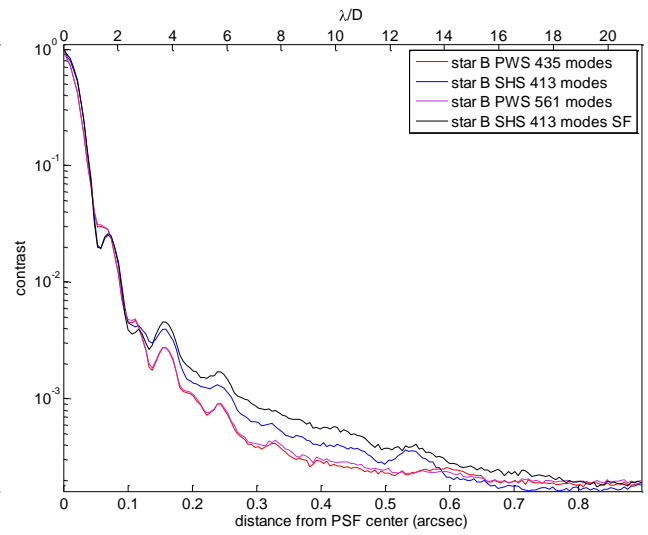
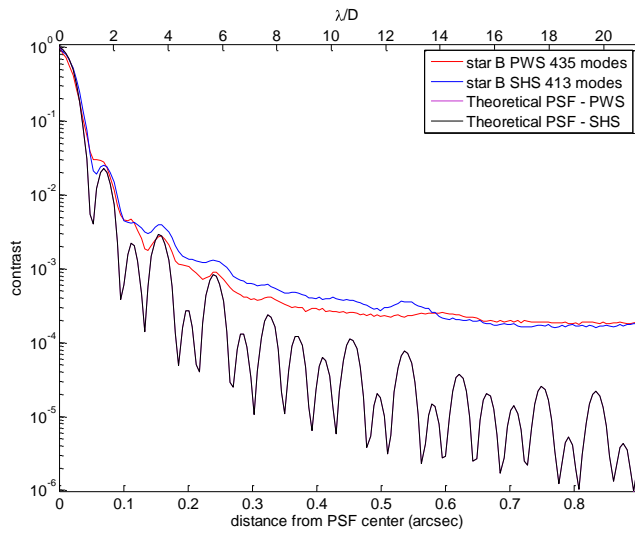




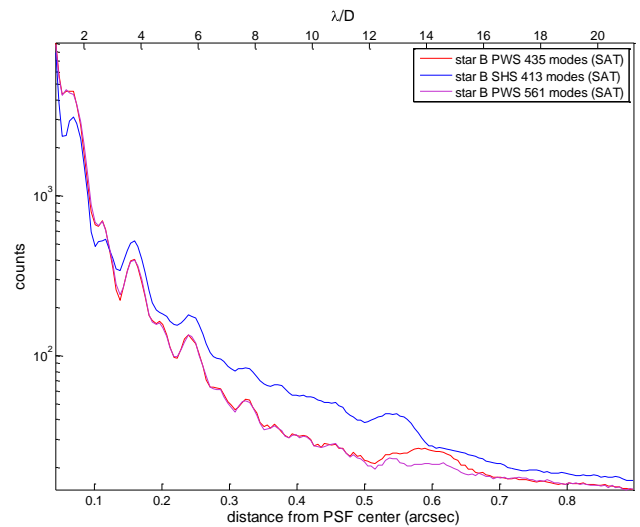
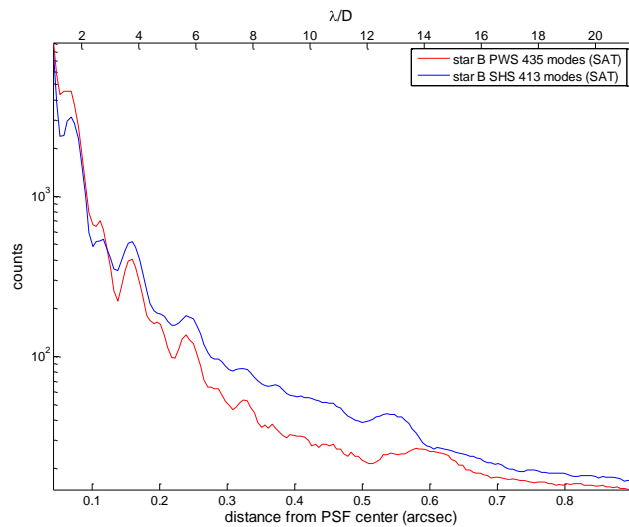
HIGH ORDER TESTBENCH

SHS and PWFS comparison test report

Doc:
Issue: 1.0
Date:
Page: 79 out of 80



Saturated PSF:





HIGH ORDER TESTBENCH

SHS and PWS comparison test report

Doc:
Issue: 1.0
Date:
Page: 80 out of 80

